Rotor Speed Microsensor
for the MIT Microengine

by

David Tang

B.S. Mechanical Engineering,
University of California, Berkeley, 1999

Submitted to the Department of Mechanical Engineering
in partial fulfillment of the requirements for the degree of
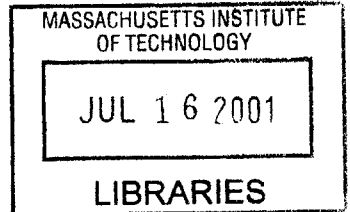
Master of Science

at the

MASSACHUSETTS INSTITUTE OF TECHNOLOGY

JUNE 2001

Signature of Author ....
Department of Mechanical Engineering
May 11, 2001

Certified by ....
Alan H. Epstein
R.C. Maclaurin Professor of Aeronautics and Astronautics
Thesis Supervisor

Certified by ....
John G. Brisson, II
Associate Professor of Mechanical Engineering
Thesis Reader

Accepted by ....
Ain A. Sonin
Professor of Mechanical Engineering
Chairman, Department Committee on Graduate Students

Rotor Speed Microsensor for the MIT Microengine

by

David Tang

Submitted to the Department of Mechanical Engineering
on 11 May 2001, in partial fulfillment of the
requirements for the degree of
Master of Science

Abstract

This thesis presents the design, fabrication, and testing of a temperature-based sensor for measuring rotor speeds in the MIT MEMS micro gas turbine engine. The MIT microengine is a gas combustion engine made by micromachining and bonding six silicon wafers. The sensor is a boron-doped polysilicon resistor with a serpentine geometery that is thermally isolated from the substrate. The sensor is designed to measure the rotor rpm by responding to the heat flux fluctuations on the wall above the compressor blade tips. This thesis investigates the feasibility of this approach.

The sensor development process involved fabricating stand-alone devices (which have only the sensor and contact pads and not integrated with other microengine components) and testing them using a furnace and a shock tube. The furnace test characterized the stability with thermal cycling and annealing. The shock tube test characterized the dynamic response.

The temperature coefficient of resistivity (TCR), 0.009/K , and the room temperature resistance, ~9 kohms, measured in the furnace characterization experiments were approximately 50% less and 300% more than the predicted values, respectively. These discrepancies may be due to the fabrication process conditions, such as ion implant dose, polysilicon deposition temperature, and anneal conditions. The time constant, 9-10 μsec, measured from the shock tube experiments matched predicted values to within 20-40% depending on the model used to estimate the convective heat flux into the sensor. However, the sensor's amplitude response was less than predicted values by approximately 10 - 75% perhaps due to the simplicity of the models used to estimate the convective heat flux.

The experimental results suggest that this concept is viable as a microengine rpm sensor. Some design changes are suggested which should improve sensor performance.

Thesis Supervisor: Alan H. Epstein
Title: R.C. Maclaurin Professor of Aeronautics and Astronautics

Acknowledgments

My two years at MIT has been a tremendous experience. I benefited from working with many top-notch people and would like to acknowledge them. My research was only possible with the help of these people. I have been fortunate to had guidance and support from people at MIT Gas Turbine Laboratory and Microsystems Technologies Laboratories.

I would like to thank Professor Epstein for the opportunity to work on this project and the guidance he provided. I learned a lot from working with him. His advice helped me complete this project and will help me in my career.

Stuart Jacobson and Arturo Ayon helped me tremendously at the beginning of my project while they were at MIT. Stu provided early guidance and good advice on how to manage my project and general support. Arturo was a tremendous resource for discussing fabrication issues and general career advice.

Xin Zhang and Carol Livermore were always available to help me with the never-ending problems I had with my project. Xin has been very encouraging and was helpful in getting me the necessary fabrication resource at times of crisis. Carol has been very patient and helpful with my continuous stream of questions.

Jerry Guenette and Stephen Umans provided with invaluable technical help. Jerry helped me tremendously with my modeling work at the beginning of my project and with equipment for the shock tube experiment. Dr. Umans helped me design and built the electronics that I used for the shock tube experiment. My project would have been a much bumpier road without their generous help.

In addition, I would like to thank all the people in MTL for their help throughout my fabrication process. In particular, I would like to thank Kurt Broderick for his consistent help

with numerous fabrication issues and Tom Takacs and Dennis Ward for their help with the deep etcher.

Finally, I would like to thank the sponsors, DARPA and the US Army Research Office. Without their funding, I would not have the opportunity to work on this project.

Contents

Chapter 1

Introduction

This chapter introduces the motivation for the sensor, Fig 1-1, development, discusses previous work in fast response heat flux sensors, and presents the layout of this thesis. The sensor development is part of the Massachusetts Institute of Technology (MIT) microengine project. A discussion of the microengine project is first presented to provide the reader with a better understanding of the motivation for developing the sensor, the design constraints, and the sensor's required performance. Subsequently, previous work in fast response heat flux sensors are discussed to demonstrate the development progression of similar devices. Finally, the thesis structure is discussed.

1.1 Background

The MIT microengine project is a multidisciplinary effort to develop a centimeter-scale gas turbine engine using silicon bulk and surface micromachining technology, Fig 1-2 and Fig 1-3[1]. The concept was proposed in 1994 by Epstein *et al.* to take advantage of silicon's high-strength at the microscale and the cube-square law to achieve higher power-to-weight ratio than conventional gas turbine engines. Subsequently, a multidisciplinary research effort began to develop the fundamental technologies, such as high-temperature material, high-speed gas bearings, microscale combustion systems, silicon fabrication, and wafer bonding, to develop such a device.

The microengine project's objective is to produce a gas turbine engine with a higher power-

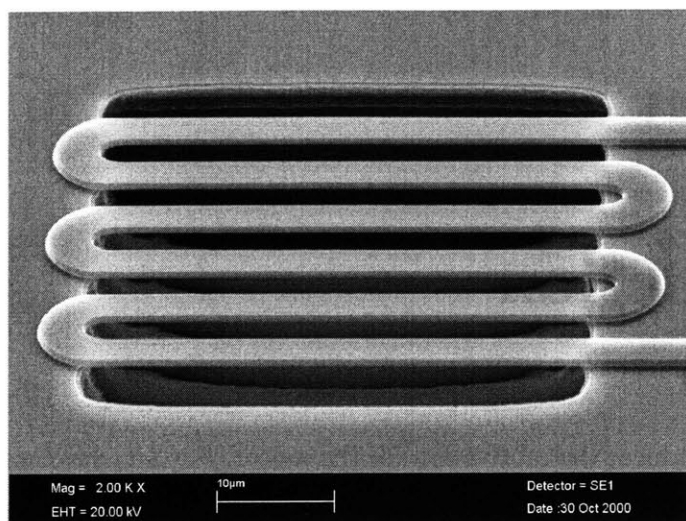Figure 1-1: SEM photograph of the sensor. The sensor is a polysilicon structure with the ends resting on silicon dioxide on a silicon wafer.
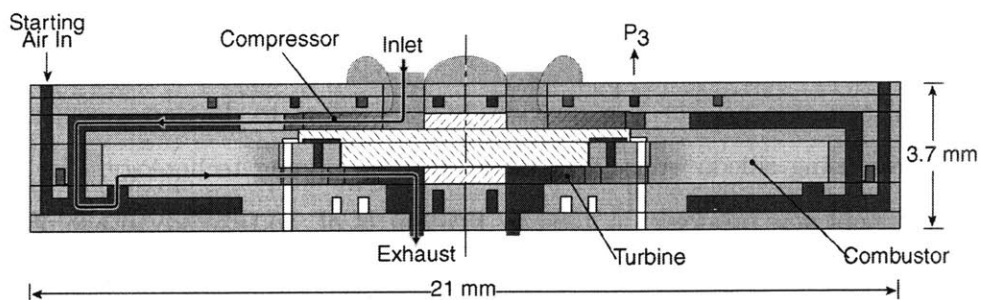

Figure 1-2: Schematic of the cross-sectional view of a microengine design. Flow enters through the top wafer, passes rotor and flow radially outward, enters the combustion chamber from the bottom, combusts, and exits the bottom after passing the turbine.
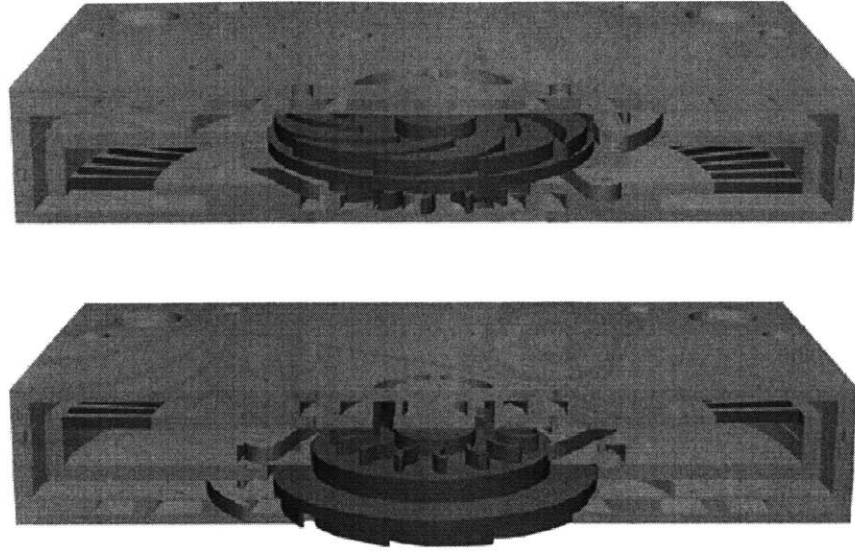
Figure 1-3: Schematic of a cross-sectional cut view of a microengine design.

to-weight ratio, i.e. higher power density, than conventional gas turbine engines. One of the keys to achieving high power density using rotating machinery is to achieve high tip speed. High tip speed requires high strength material and suitable air bearings. Single crystal silicon is strong at the microscale because of low defect concentration and, thus, capable of surviving the large stresses caused by a high tip speed. The higher surface area-to-weight ratio of miniature air-bearings allows larger loads to be supported[2]. A microengine's potential applications include portable battery replacement, microvehicle propulsion, boundary layer and circulation control, and coolers[3].

The microengine is a 2.1 cm square 3.3 mm thick silicon device. It is made by defining features onto six wafers using silicon fabrication techniques, such as photolithography, etching, and deposition, and then bonding the six wafers together at temperatures typically above 900 °C, Fig 1-4. The top wafer, Level 1, and the bottom wafer, Level 6, are the Forward Cap and the Aft Cap, respectively. The second wafer from the top, Level 2, and the second wafer from the bottom, Level 5, are the Forward Thrust Bearing and the Aft Thrust Bearing, respectively, which help stabilize the rotor during operation. The middle two wafers, Level 3 and Level 4, have the compressor and turbine blades, respectively, and they also form the combustion chamber.

Level 1: Foward Cap

Level 2: Foward Thrust
          Bearing

Level 3: Compressor

Level 4: Turbine

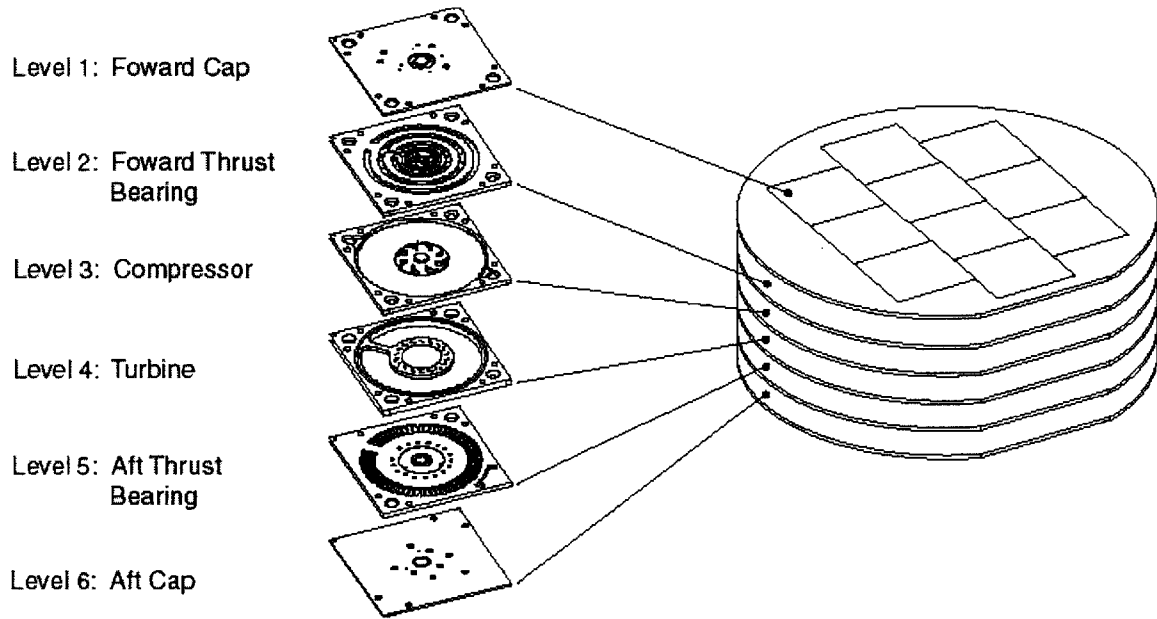Level 5: Aft Thrust
          Bearing

Level 6: Aft Cap

Figure 1-4: Schematic of the six wafers in a microengine. The ten squares on the wafer corresponds to ten devices.

The microengine is designed to produce 10 grams of thrust using 16 $\frac{grams}{hour}$ of hydrogen fuel and 0.36 $\frac{grams}{sec}$ of air[4]. The air and fuel enters the device through Level 1 and 2, passes the compressor blades, enters the combustion chamber, combusts, passes the turbine blades, and exits through Level 5 and 6, as shown in Fig 1-2. The microengine is a high temperature device and its combustion chamber approaches silicon's melting temperature. The combustion chamber is designed to operate at 1600 K combustion exit gas temperature. The compressor blades are at about 800 K and the wall above the compressor blades, Level 2's bottom surface, is about 700 K.

A potential application of the microengine is microairplane propulsion. A microairplane is currently being developed in conjunction with the microengine project. The current design is a six-inch wingspan jet-propelled micro air vehicle (JMAV), Fig 1-5, with a 30 $\frac{m}{sec}$ flight speed and a 50 km range. Once the microengine is implemented, it will eliminate the batteries, power electronics, and motor of a JMAV[5].

The purpose of the sensor discussed in this thesis is to enable the microengine to be flight-capable. In order for the microengine to power the microairplane, all the diagnostic tools and

14

JMAV 2A

T/O mass   :   40 g
Wingspan   :   12 cm
Airspeed   :   16-31 m/s (30-60 kt)
Endurance: 30 minutes
Range   :   50 Km

Payload   :   15 g (10 cm³)
Fuel   :   8 g
Engine   :   4 g
Cntl Elec: 8 g
Actuators: 2 g
Structure: 3 g

S_{ref}:   35 cm²
CL   :   0.20-0.75
Re_c :   30000-60000
L/D :   4.0-6.0

Rohacell / CF mat
surfaces

Smoovy 30001
Actuators

μ-Turbojet Engine

Rudder/Elevator Control

12 cm

Payload

Butane tank

Nav/Control Avionics

MD
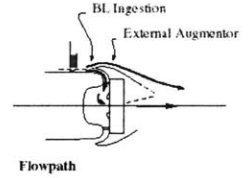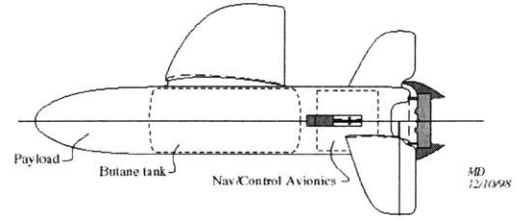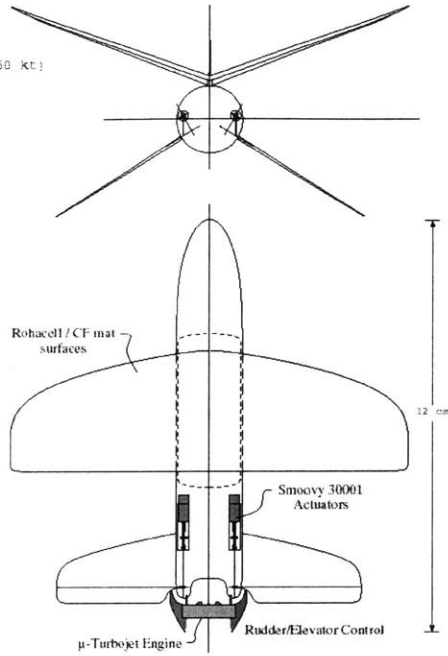12/10/98

BL Ingestion

External Augmentor

Flowpath

Figure 1-5: Schematic of the jet-propelled micro-air vehicle.

control systems must be flight-capable, i.e. small and light-weight. The on-board control system requires a sensor to measure the performance of the microengine to close the control loop. The control system will actuate the valve controlling the fuel supply to the microengine. The candidate measures for the control system to sense are the rotor speed, pressure, and temperature. The rotor speed is the simplest candidate in terms of design, operation, and fabrication complexity. Most macroscale engines use the pressure difference across the compressor for their control systems. However, the control algorithm would require absolute accuracy in either the pressure ratio across the compressor or flow temperatures, as seen from the thrust equation, Eq 1.1[6], for a turbojet with an ideal cycle

$$\frac{Thrust}{unit\_mass} = \sqrt{\frac{2}{\gamma - 1}\left(\frac{\theta_t}{\tau_c} - 1\right)(\tau_c - 1)} \tag{1.1}$$

where γ is the ratio of specific heat, θ_t is the ratio of the total temperature after the turbine blades to the engine's inlet temperature, and τ_c is the temperature ratio across the compressor. Measuring pressure and flow temperature with absolute accuracy would be difficult in terms of

design and operation. Pressure transducers have temperature dependences that restricts their operating range and their measurements may drift over time. Measuring flow temperature with absolute accuracy requires a temperature sensor that is thermally isolated from the device, which is a major design challenge because such a small device is approximately isothermal. In addition, a pressure or flow temperature sensor requires calibration for each microengine because the efficiency is required for an engine with a non-ideal cycle. In contrast, the rotor speed can be measured by detecting the fluctuation frequency in certain phenomenon, such as flow temperature or pressure. The rotor speed can be related to the thrust with an equation similar to the previous equation, Eq 1.2[7], and Euler's equation for a compressor, Eq 1.3[8]

$$
\begin{aligned}
\frac{P_{compressor}}{\dot{m}} &= C_p(T_{t2} - T_{t1}) & (1.2) \\
\eta &= \frac{\pi^{(\gamma-1)/\gamma} - 1}{T_{t2}/T_{t1} - 1} \\
\pi &= \frac{P_{t2}}{P_{t1}}
\end{aligned}
$$

$$
C_p(T_{t2} - T_{t1}) = \omega(r_2 v_2 - r_1 v_1) \tag{1.3}
$$

where $\frac{P_{compressor}}{\dot{m}}$ is the compressor power per unit mass flow, η is the compressor efficiency, π is the pressure ratio across the compressor, C_p is the specific heat, T_t is the total temperature, ω is the rotor speed, r is the radius, v is the tangential velocity, and the subscripts 1 and 2 denotes upstream and downstream of the compressor blades, respectively. Measuring the fluctuation frequency is simpler because it does not require measuring the phenomenon with absolute accuracy. Also, the fabrication process for the sensor that will be presented is relatively simple, a two-mask process where the number of mask is a measure of process complexity, and uses standard silicon processing.

1.2 Approach

There are several methods to measure blade passing frequency to obtain the rotor speed. The ones considered involve detecting fluctuations in certain phenomenon, such as pressure, optical

interference, and temperature, as the blades pass. Pressure transducers can have good stability over time as demonstrated by Kulite, whose pressure transducers drift by less than 0.1% per year[9]. However, a pressure approach poses two major challenges: small expected pressure fluctuations (~10 kPa) across the blades[10] and packaging a pressure transducer capable of operating up to 800 K. As a reference, Kulite's silicon-on-silicon sensor technology can produce pressure transducer that can operate continuously up to a maximum temperature of 400°C and their smallest package is 0.062" in diameter and 0.20" long. The highest temperature that Kulite's pressure transducer is capable of operating at is just below the wall temperature. Thus, such a pressure transducer will require cooling if packaged with the microengine. Any additional packaging will come at the expense of the micro-airplane's payload and is not desirable. Even the smallest Kulite pressure transducer will consume volume and mass budgeted for the payload. On the other hand, no external packaging may be required if a pressure transducer is integrated into the microengine's fabrication process. However, calibrating a pressure transducer that is already in the microengine will pose some challenges.

An optical approach is the current method used to measure rotor speed in a laboratory benchtop set-up. It consists of a fiber optic system that detects fluctuations in reflected light. An optical approach is more suitable for measuring high frequency signals because solid-state detectors are capable of having fast response time (~0.1 to 1 μs). An optical approach can be integrated with the microengine by either miniaturizing the fiber optic system and package it with the microengine or embedding optoelectronics into Levels 1 and 2. However, similar to the case of pressure transducers, additional packaging will consume volume and mass budgeted for the payload and therefore, an external package is not a feasible option. Also, they typically operate below 300 K[11] and even a photodectector embedded into the microengine will require additional packaging for cooling.

Considering the disadvantages of measuring pressure and optical interference, Table 1.1, a temperature measurement approach was chosen. A temperature based method can leverage previous work on polysilicon anemometers, whose resistance varies with temperature. Polysilicon fabrication methods are well-established and are compatible with the current microengine's fabrication process. The fabrication process for the sensor presented in this thesis is a two-mask process and uses material that is compatible with silicon processing. In addition, the device

17

Table 1.1: Comparison of the different methods for measuring rotor rpm.

Method	Advantages	Disadvantages
Pressure	- Good stability	- Small expected pressure fluctuations - Low maximum operating temperature - Packaging complexity - Calibration
Optical	- Fast response	- Low maximum operating temperature
Heat flux	- Leverage previous work - Compatible with Si fab process	

can withstand the high temperature wafer bondings, ~1100 K, and the microengine's operating temperature. Thus, the concept chosen is to use a doped polysilicon sensor to measure heat flux fluctuation frequency.

A sensor placed above the blades will experience heat flux fluctuations as the blades pass underneath. As the blades pass, the sensor alternates between being 20 μm away from a 800 K blade to about 420 μm away from the blade base. The air temperatures at the midpoint between the sensor and the blade and between the sensor and the blade base are approximately 810 K and 400 K, respectively. The heat flux fluctuation, which results from the fluctuating flow temperature and velocity, experienced by the sensor will cause its temperature to fluctuate if its thermal response is fast enough. The sensor's temperature fluctuation will be detectable if it has a fast thermal response, sufficiently thermally isolated, and the heat flux fluctuation is large enough. The sensor's temperature fluctuation frequency corresponds to the blade passing frequency. Since doped polysilicon's resistance varies with temperature[12], the voltage across the sensor will fluctuate when a constant current is supplied to the sensor. A sensor with high-frequency response will have detectable voltage fluctuations, where the minimum detectable voltage fluctuation is determined by the noise and the electronics. The heat flux fluctuation is a function of the operating conditions, such as the wall temperature, rotor speed, gas flowrate, etc., and was estimated using a 3-D computational fluid dynamics (CFD) simulation results.

Stand-alone sensors (sensors with contact pads and that are not integrated with other microdevices) were fabricated and tested. They were first tested using a furnace to characterize their temperature coefficient of resistivity (TCR), the proportional constant that relates resis-

tance to temperature, and to test their robustness to high temperature. Subsequently, they were tested using a shock tube to characterize their dynamic response and to test their robustness to pressure perturbations.

1.3 Previous Work

The sensor described in this thesis is a temperature sensor used to detect the heat flux fluctuation frequency. Numerous researchers have presented different sensors designs that can measure heat flux or heat flux changes. However, none of the previous designs can be directly applied in the microengine to detect heat flux fluctuation frequency because the microengine requires a sensor that has relatively high-frequency response and is integrable with the microengine's fabrication process. Nevertheless, previous work provides useful information about the important considerations in designing a high-frequency response temperature sensor to measure heat flux fluctuations.

As reported in 1985, Epstein *et al.* developed a double-sided, high-frequency response heat flux gauge capable of measuring heat flux from dc to 100 kHz[13]. The device is a layered gauge with a 0.15 μm metal films, which serves as resistance thermometers, sputtered on both sides of a 25 μm polyimide sheet, Fig 1-6. The gauge is used by adhesively bonding it to a test article. At low frequencies, less than 20 Hz, the temperature difference across the polyimide is proportional to the heat flux normal to the surface. At high frequencies, greater than 1.5 kHz, the polyimide layer appears infinitely thick and the temperature at the upper surface can be used with a quasi-1D semi-infinite solid heat conduction analysis to calculate the heat flux. Even though this device can measure heat flux up to 100 kHz, this device's fabrication process is not compatible with silicon fabrication process and cannot be used in the microengine.

As demonstrated by the heat-flux gauge developed by Epstein *et al.*, the surface temperature measurement is most important in measuring high-frequency heat flux because the thermal penetration depth is inversely related to the square root of the frequency. Therefore, a sensor placed on the surface of a substrate can be a fast response sensor for measuring high-frequency heat flux into the substrate. Fast response sensors (< 1 μs) can be fabricated onto substrates with advancements in thin-film processes that allow thinner devices (~ 1 μm) to be fabricated[14].
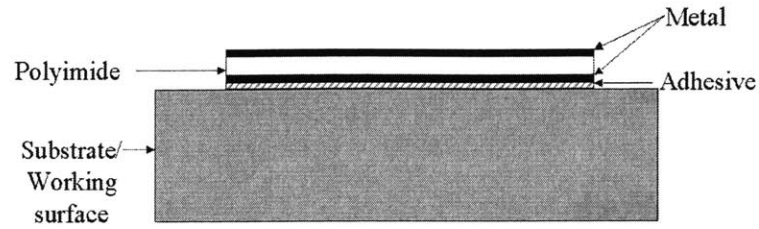
Figure 1-6: Schematic of the high-frequency heat flux gauge developed by Epstein et al. A 25 micron thick polyimide substrate is coated with 0.15 micron of metal film on both sides. The gauge is then placed on the working surface with adhesive.

For example, Dunn developed devices with a resistance temperature device, which had a typical thickness of 0.1 μm, sputtered onto MACOR that have transient responses on the order of 0.01 μs[15]. The response time demonstrated by Dunn is almost two orders of magnitude smaller than required for measuring the maximum blade passing frequency, 200 kHz. However, an analytical solution of a semi-infinite solid subjected to the 200 kHz heat flux expected above the blades shows that the temperature fluctuation at the surface is not detectable (refer to Chapter 2: Preliminary Analysis).

The previous device by Dunn suggests that the temperature fluctuation of a sensor that is located on a substrate's surface can be increased by increasing thermal isolation. Several researchers (Goldberg 1994, Jiang 1994, Mastrangelo 1991, Tai 1987, etc.) have developed MEMS-based suspended sensors that are only connected to the substrate at the ends to increase thermal isolation. For example, Jiang developed a micromachined hot-wire anemometers using boron doped polysilicon that are 1 μm wide, 0.5 μm thick, and 10-160 μm long. The devices are made from a sensing wire, two parallel supports, a Si beam, and a thick Si handle. The Si beams serve as a thermal and mechanical buffer between the handle and supports to reduce interference with the flow.

The thermal response of a structure like Jiang's anemometer has two time constants, (τ_1) one associated with the sensing wire and (τ_2) another associated with the wire support shanks. τ_2 for Jiang's design ranges from 100 μs to 300 μs. A square wave can be used to measure the time constant of a device with a large aspect ratio, greater than 200[16]. For a device with an aspect ratio of 200, Jiang measured a time constant of about 50 μs. For devices

with an aspect ratio less than 200, τ_1 will have a greater affect on the time constant and it varies with the wire length. τ_1 increases parabolically with the length at small lengths and becomes constant at large lengths. Jiang reports that his design with a 10 μm wire has a 40 kHz bandwidth[17]. As the sensing wire's length decrease, it becomes similar to a thin-film sensor on a substrate. The sensing wire has complete thermal contact with the substrate and the conduction of the sensing wire to the substrate approaches the case of conduction in a semi-infinite solid. Consequently, the temperature fluctuation decreases as thermal isolation decreases but thermal response increases. Conversely, thermal isolation increases as the sensing wire's length increases but a long wire's time constant is greater than that of a short wire.

Based on previous sensor designs, such as Jiang's, the sensor design discussed in this thesis balances thermal isolation and response time for use in the microengine. A balance of the two will provide an operating range where the sensor's signal will be detectable. In contrast to other researcher's sensors, where they need to reach the steady-state temperature to measure the magnitude of the temperature change, the sensor discussed here need to be able to detect the frequency of a high-frequency heat flux fluctuation. Thus, it does not need to reach the steady-state temperature but only need to have a temperature change that is detectable by the electronics.

1.4 Thesis Structure

Chapter 2 discusses the sensor's design analysis and the 3-D CFD simulation heat flux results used in the design analysis. Chapter 3 describes in detail the fabrication process of the sensor and the tools used. Chapter 4 describes the test setups. Chapter 5 discusses the test results and the design feasibility. Finally, Chapter 6 summarizes the work presented and discusses recommendations for future work.

Chapter 2

Design Analysis

2.1 Introduction

A sensor integrated in the microengine must function under the microengine's operating conditions. While the microengine is operating, the combustion will heat the wall to approximately 700-800 K and the rotor will spin up to 1.2 million rpm. The sensor must operate at the wall temperature and have sufficient spatial resolution and frequency response to detect the rotor speed. The spatial resolution must be small enough to distinguish between adjacent blades, in other words, the overall sensor dimensions should be smaller than the distance between the compressor blades. The maximum rotor speed is 1.2 million rpm, which corresponds to 200 kHz for a rotor with ten blades. Thus, the sensor must have a fast response to produce a sufficient signal-to-noise ratio (S/N). In addition, the sensor's natural frequency needs to be larger than the pressure fluctuation excitation frequency caused by the passing compressor blades.

This chapter describes the analysis leading to the design of the sensor (Fig 2-1a). The analysis is separated into two main categories: structural and S/N. The structural analysis constrains the sensor's dimension such that its natural frequency is above the primary excitation frequency. The S/N analysis constrains its dimensions and the driving current. The sensor's operating conditions at maximum rotating speed are summarized in Table 2.1. The maximum workspace dimensions are set to be less than the spacing between compressor blades to increase spatial resolution. However, later design analysis will show that increasing the sensor's length per span (where a span is a sensor section that crosses the undercut) and the number of spans

Table 2.1: Operating Conditions. The wall temperature and flow temperature are based on a 3-D FLUENT CFD simulation result, which will be introduce later in the chapter. The maximum blade passing frequency is based on a rotor with ten blades spinning at the maximum design rpm, 1.2 million rpm. The maximum dimensions are set to be less than the distance between the compressor blades.

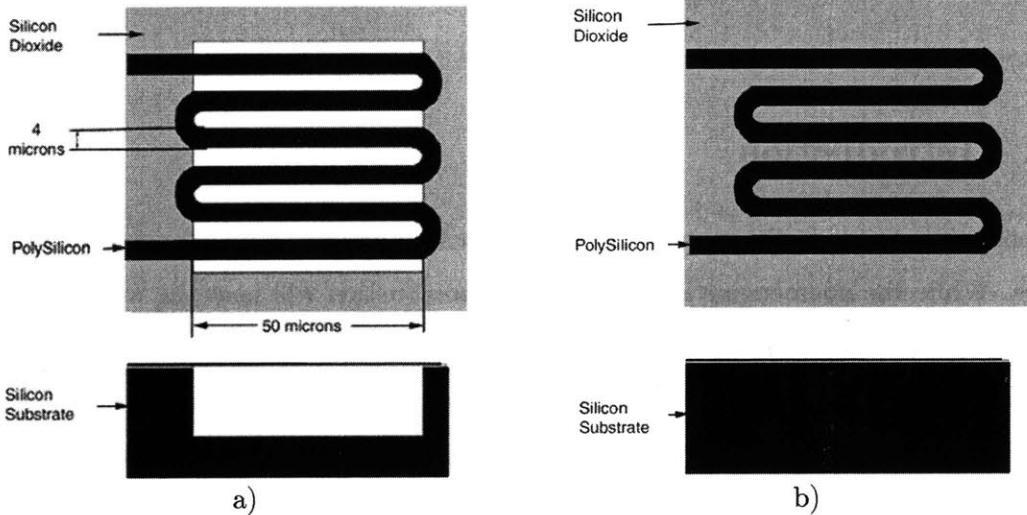|	
Maximum Wall Temperature	800 K
Flow Temperature	400 to 810 K
Maximum Blade Passing Frequency	200 kHz
Maximum Dimensions	50 μm x 50 μm

Figure 2-1: Schematics of the sensor designs. a) Baseline design, where there is an undercut. The sensing element rest on air and the ends are supported. b) Embedded design, where the whole sensor is supported.

increases the signal to noise ratio, S/N.

2.2 Preliminary Analysis: Embedded Sensor

The baseline sensor design has the middle of the sensing element above air and the ends supported by the substrate. The undercut beneath the sensing elements improves thermal isolation and increases the signal. However, a sensor that has no undercut would have a more straightforward fabrication process and would be more structurally robust. Such a sensor was mentioned in Chapter 1 and one was demonstrated by Dunn to have a transient response that is less than 1

μsec. The temperature change, which the signal is a strong function of, needs to be determined to assess the applicability of such a device in the microengine. A thin sensor located at the surface with no undercut can be modeled as the surface of a semi-infinite solid. This section uses a semi-infinite solid conduction analytical model to calculate the expected temperature change at the substrate's surface.

Prior to the baseline sensor design, an embedded sensor, Fig 2-1b, was established as infeasible. The temperature fluctuation amplitude versus depth into the substrate was analyzed using a semi-infinite solid model[18], Eq 2.1, with a unit amplitude sinusoidal surface heat flux, $\sin(\omega t)$.

$$T = \frac{\sqrt{\kappa}}{k\sqrt{\omega}} e^{\frac{x\sqrt{\omega}}{\sqrt{2\kappa}}} \sin\left[\omega t - \frac{1}{4}\pi - x\sqrt{\frac{\omega}{2\kappa}}\right] \qquad (2.1)$$

where T is temperature, κ is the thermal diffusivity (4.23 x 10^{-5} $\frac{m^2}{s}$), ω is frequency (1.26 x 10^6 $\frac{rad}{s}$), t is time, x is depth into the substrate, and k is the thermal conductivity (70 $\frac{W}{m \bullet K}$). The resulting temperature fluctuation caused by a sinusoidal surface heat flux with a 1 $\frac{W}{m^2}$ amplitude is 4.67 x 10^{-11} K at the surface. For the expected surface heat flux amplitude, 2.5 x 10^5 $\frac{W}{m^2}$, the temperature fluctuation at the surface is 11 μK, which is not detectable. The heat flux characteristics will be discussed later in this chapter. However, the temperature fluctuation amplitude attenuates by only 5 % at 0.5 μm below the surface according to the model. Thus, a 0.5 μm sensor was approximated as isothermal along its thickness for the analysis that follows.

2.3 Structural Analysis

The sensor will be subjected to primary excitation frequency of 200 kHz when operated at the maximum design rotor speed. The sensor's mechanical natural frequency must be much greater than 200 kHz to avoid resonance.

The sensor was modeled as a beam with both ends fixed. The natural frequency for the first mode is given by Eq 2.2[19]

$$n = \left(\frac{1.5\pi}{l}\right)^2 \sqrt{\frac{EI}{m}} \qquad (2.2)$$

where n is the natural frequency, l is the length, E is the Young's modulus, I is the moment of

inertia, and m is the mass. Substituting the Young's modulus, 200 GPa[20], and polysilicon's density, 2330 $\frac{kg}{m^3}$, into Eq 2.2 yields Eq 2.3.

$$n = 59,331\frac{t}{l^2} \tag{2.3}$$

2.4 S/N Analysis

The S/N is important for a sensor and was used determine the sensor's dimension. The sensor's signal is a voltage change caused by the flow heating or cooling the sensor. The noise sources that were considered are Johnson noise, which is due to the sensor's temperature and $1/f$ noise, which becomes less important at high frequencies. The S/N was calculated using Eq. 2.4[21]

$$\frac{S}{N} = \frac{\alpha^2 \left(i^2\frac{\rho l}{wt}\right)\Delta T^2}{\left[4kT + 2ei\frac{\rho l}{wt}\right]B} \tag{2.4}$$

where α is the TCR, i is current, ρ is the resistivity, ΔT is peak-to-peak sensor temperature fluctuation, k is the Boltzman's constant, T is the sensor temperature, e is an electron charge, and B is the bandwidth. As shown in the equation, the S/N is most dependent on the TCR and the sensor's temperature change.

In order to calculate the sensor's S/N, the sensor's temperature fluctuation is required. However, the flow conditions that the sensor will experience are required to calculate the sensor's temperature fluctuation. Thus, the flow conditions will be discussed first, followed by the sensor's temperature fluctuation calculation, and then by the S/N calculation.

2.4.1 Flow Conditions

The flow properties necessary for the sensor's temperature fluctuation calculation are the heat flux, heat transfer coefficient, and mean flow temperature profiles. They were obtained from a 3-D FLUENT simulation, performed by Yifang Gong of MIT's Gas Turbine Laboratory[22], of the flow above the compressor blades. The boundary conditions are summarized in Table 2.2. The simulation was done by specifying the inlet and outlet pressures and temperatures, wall temperature, geometry, and rotor speed. FLUENT uses a steady Navier-Stoke solver to

26

Table 2.2: 3-D FLUENT simulation boundary conditions. The simulation results presented in this chapter are based on these boundary conditions.

|	
Blade height	400 μm
Wall temperature	800 K
Blade base temperature	875 K
Mass flowrate	0.25 $\frac{g}{sec}$
Isothermal	

converge to a flow field.

The heat flux, Q", profile was obtained using Eq 2.5,

$$Q" = \left[k_{air} \frac{dT}{dx} \right]_{x=wall} \tag{2.5}$$

where k_{air} is the conductivity of air, 0.04 $\frac{W}{m \cdot K}$, and $\frac{dT}{dx}$ was estimated from a sixth-order polynomial curve-fit of the flow temperature profile above the wall from the FLUENT simulation, Figs 2-2 and 2-3. In the region between blades, the temperature profile less than 20 μm above the wall was curve-fit to estimate $\frac{dT}{dx}$ at the wall, Fig 2-2b. The word "profile" is used in two senses. The heat flux, heat transfer coefficient, and mean flow temperature profiles represents what the sensor experiences as the blades pass and is in the time or angular position domain, as illustrated in Fig 2-4. The flow temperature profile is the flow temperature at varying distances above the wall. The 15 flow temperature profiles, Figs 2-2 and 2-3, correspond to 15 angular positions or different stages of the blade passing.

The heat flux profile, Fig 2-6, approximates the heat flow into and out of the sensor. This approximation is reasonable if the sensor's presence does not change the flow significantly, which is true if it is approximately a flat surface, and there are no other significant heat sources. However, this approximation may not be reasonable if heat dissipation from electrical current is not negligible compared to the heat flux from the flow. In this case, the heat transfer between the sensor and the flow can be approximated using the heat transfer coefficient and mean flow temperature profiles, where the mean flow temperature is defined as the flow temperature that is driving the heat transfer at a particular angular position and is not the arithmetic mean of the whole temperature profile above the wall. The mean flow temperature profile, Fig 2-7, was approximated from the temperature profiles, Figs 2-2 and 2-3. The heat transfer coefficient

27
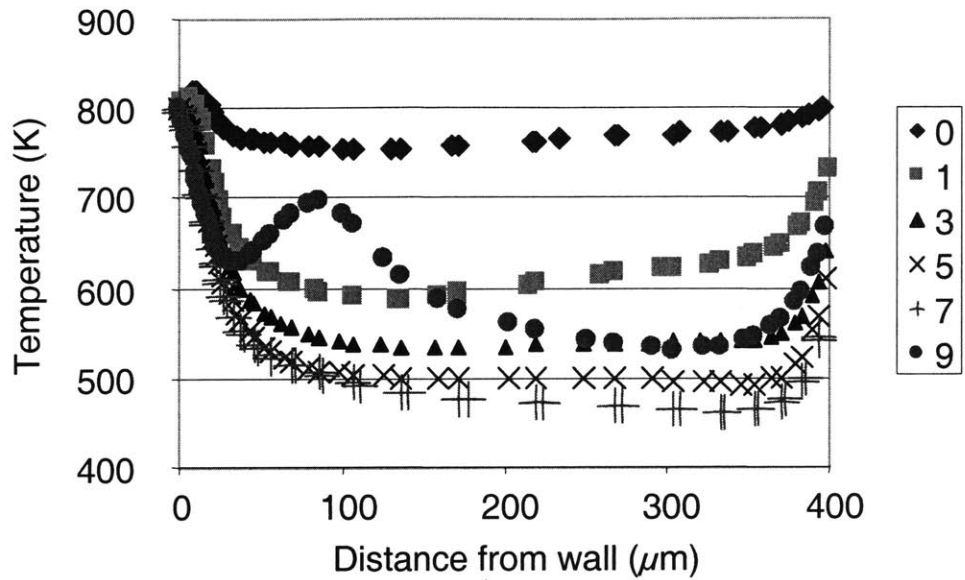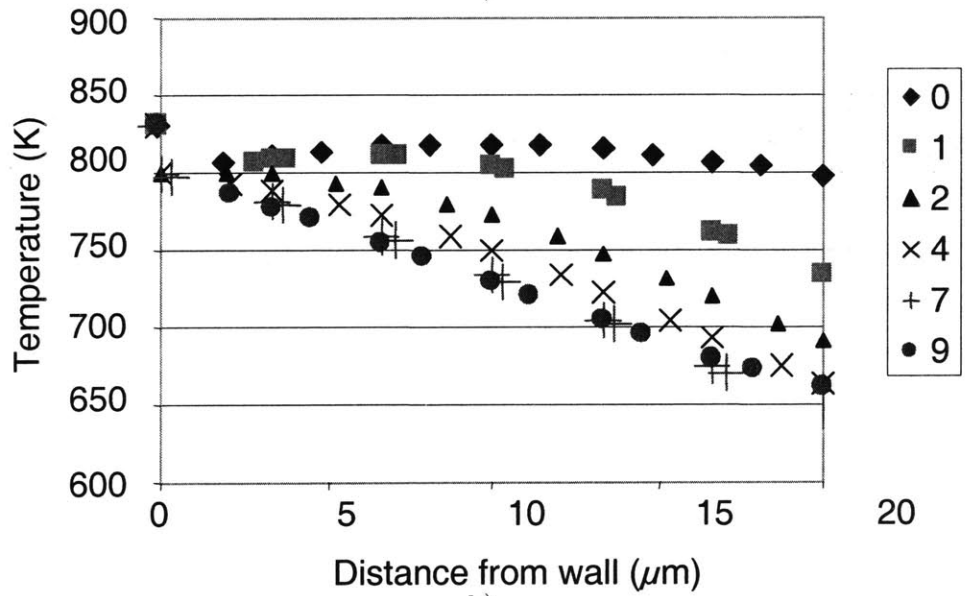
Figure 2-2: Temperature profiles extracted from a FLUENT simulation. Temperature profiles above the wall at 15 angular positions. Angular position is reference from an arbitrary value. One blade passing corresponds to 36 degrees difference in angular position. a) Temperature profiles between blades. b) Temperature profiles between blades from 0 to 20 microns from the wall.
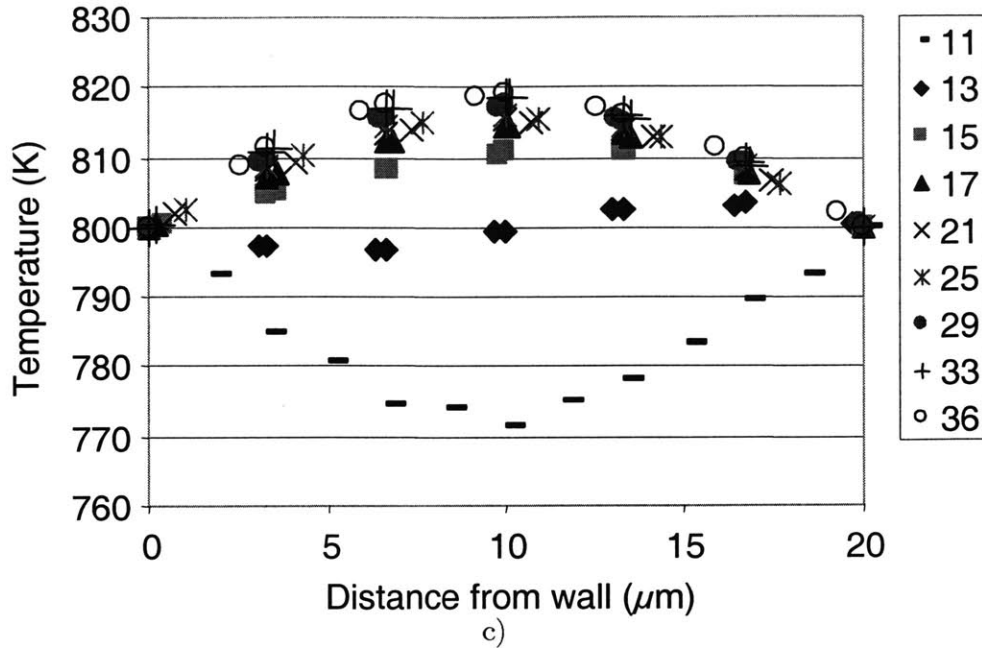
Figure 2-3: Temperature profiles extracted from a FLUENT simulation. Temperature profiles above the wall at 15 angular positions. Angular position is reference from an arbitrary value. One blade passing corresponds to 36 degrees difference in angular position. Temperature profiles above a blade.
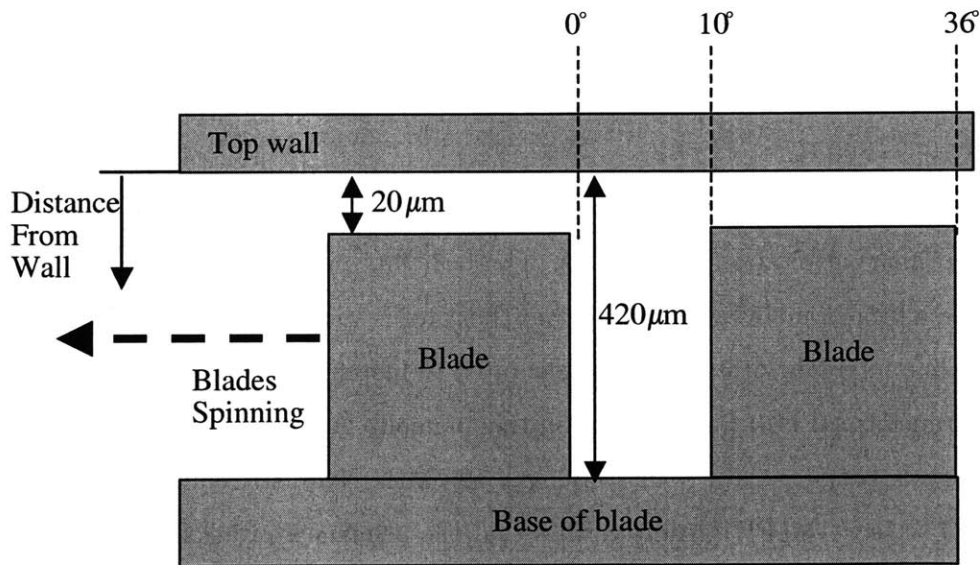

Figure 2-4: A diagram of the compressor blade and top wall that shows the angular positions corresponding to those used in the next 3 figures. The temperature profiles in the next 3 figures are at different angular position, where 36 degrees correspond to one blade passing period.
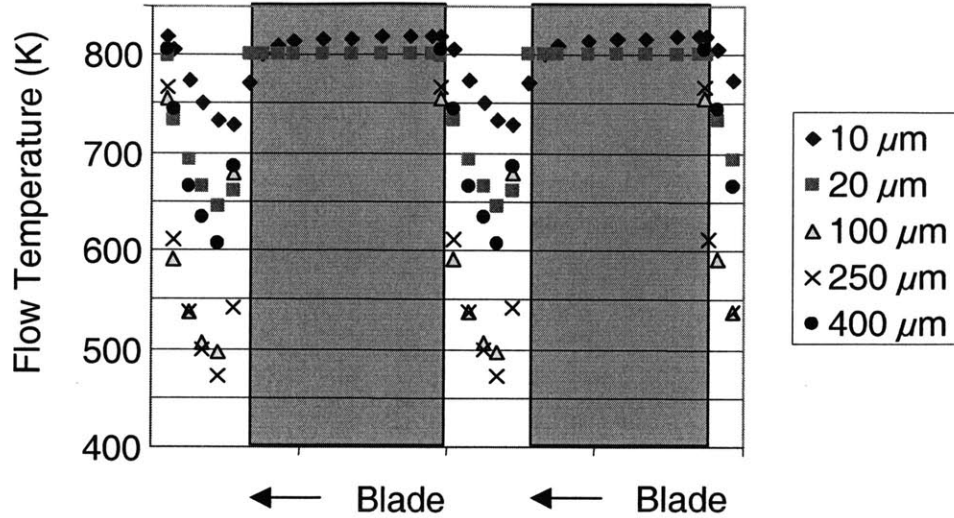
Figure 2-5: Flow temperature at various distances away from the wall, bottom surface of Level 2. The constant 800 K at 20 microns away from the wall when the blades pass corresponds to the blade temperature.

profile, Fig 2-8, was calculated using the heat flux profile and mean flow temperature profile using Eq 2.6

$$h = \frac{Q"}{(T_{flow} - T_{wall})} \qquad (2.6)$$

where $T_{wall} = 800$ K.

The frequency content of the heat flux profile was used to verify that the sensor will experience a primary excitation at 200 kHz. The heat flux profile was converted from the angular domain to a time domain by assuming that the rotor is spinning at 1.2 million rpm. Data points at fixed time intervals were manually generated to match the heat flux curve, Fig 2-9. A finite Fourier transform (FFT) was perform on the manually generated data points, which had 0.125 μsec intervals between data points giving a 400 MHz Nyquist frequency and 256 data points over 31.875 μsec. The FFT result verifies that the primary excitation frequency is at 200 kHz, Fig 2-10.
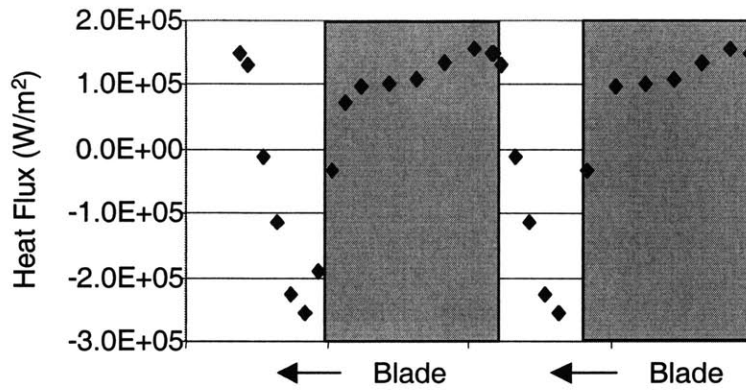
Figure 2-6: Profile of heat flux into the wall as blades pass. One blade passing is equal to a 36 degrees angular position difference. The heat flux profile is used to approximate the heat flux into the sensor if the sensor is not perturbing the flow significantly, which is reasonable at low driving current and when the sensor is close to the wall.
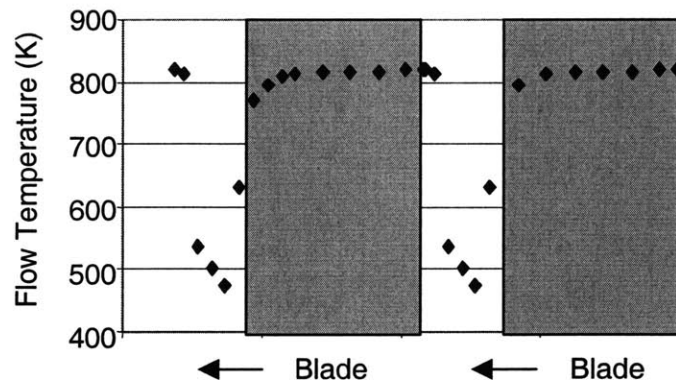

Figure 2-7: Mean flow temperature profile is the flow temperature that is driving the heat transfer. It is obtained from Fig 2-2. Instead of the heat flux profile, it is used with Fig 2-6 to approximate the heat transfer into the sensor when Joule heating is considered.
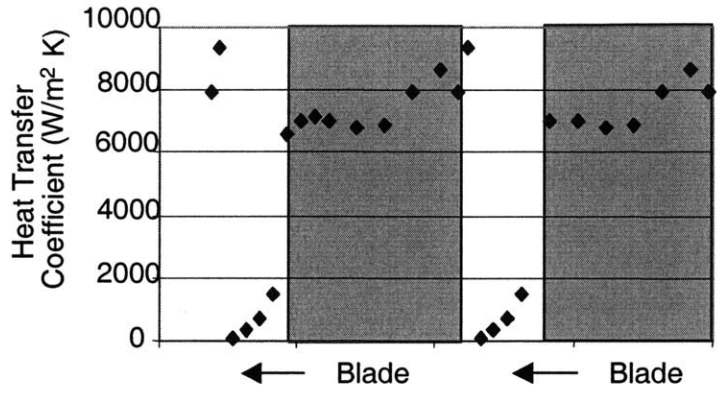
Figure 2-8: Heat transfer coefficient profile. It is an approximation of the heat transfer co-
efficient between the sensor and the flow as the rotor spins at 1.2 million rpm and with the
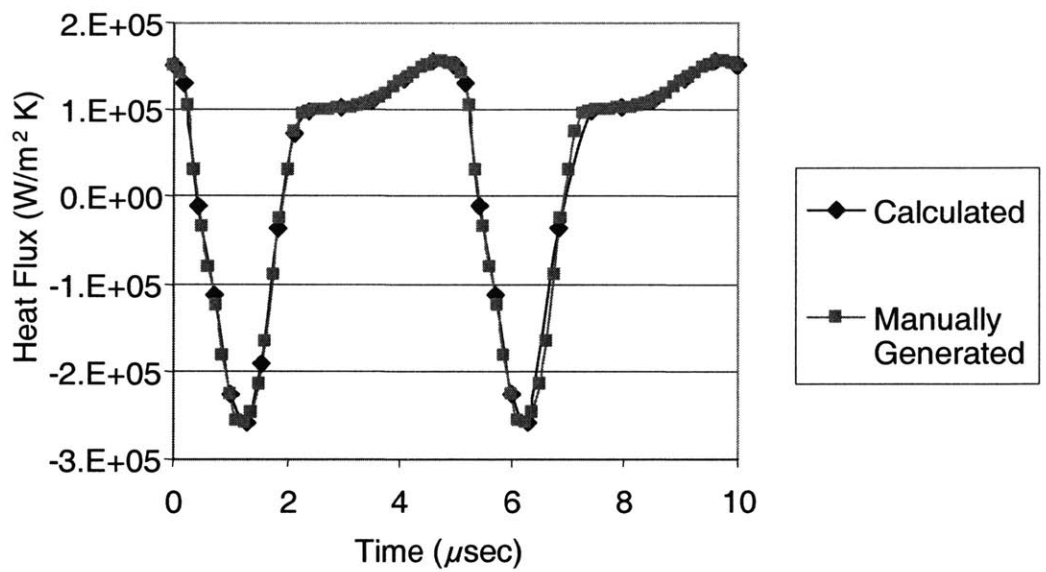FLUENT simulation boundary conditions. It is calculated using Fig 2-4 and Fig 2-5.

Figure 2-9: Heat flux profile from Fig 2-4 in the time domain. A manually generated heat flux
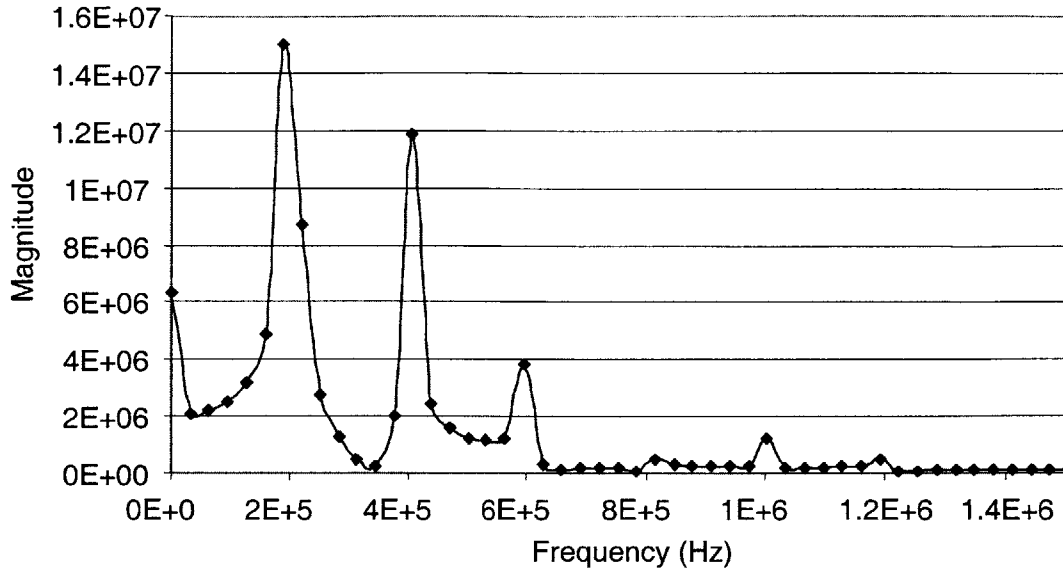profile that will be used in a finite Fourier transform analysis.

Figure 2-10: FFT of the manually generated heat flux profile. The primary excitation frequency is 200 kHz.

2.4.2   Numerical Model

The sensor's temperature fluctuation was calculated using a numerical model coded in MAT-LAB, Appendix A. The numerical model calculates the temperature at various locations along the length of a sensing element. In the model, a sensing element is divided into n nodes, where the end nodes are held at the wall temperature. The top surface of each node experiences convection from or to the flow and each node conducts heat to adjacent nodes. The inputs to the model include air properties, sensor material properties, sensor's dimensions, heat transfer in terms of the heat flux profile or heat transfer coefficient and mean flow temperature profiles. The sensing element's average temperature fluctuation was calculated from the numerical model's output and used to determine its average resistance change. The numerical model was verified with analytical solutions for a finite length cylinder subjected to a step change in flow temperature and an infinite length cylinder subjected to a sinusoidal flow temperature. Subsequently, the geometry of the sensor was adjusted to model a rectangular sensor.

33

2.4.3 Numerical Model Verification

The first analytical solution, Eq 2.7 [23], used to verify the numerical model is a steady-state solution of a finite length cylinder subjected to a step change in flow temperature, where the ends are maintained at a constant temperature. The analytical solution provides the steady-state temperature at different axial position of the cylinder.

$$T = \frac{T_0 \sinh \mu(l - x) + T_0 \sinh \mu x}{\sinh \mu l} \tag{2.7}$$

$$\mu = \sqrt{\frac{hp}{kA_{cross}}} \tag{2.8}$$

where T_0 is the end temperature, h is the heat transfer coefficient, p is the perimeter, k is the conductivity, and A_{cross} is the cross-sectional area.

Analytical, Fig. 2-11, and numerical solutions, Fig. 2-12, of 0.1 μm, 1 μm, and 10 μm diameter cylinders subjected to a flow temperature of 810 K indicate that both steady-state solutions agree. The steady-state temperatures from the numerical solution at the axial center of the cylinder and at 5 μm from the ends are within 0.5 K of the corresponding temperatures from the analytical solution, as shown in Fig 2-13. At the cylinder's center, the steady-state temperature from the analytical solution for 0.1 μm, 1 μm, and 10 μm diameters are 808.8 K, 802.8 K, and 800.4 K, respectively, and those from the numerical solution for 0.1 μm, 1 μm, and 10 μm diameters are 808.4 K, 802.5 K, and 800.3 K, respectively. At 0.5 μm from the cylinder's end, the steady-state temperature from the analytical solution for 0.1 μm, 1 μm, and 10 μm diameters are 804.0 K, 801.0 K, and 800.3 K, respectively, and those from the numerical solution for 0.1 μm, 1 μm, and 10 μm diameters are 803.5 K, 800.7 K, and 800.1 K, respectively.

The second analytical solution, Eq 2.9 [24], used for numerical model verification is a temperature response solution of an infinite length cylinder with zero initial temperature immersed in a flow with a temperature $V \sin(\omega t)$.

$$T = \text{Re} \left\{ \frac{HVI_0 \left[r\sqrt{\frac{j\omega}{\kappa}} \right] e^{j(\omega t)}}{j \left[\sqrt{\frac{j\omega}{\kappa}} I_1 \left(a\sqrt{\frac{j\omega}{\kappa}} \right) + HI_0 \left(a\sqrt{\frac{j\omega}{\kappa}} \right) \right]} \right\} + transient \tag{2.9}$$
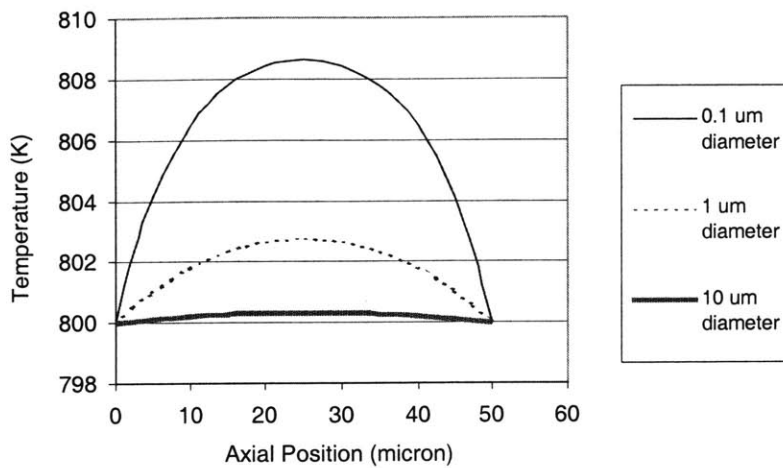
Figure 2-11: Analytical solution of the steady state temperature profile along a finite length cylinder subjected to a step change in flow temperature. The ends are fixed at the initial temperature, 800 K, and the flow temperature is 810 K.
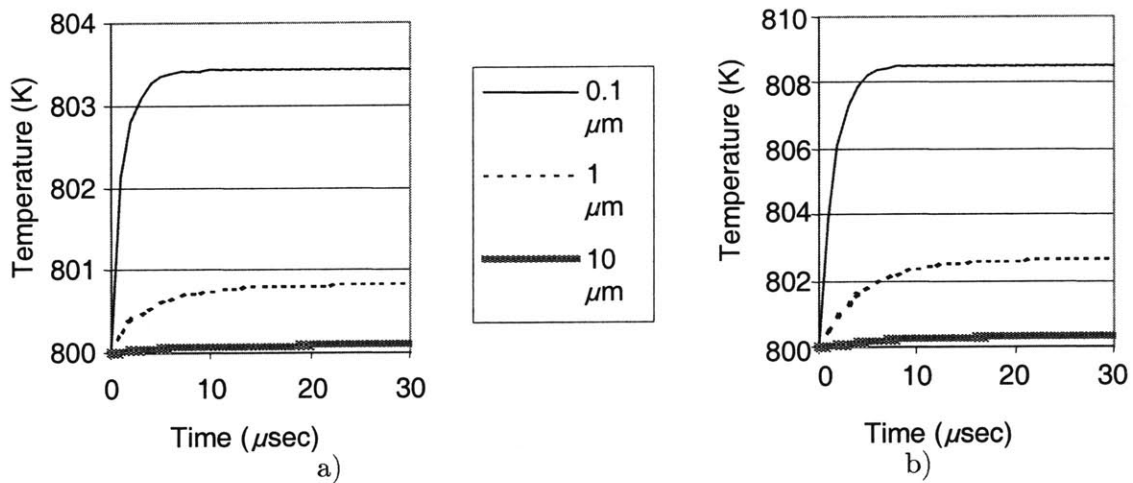

Figure 2-12: Numerical solution from a MatLab simulation of the temperature response at two axial locations of a 50 microns long cylinders subjected to a step change in flow temperature. The ends are fixed at the initial temperature, 800 K, and the flow temperature is 810 K. The steady state temperature corresponds to those of the previous figure. a) Temperature response at the axial center. b) Temperature response at 0.5 micron from the end.
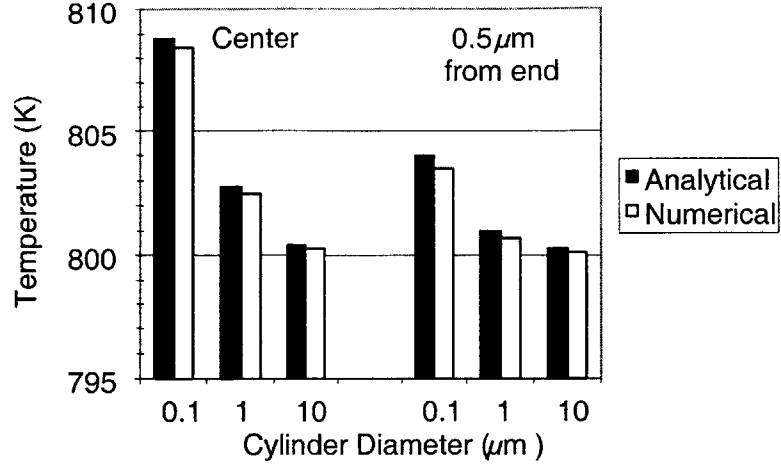
Figure 2-13: A comparison of the steady-state temperature from the analytical, Fig 2-9, and numerical solutions, Fig 2-10, at two axial locations for three diameters.

$$H = \frac{h}{k} \tag{2.10}$$

where I_0 and I_1 are the modified Bessel functions, r is radial location, a is the radius, and κ is the thermal diffusivity.

The temperature fluctuation from the analytical solution of an infinite length cylinder, Fig.2-14, was compared to the temperature fluctuation from the numerical solution of a finite-length cylinder, Fig. 2-15. The temperature response at the axial center of a long cylinder approaches that of an infinite length cylinder because the end-effects, decreasing the average temperature fluctuation, become negligible as the cylinder's length increases. The peak-to-peak temperature fluctuations from the analytical solution are 0.8 K and 8 K for the 10 μm and 1 μm diameter cylinders, respectively. They agree with the numerical solution, which are 0.8 K and 7.8 K for the 10 μm and 1 μm diameter cylinder, respectively, as shown in Fig 2-16.

Furthermore, the analytical solution indicates that the cylinder has almost constant radial temperature, Fig 2-14b. The temperature at 95% of the radius and at the radial center differ by less than 1%. Thus, the approximation that the temperature along the sensor's thickness is isothermal is further justified.

After verifying that the numerical model, it was adjusted to model a rectangular beam
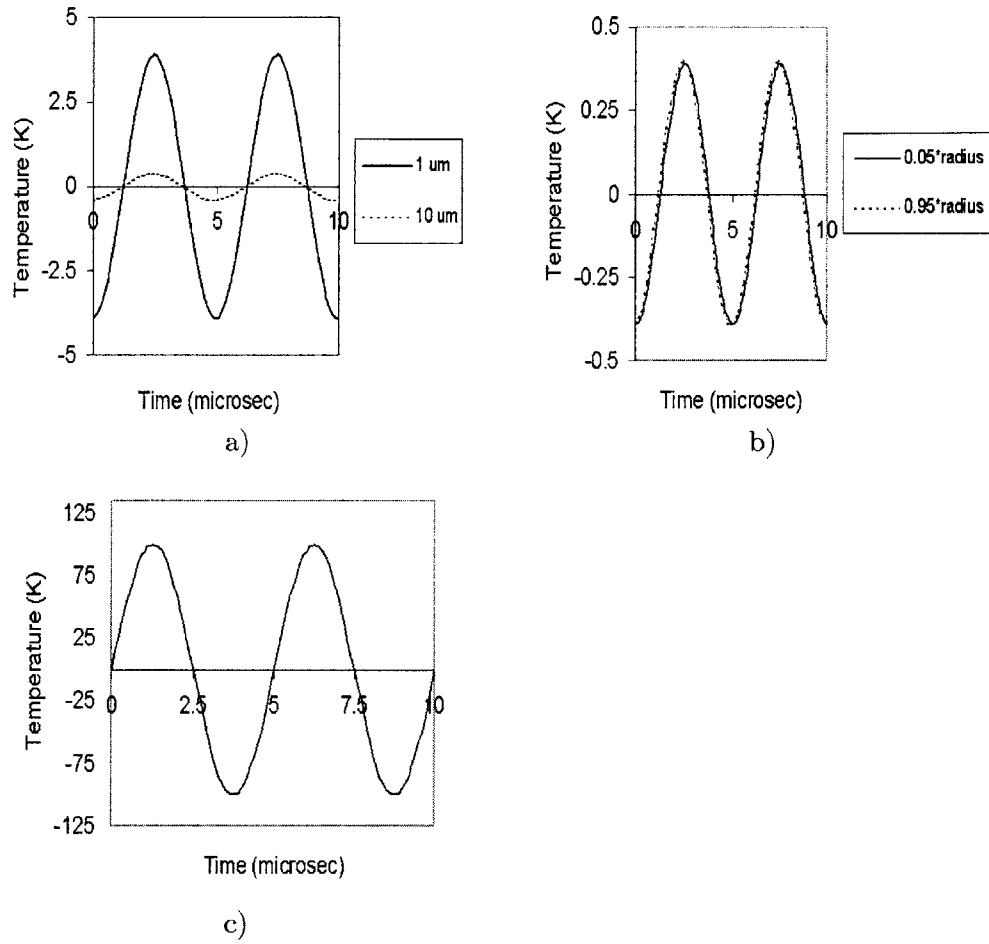
36

Figure 2-14: Analytical solutions for the temperature response of an infinite length cylinder subjected to a sinusoidal flow temperature. a) Temperature response at radial position = 95microns diameter cylinder. c) The sinusoidal flow temperature.

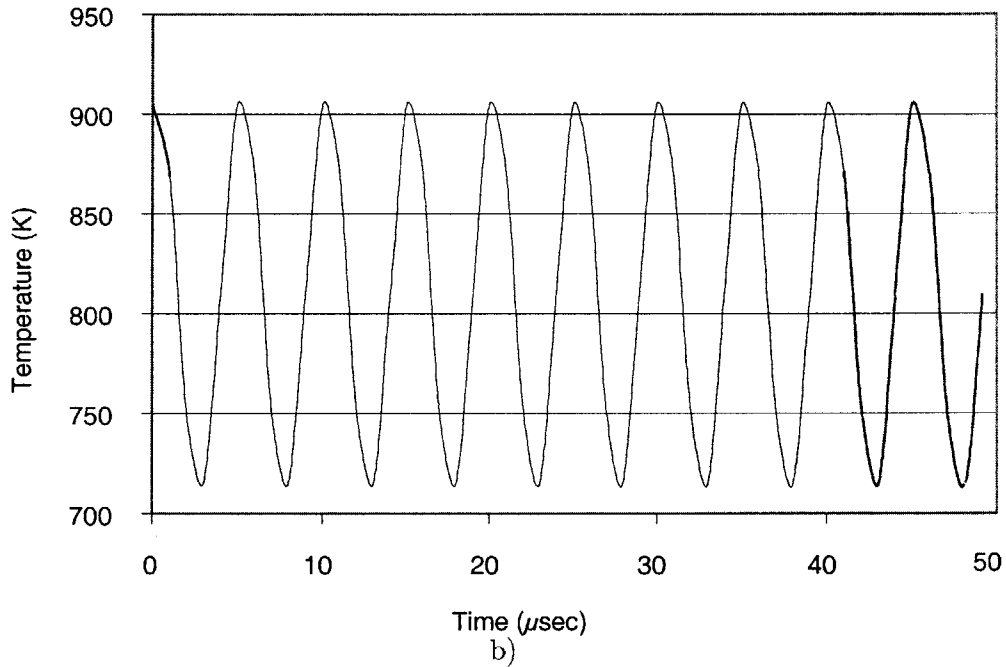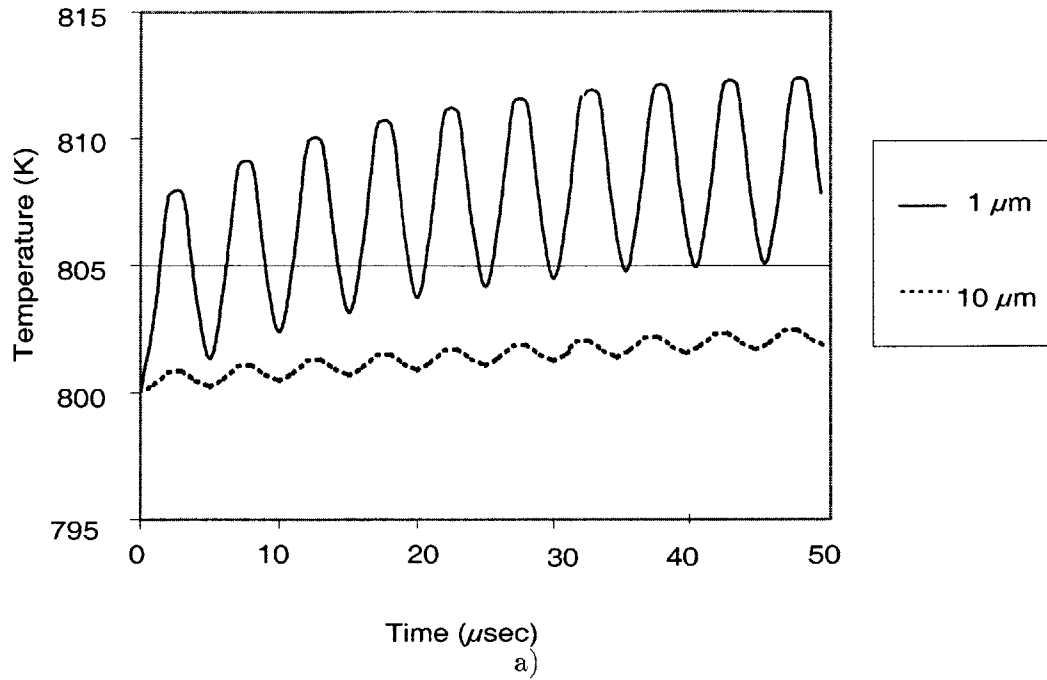Figure 2-15: Numerical solutions from a MatLab simulation of the temperature response of a 200 microns long cylinder subjected to a sinusoidal flow temperature. a) Temperature response of two cylinders, 1 micron and 10 microns diameters. b) The sinusoidal flow temperature, 810 +/- 100 K. The peak-to-peak fluctuation from a) figure corresponds to the peak-to-peak temperature fluctuation in the Fig. 2-12a.
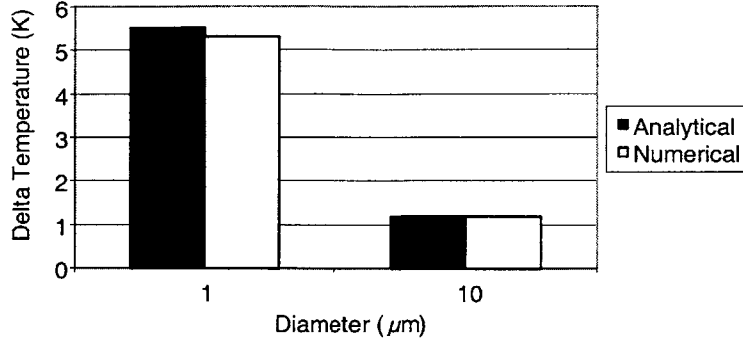
38

Figure 2-16: A comparison of the analytical and numerical solutions of a long cylinder subjected to a sinusoidal flow temperature.

rather than a cylinder by changing the areas, cross-sectional and surface area, that experience heat flux. The cross-section was changed from a circle to a rectangle. In the cylinder case, heat flux was imposed on the entire surface area except on the ends. However, the model was changed such that only the rectangular sensor's top surface experiences heat flux from the flow.

2.4.4 Sensitivity vs. Sensor Length Analysis

Since natural frequency is inversely proportional to the square of the sensor's length, it is desirable to have a short sensor to obtain high natural frequency and robustness while sacrificing minimal sensitivity. The sensor's sensitivity is given by Eq 2.12,

$$\frac{\Delta R}{R} = \alpha \Delta T \tag{2.11}$$

where $\frac{\Delta R}{R}$ is sensitivity, α is the temperature coefficient of resistivity (0.002/°C), and ΔT is the sensor's temperature fluctuation. The sensitivity versus length for various thicknesses are shown in Fig 2-17. The sensitivity is independent of the sensor's width because its temperature fluctuation is independent of its width. The sensor's temperature fluctuation is obtained from the numerical model with the appropriate dimension inputs and the heat flux profile.

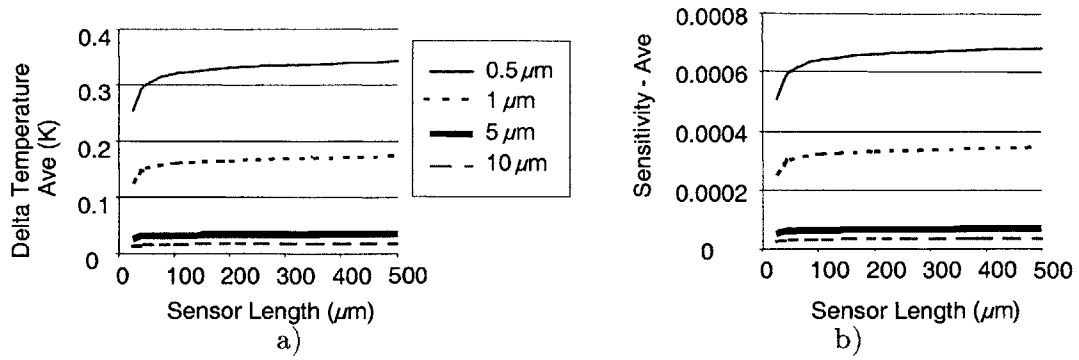$$\frac{\Delta R}{R} = \alpha \Delta T \tag{2.12}$$

Figure 2-17: Sensitivity analysis of a 4 microns wide poly-Si sensor of various thicknesses subjected to the heat flux profile calculated from FLUENT. The sensitivity analysis was obtained using the heat flux profile to model the sensor's temperature fluctuations. (a) The sensor's temperature fluctuation averaged over the sensor's length. (b) The sensitivity corresponding to the average sensor temperature fluctuation.

where $\frac{\Delta R}{R}$ is sensitivity, α is the temperature coefficient of resistivity (0.002/°C), and ΔT is the sensor's temperature fluctuation.

Fig 2-18 shows the sensitivity normalized by the maximum sensitivity possible, which is that of a long sensor where the end-effects are negligible. A 50 μm sensor provides about 85% of the maximum sensitivity. At long lengths, the loss in structural integrity from decreasing natural frequency begins to outweigh the gains from increasing sensitivity. The natural frequency of a 50 μm long x 0.5 μm thick beam is 11 MHz, which is over one magnitude larger than the maximum primary excitation frequency.

2.4.5 S/N Analysis

As previously mentioned, a 50 μm long x 0.5 μm thick sensor has sufficient sensitivity to produce a detectable signal and structural integrity to survive the pressure fluctuation excitations. The S/N can be increased while maintaining the sensitivity and structural integrity by placing multiple 50 μm lines in parallel physically and in series electrically as shown in Fig. 1-1. The number of lines is restricted by the 50 x 50 μm workspace. The S/N analysis for a 50 μA driving current shows about a 250% increase in S/N by using a 250 μm long sensor (five 50 μm lines). Furthermore, a S/N of up to 130 is obtainable by using a 4 μm wide, 0.5 μm thick, and 300 μm (six 50 μm lines) long sensor, as shown in Fig 2-19. The S/N analysis calculation shown in Fig 2-19 accounts for only Johnson and 1/f noises and does not consider noise from the electronics.
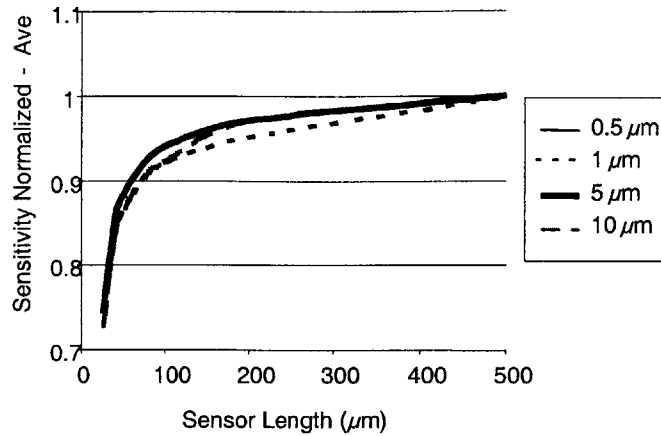
Figure 2-18: Sensitivity analysis for various sensor thicknesses. The sensitivity is normalized by the maximum sensitivity, which is approximately the sensitivity of an infinitely long sensor.

Therefore, the device's S/N will probably be lower than these calculated values. However, this analysis is useful in showing the trends and parameters affecting S/N.

2.5 Joule Heating

The analysis thus far has neglected Joule heating. To include the electrical heat dissipation, the heat transfer coefficient and mean flow temperature profiles must be used instead of the heat flux profile to approximate the heat flux from the flow into the sensor. The temperature response from the numerical model of a 4 μm wide, 0.5 μm thick, and 50 μm long polysilicon sensor, with no current, subjected to heat flux defined by the heat flux profile and by the heat transfer coefficient and mean flow temperature profiles are shown in Figs 2-20a and 2-21a, respectively. The peak-to-peak temperature fluctuation from the heat flux profile is 10% lower than that of the heat transfer coefficient and mean flow temperature profiles, ~0.32 K and ~0.35 K, respectively. The temperature response in Fig 2-21a is used as a reference to observe any changes caused by Joule heating.

The effect of Joule heating from the driving current is shown in Fig 2-22a. The region of constant temperature fluctuation up to approximately 50 μA driving current corresponds to a cold-film anemometer. Above 50 μA, the sensor becomes a hot-film anemometer and the sensor
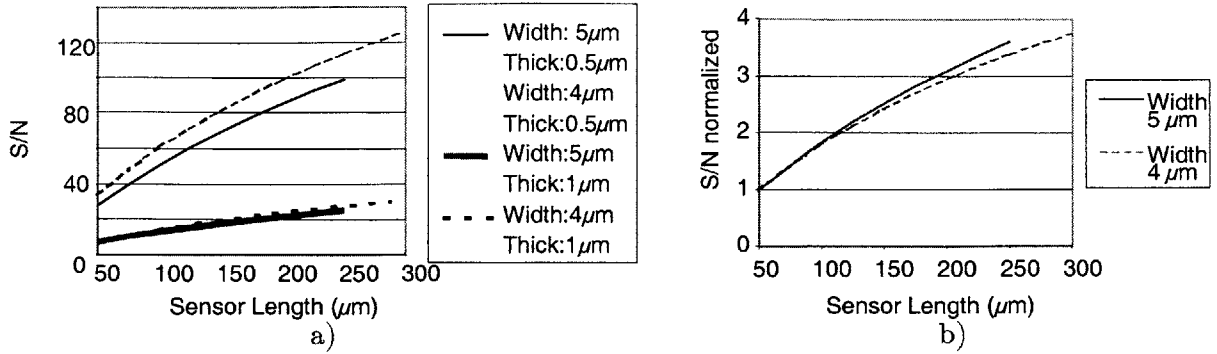
41

Figure 2-19: S/N analysis of a polysilicon sensor with an average sensor temperature fluctuation of 0.3K, corresponding to a 50 microns long sensor with the ends held at constant temperature and subjected to the heat flux profile. (a) S/N of n, length = n x 50 microns, sensors place in electrical series. (b) S/N normalized by the S/N of one 50 microns sensor.

temperature fluctuation increases exponentially. Thus, the previous S/N analysis where Joule heating was neglected is valid because the current does not significantly change the sensor's temperature fluctuation at 50 μA.

The S/N increases approximately exponentially with driving current, Fig 2-22b. However, it is not physically possible to have a driving current larger than a few mA because the steady-state temperature approaches the melting temperature, 1600 K, of silicon, Fig 2-23.

2.6 Sensor Design

Based on the analysis presented in this chapter, the sensor design is a 0.5 μm thick serpentine polysilicon structure, as shown in Fig 2-1. A serpentine structure increases the overall sensor length given a certain workspace, which is the distance between the compressor blades. Additional sensing elements, where an element is a span across the undercut, increase the signal as discussed in the previous sections. The sensor's linewidth was restricted by the spacing between the compressor blades and by the fabrication equipment available. All the sensing elements must fit within the spacing between blades and the spacing between the sensing elements must be sufficiently wide to pattern etch holes to form the undercut. Thus, alignment accuracy and the width of the etch holes are the main considerations in designing the distance between the sensing elements. The etch holes cannot be made much less than 2 μm because the etch rate is inversely related to the etch holes' dimensions and patterning repeatability decreases as
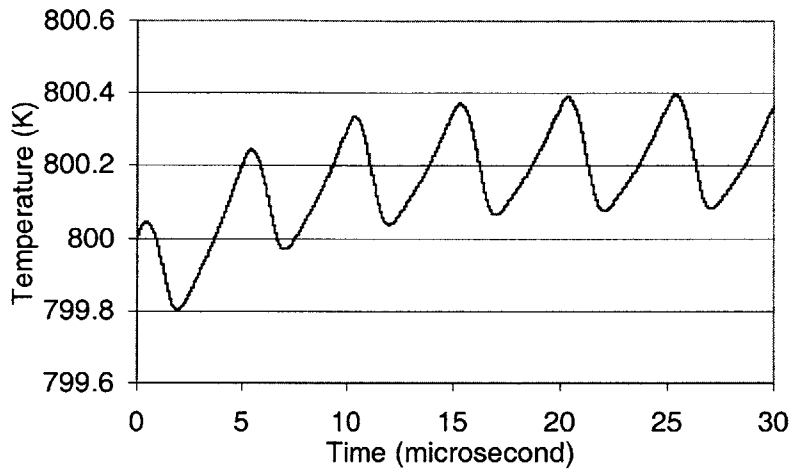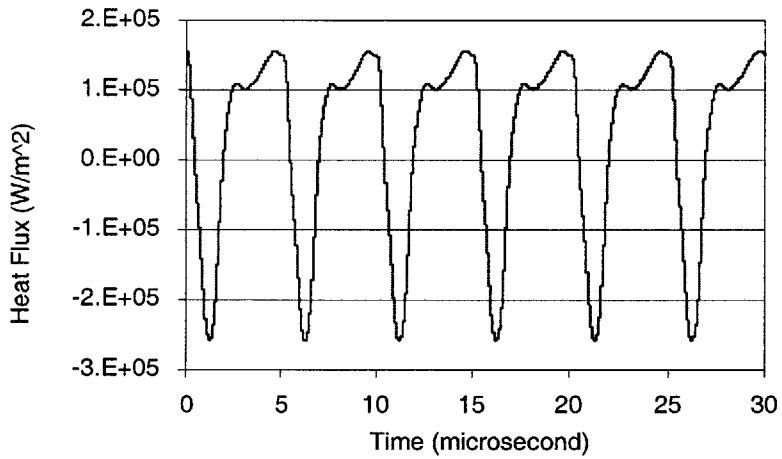
Figure 2-20: a) Numerical model result showing the temperature response at the axial center of a 50 micron long x 4 micron thick polysilicon subjected to the heat flux profile. b) The heat flux profile used in the numerical model.
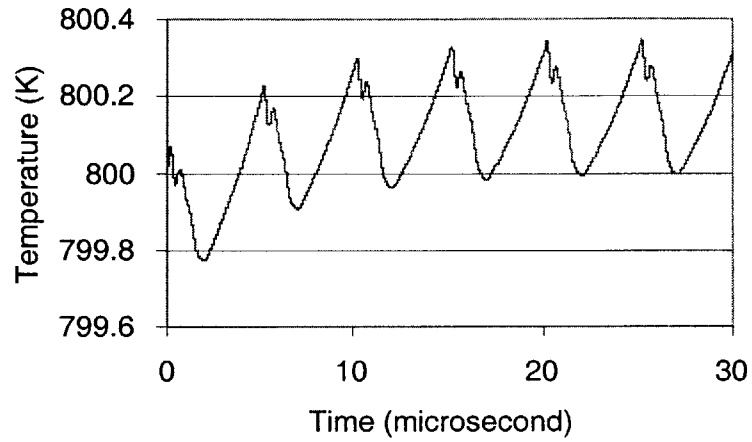
a)
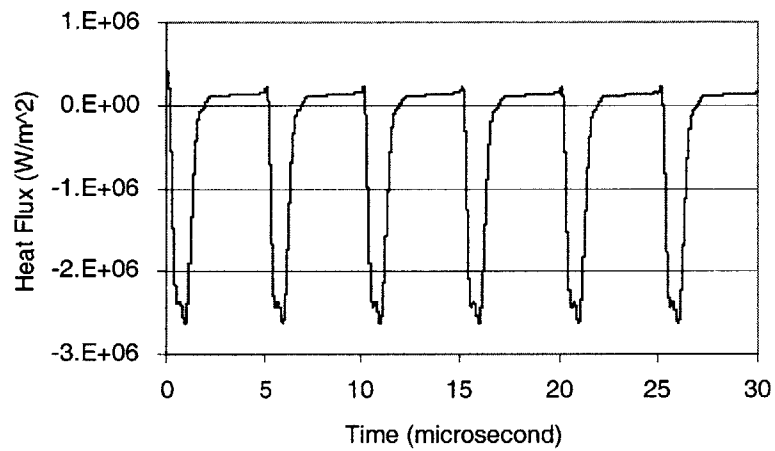
b)

Figure 2-21: a) Numerical model result showing the temperature response at the axial center of a 50 micron long x 4 micron thick polysilicon subjected to the heat transfer coefficient and mean flow temperature profiles. b) The heat flux into the structure at the axial center calculated using the heat transfer coefficient and mean flow temperature profiles.
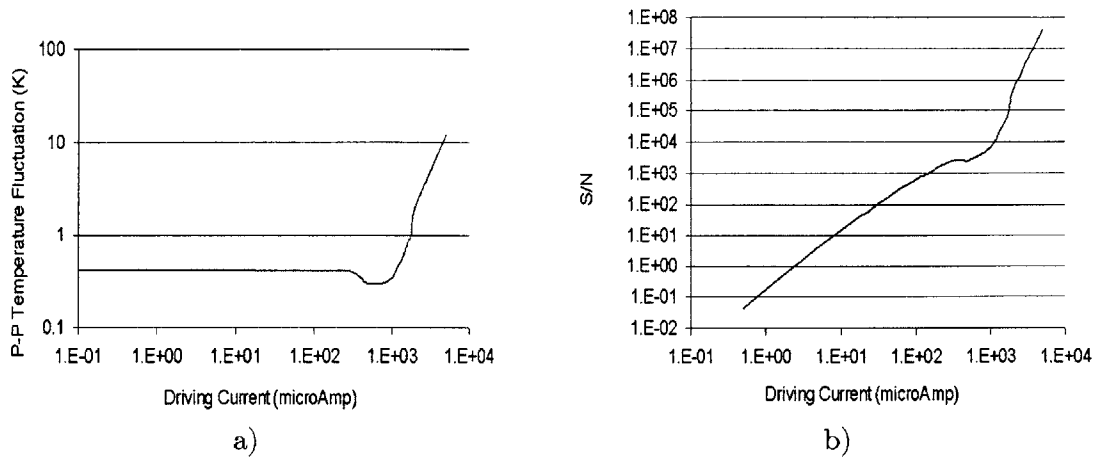
Figure 2-22: a) The sensor's temperature fluctuation from Joule heating and heat transfer from the flow. The heat transfer from the flow is approximated using the heat transfer coefficient and mean flow temperature profiles. b) S/N analysis using the sensor's temperature fluctuations from a).

Figure 2-23: Steady state temperature of a 50 μm long polysilicon sensor with Joule heating and heat transfer calculated from the heat transfer coefficient and mean flow temperature profiles. Driving currents greater than approximately 3.5 mA is not feasible because the sensor will melt.

dimensions become smaller.

Chapter 3

Fabrication

The sensor is a serpentine polysilicon structure with the ends supported on silicon dioxide and the middle section free-standing. The silicon dioxide layer electrically isolates the polysilicon from the silicon substrate. The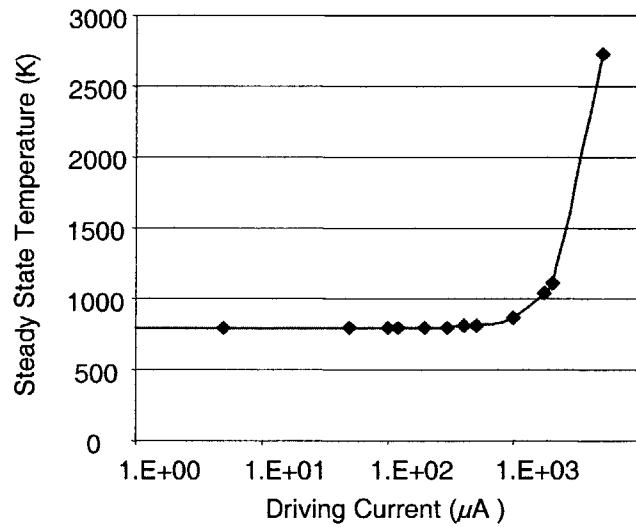 middle sections are released to increase thermal isolation. The sensor's baseline design dimensions are 4 μm wide, 0.5 μm thick, and each span is 50 μm. It was fabricated using a two-mask process and standard silicon processing equipment.

This chapter describes the sensor fabrication process. The overall fabrication process is first described followed by a discussion of the two main challenges in the fabrication process development: the undercut etch and the metal deposition. The undercut etch is for the sensor's thermal isolation and is accomplished with a two-step dry etch process. The metal deposition is for electrical connection and is accomplished with a shadow mask process.

3.1 Facility Description

The sensor was fabricated in MIT's Microsystems Technology Laboratories (MTL). MTL has a class 10 cleanroom facility, Integrated Circuits Laboratory (ICL), and a class 100 cleanroom facility, Technology Research Laboratory (TRL). The sensor's oxide growth, polysilicon and oxide depositions, anneals, and shallow etches were done in ICL; whereas, photolithography, deep etches, and metal depositions were done in TRL. Additional information on MTL's facility can be found in [25].

3.2 Fabrication Process Flow

The fabrication process flow is summarized in Table 3.1. The masks design are in Appendix B. In addition, the fabrication process flow with recipes specific to MTL's equipment are in Appendix C.

A description of the key steps follows:

Start with a blank single-side polished Si wafer: <100>, B dopant, res high= 10.000, res low= 1.000;

2) Grow 0.5 μm of thermal oxide at 950 °C using a Bruce Technologies International (BTI) BDF-4 Furnace System (ICL tube A3). The thermal oxide is for electrical isolation;

3) Deposit 0.5 μm of polysilicon at 560 °C using a BTI furnace (ICL tube A6) with SiH_4. Polysilicon deposited at 560 °C is deposited in an amorphous state and then crystallizes, which has more controllable properties than as-deposited polysilicon at higher temperatures[26]. In addition, Jiang observed that at high doping levels the TCR of the polysilicon deposited in an amorphous state is about 50% higher than that of as-deposited polysilicon[27];

4) Ion implant at 80 keV with a 5 x $10^{16}cm^{-2}$ dose of boron (via Ion Implant Services of Sunnyvale, CA). The corresponding doping concentration, 10^{20} cm^{-3}, has been observed to give the highest positive TCR, 0.2%/°C[28];

5) Deposit 0.05 μm of low temperature oxide (LTO) using a BTI furnace (ICL tube A7) for dopant capping in the subsequent anneal;

6) Anneal at 900 °C for 1 hour using a BTI furnace (ICL tube A2) to activate the dopants and to repair the damage caused by the ion implantation;

7) Remove the LTO with a buffered oxide etch (BOE);

9) Dry anisotropic polysilicon etch, 0.5 μm, using an Applied Materials Etcher 5000 (AME 5000) to pattern the sensor;
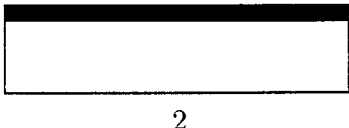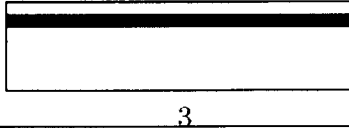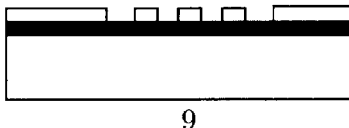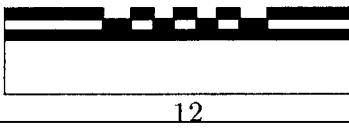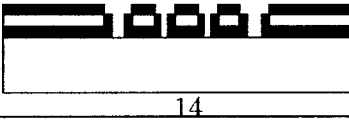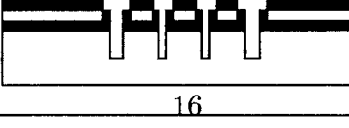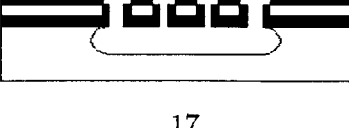
11) Deposit 0.5 μm of LTO using a BTI furnace (ICL tube A7) to serve as a masking layer for the subsequent anisotropic and isotropic silicon etches;

12) Anneal at 900 °C for 1 hour to densify the LTO using a BTI furnace (ICL tube A2);

14) Dry anisotropic oxide etch, 1 μm, using an AME 5000 to pattern the oxide mask. Seven 2 x 40 μm trenches are etched into the oxide layer;

16) Deep dry anisotropic Si etch using a Surface Technology Systems (STS) Deep Reactive

48

Table 3.1: Fabrication Process Flow

Step	Process	
1	RCA clean	
2	Grow Thermal Oxide: 0.5 μm	2
3	Deposit Poly-Si: 0.5 μm	3
4	Dope Poly-Si: Ion Implant boron 5×10^{15} cm^{-2}	
5	Deposit LTO: 0.05 μm	
6	Anneal: 900 °C, 1 hour	
7	BOE etch SiO$_2$: 0.05 μm	
8	Photolithography (Mask 1): standard resist	
9	Anisotropic etch Poly-Si: 0.5 μm	9
10	Strip photoresist: Ashing	
11	Deposit LTO: 0.5 μm	
12	Densify: 900 °C, 1 hour	12
13	Photolithography (Mask 2): standard resist	
14	Dry anisotropic etch SiO$_2$: 1 μm deep	14
15	Strip photoresist	
16	Anisotropic Etch Si: 22 min 38 sec, ~50 μm deep	16
17	Isotropic Etch Si: 6 min, ~4 μm	17
18	BOE etch SiO$_2$: 8 min, ~0.6 μm	18
19	Shadow mask for contact pad metallization	

Ion Etch (DRIE) etcher. This deep etch is the first of a two-step process to form the undercut beneath the sensor. The undercut increases thermal isolation to the sensor, which increases its thermal frequency response;

17) Dry isotropic Si etch using a STS etcher with a SF_6 flow. This etch is timed such that the Si underneath the sensor is etched and the structure is only supported at the ends;

18) Remove the oxide mask with a BOE etch. This etch is also timed such that the oxide encasing the sensing structure is removed but the oxide supporting the polysilicon sensor's ends is not overly undercut;

19) Deposit Ti and Pt at selected areas using a shadow mask process. A shadow mask process is a line-of-sight deposition process, where the desired areas for deposition are exposed via through wafer openings on a mask wafers. This shadow mask process developed for the sensor fabrication used an Electronic Vision (EV) tool for aligning the wafers and a e-beam deposition tool to deposit the Ti and Pt. The shadow mask process will be discussed in more detail later in this chapter. The metallization allows ohmic contacts for packaging. Pt is used because it is a high temperature metal, which is required for the temperature characterization, and Ti is used as an adhesion layer between the polysilicon and the Pt.

3.2.1 Thermal Isolation Undercut Etch

The thermal isolation undercut is made with a two-step dry silicon etch process: a deep anisotropic etch and an isotropic etch. The deep anisotropic etch uses a STS etcher with a recipe that alternates between etching and passivation cycles[29]. Etch rates depend on the feature size as well as the recipe's parameters. The etch rate for this geometry was characterized by using dummy silicon wafers with 1.0 μm of thermal oxide. The etch holes, 2 μm x 40 μm, were first anisotropically etched into the oxide. Subsequently, the silicon at different sections of the wafer were anisotropically etched for different times. Etch characterization results using a recipe with parameters shown in Table 3.2 show that a 30 minute etch results in a 47 μm deep trench, Fig 3-1, which is more than the design undercut depth, 15 μm.

The isotropic etch also uses the STS etcher but with a recipe (sf6_2) that provides only a SF_6 flow. The isotropic etch is carefully monitored to avoid over-etching and under-etching. Over-etching will remove the silicon supporting the ends of the sensing elements. Under-etching

50

Table 3.2: Anisotropic etch recipe (MIT 69) parameters.

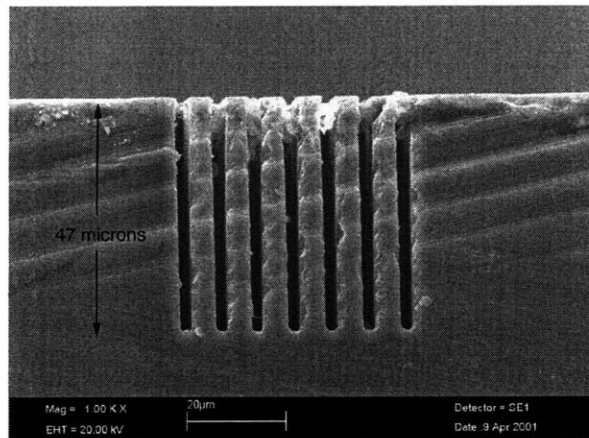|	SF$_6$	C$_4$F$_8$
Flowrate (sccm)	105	40
	Passivation cycle	Etch cycle
rf forward power (Coil) (W)	600	750
Load position (degree)		50
Tune position (degree)		50
rf foward power (Platen) (W)	60	100
Load position (degree)		50
Tune position (degree)		50
Chamber process pressure (mT)		11
APC angle (degree)		65
Chamber peak-to-peak voltage (V)		70
Chamber bias voltage (V)		0

Figure 3-1: SEM picture of a sample used for the anisotropic etch characterization. The sample went through the following process: grown 1 micron of thermal oxide, anisotropic oxide etch for the etch holes, 30 minutes anisotropics silicon etch, and then die-sawing.
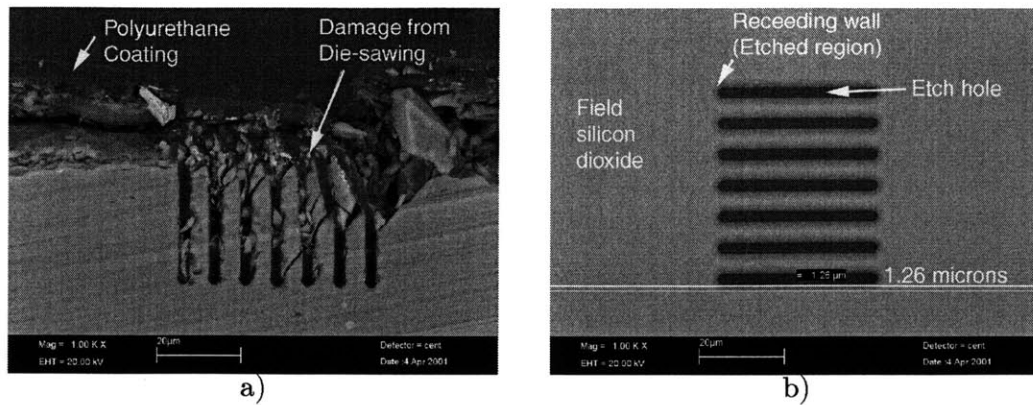
Figure 3-2: SEM pictures of samples used in the isotropic etch characterization. The samples were from a silicon wafer with 1.0 micron of thermal oxide. The etch holes were anisotropically etched into the thermal oxide, the silicon was then etched anisotropically for 22 min 38 sec, and finally it was isotropically etched for 5 minutes. The black slots are the etch holes, the dark gray rings are oxide with no silicon directly underneath, and the field (light gray) is oxide. a) Crossing sectional view. The sample was cut with a 25 micron die-saw blade. The top layer is a polyurethane coating used to protect the etch features. However, later samples showed that the polyurethane coating is not effective in preserving the feature details. b) Top view of a different sample.

will leave silicon underneath the sensing element, which reduces thermal isolation between the sensor and the silicon substrate. The isotropic etch characterization wafers were prepared using the same process as described in the previous paragraph. Subsequently, the whole wafer was anisotropically etched and then different wafer sections were isotropically etched for different times. Samples that were anisotropically etched for 30 minutes and then isotropically etched for various time did not provide satisfactory results. A cross-sectional view of the trench profile, Fig 3-2a, shows only the material near the wafer surface was etched. The sample shown was isotropically etched for 5 minutes and the silicon walls receded by 1.3 microns.

It is hypothesized that the passivation layer remaining from the previous anisotropic etch interfered with the isotropic etch. This was investigated by adjusting the anisotropic etching time to coincide with the ending of an etch cycle, 22 minutes 38 seconds. A second consideration in adjusting the etching time was to reduce the machine usage time because the STS is a heavily used machine in MTL. Isotropic etching results following a 22 minutes 38 seconds anisotropic etch, Fig 3-3, show a improved trench profile. The silicon walls directly underneath the oxide layer receded by about 2 μm and 6 μm after being isotropically etched for 5 and 10 minutes,
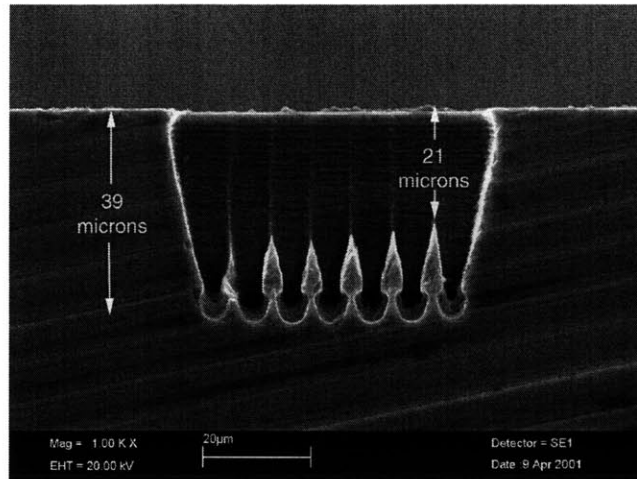
Figure 3-3: SEM picture of the cross-sectional view of a sample used for the isotropic etch characterization. This sample went through the following process: grown 1 micron of thermal oxide, anisotropic oxide etch for the etch holes, 22 minutes 38 seconds of anisotropic silicon etch, 8.5 minutes of isotropic silicon etch, and die-sawing. The white glow along the surface is due to charging in the SEM.

respectively, Fig 3-4.

However, the silicon substrate's surface at the undercut comprises of peaks and valleys, Fig 3-5. The isotropic etch etches the silicon at the top of the trench faster than the silicon at the bottom of the trench. The distance between the silicon substrate and the plane of the sensing element was measured by focusing at the two planes and measuring the height difference. The measurements show the distance ranges from 25 μm (from the peak of the silicon substrate's surface to the sensing element's plane) to 50 μm (from the valley of the silicon substrate's surface to the sensing element's plane).

3.2.2 Shadow Mask Metallization Process

Contact pad metallization provides ohmic contact, which reduces contact resistance. A platinum thin-film with a titanium adhesion layer were chosen because these metals can withstand high temperature, which is required for the temperature characterization experiment. The metallization process is complicated by the deep etch features and MTL's equipment cross-contamination prevention policies. MTL does not allow titanium into their deep etcher, STS etcher, to prevent
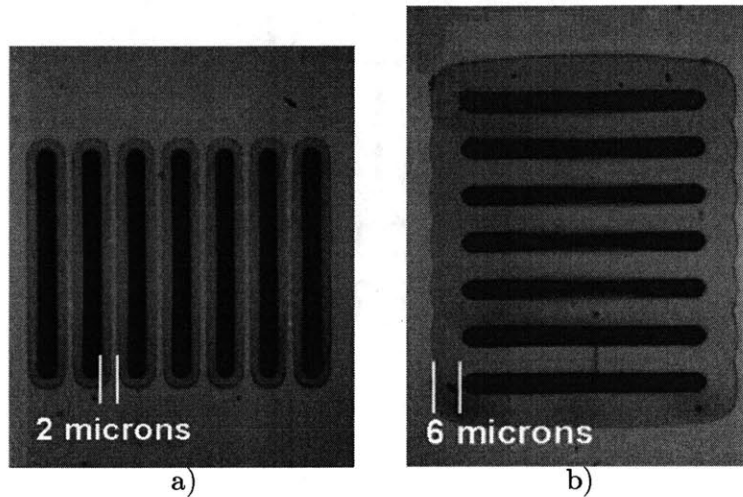
Figure 3-4: Optical microscope photographs of samples used in the isotropic etch characterization. Photographs show the samples' surface. Samples were from a silicon wafer with 1.0 micron of thermal oxide. The etch holes were anisotropically etched into the thermal oxide and then the silicon was etched anisotropically for 22 min 38 sec. a) Isotropically etched using a STS etcher for 5 minutes. b) Isotropically etched for 10 minutes.
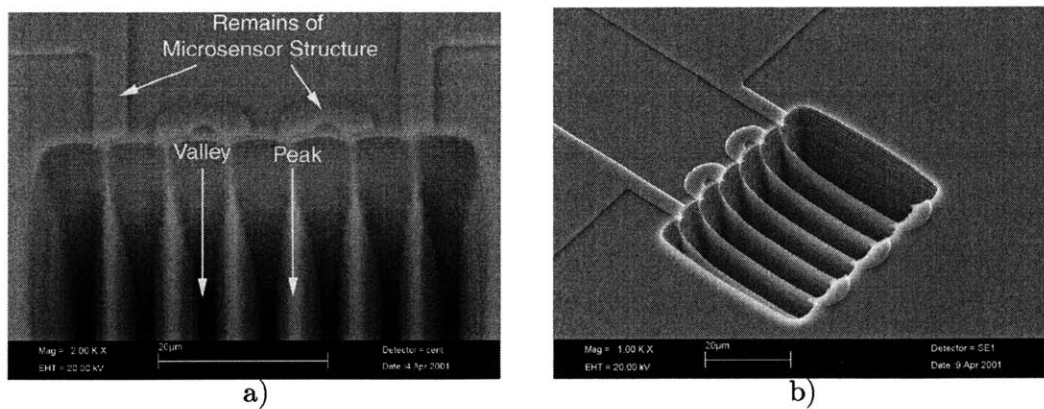
Figure 3-5: SEM picture of a sample where the sensor did not survive the fabrication process. The etch hole pattern misalignment caused the polysilicon to be etched during the undercut etching. The pictures show the surface profile of the undercut.
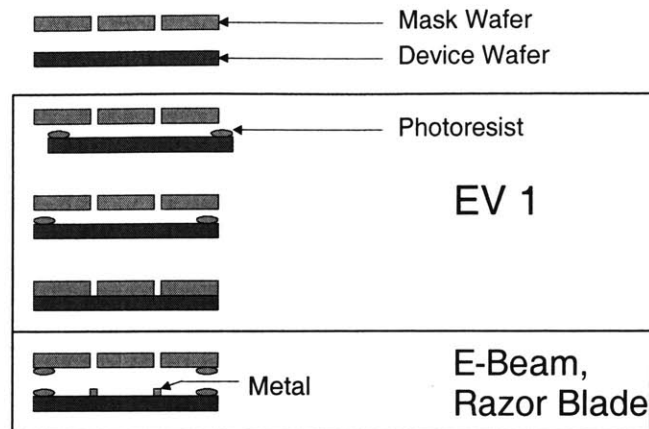
Figure 3-6: Shadow mask process. Very small amounts of thick photoresist is applied to the edges of the device wafers. The wafers are aligned using an Electronic Vision (EV1) tool. The pair of wafers are then placed on a 120 C hotplate for five minutes to harden the photoresist. Subsequently, metal is deposited using an e-beam deposition tool. The wafers are separated using a razor blade.

cross-contamination. Therefore, a simple metal deposition and etching process has to be done after the deep etching. However, a process for coating a wafer that has deep etches with photoresist requires an the equipment that is not available in MTL. Thus, a simple metal deposition and etching process cannot be incorporated into the sensor's fabrication process flow. A lift-off process would also require photoresist coating after the deep etches.

Consequently, a shadow mask process was used for metallization. A shadow mask process uses a masking wafer with thru-wafer holes at locations where deposition is desired to selectively deposit metal. The mask wafer is aligned to the device wafer and then the two wafers are held together. The pair of wafers is then placed in an e-beam deposition tool for metal deposition. An e-beam deposition tool is a line-of-sight deposition tool so only the areas of the device wafers that are exposed via the mask wafer's thru-wafer holes are deposited with metal.

The main challenges in a shadow mask process are aligning the wafers and holding them together. The large contact pads, 2.5 mm x 2.5 mm, relaxes the required alignment accuracy. The shadow mask process developed uses an Electronic Vision tool, which is an aligning and photoresist exposure tool, to align the wafers and photoresist to hold them together, Fig 3-6.

Chapter 4

Experiment Setup

The sensor fabricated is a polysilicon device whose resistance changes with temperature. Using this sensor requires knowing its temperature coefficient of resistivity (TCR), how the TCR changes under the conditions in the microengine, and how the resistance changes with time when it is subjected to a change in heat transfer conditions. This information can be obtained from temperature characterization and dynamic characterization experiments.

This chapter describes the temperature characterization and dynamic characterization experiment setups and the device packaging for the experiments. In the temperature characterization, a furnace was used to test the sensor's resistance vs. temperature behavior, behavior during thermal cycling, and behavior during annealing. In the dynamic characterization, a shock tube was used to excite the sensor with a step input in heat transfer conditions. The test was used to measure the sensor's time constant. In addition, flow parameters affecting the sensor's response was identified from the numerical model and verified with the shock tube.

4.1 Temperature Characterization

The temperature characterization experiment was used to measure the sensor's resistance during thermal cycling and annealing. To accomplish this, the experimental setup requires a furnace capable of going up to at least ~700°C, a temperature control system, a temperature measurement system, a resistance measurement system, and a packaging scheme capable of withstanding the high temperatures. This section describes these components except for the

packaging, which will be described in the Packaging section at the end of this chapter.

A schematic of the setup is shown in Fig 4-1. A die with two sensors was epoxied to a die-mount fixture, which was then mounted to a handle fixture (refer to the Packaging section for the fixtures' detail description). The fixture setup was then inserted into a 2.54 cm (1") quartz tube, which was in the furnace, such that the die was approximately at the tube's center. A 40 $\frac{mL}{min}$ nitrogen flow entered the quartz tube during characterization to reduce oxidization effects.

The temperature was measured with a 20 mil type K thermocouple that was epoxied using ceramic epoxy to the fixture about 2.5 cm away from the sensor. The thermocouple was used to approximate the sensor's temperature; thus, temperature variation along the quartz tube was measured to assess uncertainty. A measurement of the air temperature along the quartz tube's length show that the temperature varied by less than 1°C over the quartz tube's center 5 cm[30]. Since ceramic is a better thermal conductor than air, the temperature profile along the fixture will be more uniform than in air and the sensor's temperature can be approximated within 1°C of the temperature measured with the thermocouple. Temperature difference along the 5 cm that is caused by convection is negligible because convection heat transfer is approximately uniform along the 5 cm. Convection heat transfer is proportional to the temperature difference between the surface temperature and gas temperature and it is approximately constant along the 5 cm. The thermocouple was connected to a temperature controller and display.

The sensor's resistance was measured either by connecting it in series with an ohm-meter, Fig 4-1a, or by connecting it in series with a constant current source and in parallel with a volt-meter, Fig 4-1b. The former method is valid if the sensor has a linear I-V behavior because an ohm-meter is designed to measure devices with linear I-V characteristics. The latter method is used to demonstrate that the sensor's I-V behavior is linear and validates the former method. Results from both methods will be discussed in the Results and Discussion chapter.

4.2 Dynamic Characterization

For a particular sensor design, the sensor's signal magnitude and, to a lesser degree, response time depend on the flow conditions that it experiences. A shock tube was used to subject the
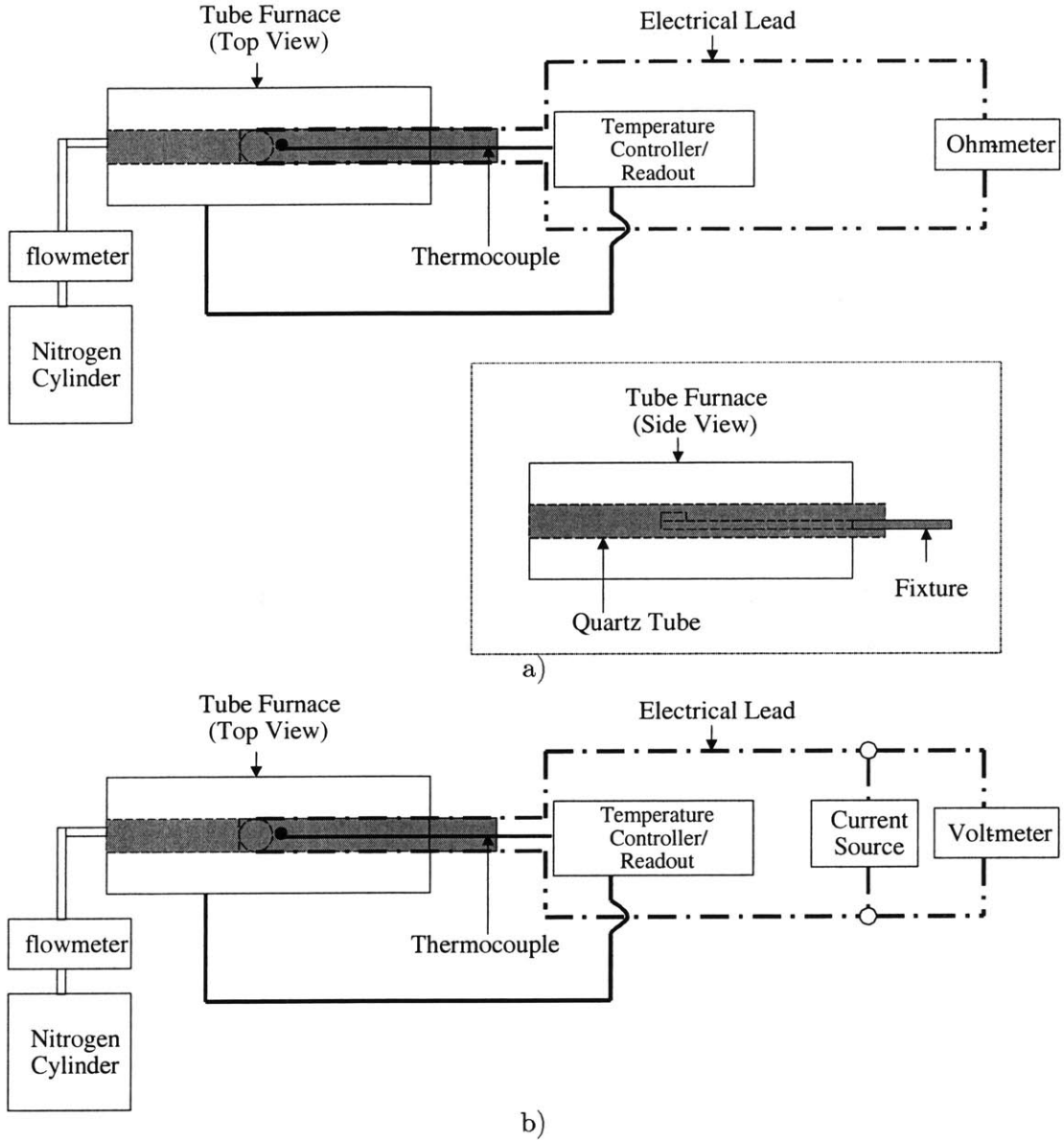
Figure 4-1: Schematic of test setup used for resistance vs. temperature characterization. a) The sensor's resistance is measured using an ohm-meter. b) The sensor is supplied with a constant current and output is measured with a voltmeter.

sensor to different flow conditions and to test its dynamic response. The sensor is subjected to different heat transfer conditions, such as gas velocity and temperature, to observe the importance of each on its performance.

A shock tube is a device that produces a shock wave. A shock tube is separated into two regions by a diaphragm. A pressure difference across the diaphragm causes it to rupture, which produces a shock wave. The pressure difference is obtained by pressurizing one region, the driver section, and evacuating the other region, the driven section, or just by pressurizing the driver section. Different shock speeds and heat transfer conditions are obtained by varying the initial pressure ratio, the driver gas, and/or the driven gas. A detailed discussion of shock tube theory can be found in references [31][32].

The shock tube used in this experiment is a 5.08 cm (2") diameter 5.3 m long (a 2.8 m driven section and a 2.4 m driver section) steel tube with instrumentation ports and gas inlets/outlets, Fig 4-2. Clear Polyvinyl Chloride (PVC) film was used as the diaphragm. A thicker diaphragm for experiments with higher initial pressure ratio was obtained with multiple layers of the PVC film. Atmospheric air was used as the driven gas and air from a gas cylinder containing compressed air was used as the driver gas.

A 250 psi Kulite pressure transducer was placed at instrumentation port 1 to measure the shock speed and the pressure profile. The shock speed was calculated from the time difference between the pressure transducer's and the sensor's initial excitation and the distance between them. The measured pressure profile and the shock speed were compared to the expected values predicted from analytical solutions with the initial pressure ratio. The pressure transducer was connected to a signal conditioner/amplifier, whose output was displayed on and recorded by a digital oscilloscope.

The shock tube fixture with the sensor was placed in instrumentation port 2. The sensor was connected to a circuit designed by Stephen D. Umans of MIT Electrical Engineering and Computer Science Department, Fig 4-3, that conditioned and amplified the signal. With this circuit, a constant voltage is applied across the sensor and a resistance change causes a current change, which can be approximated by Eq 4.1

$$\Delta i \approx -I_0 \left(\frac{\Delta R}{R_S} \right) \tag{4.1}$$

Figure 4-2: Schematic of shock tube experiment setup.

61
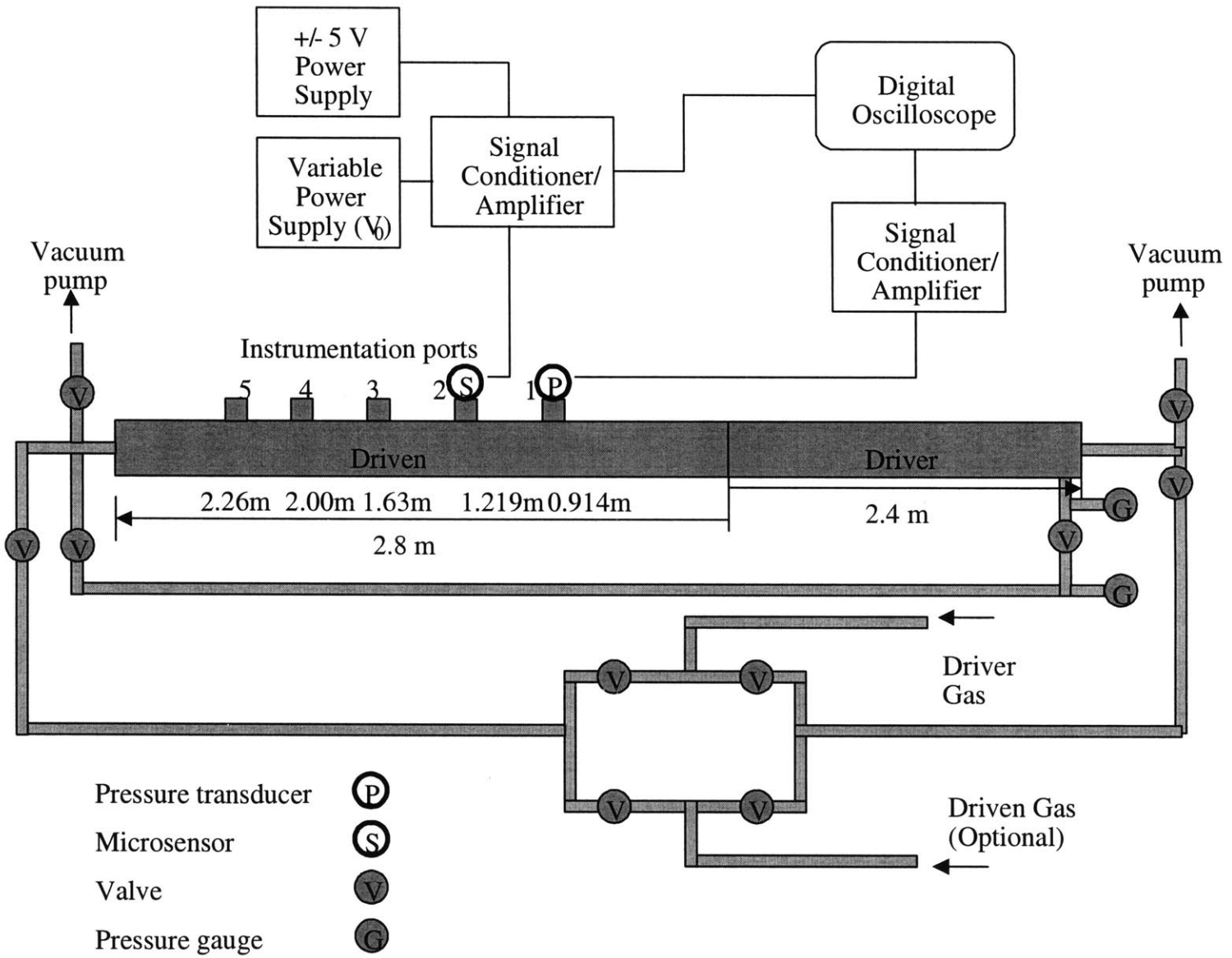
where Δi is the current change, I_0 is the nominal current, ΔR is the resistance change, and R_S is the sensor's resistance. The expected $\frac{\Delta R}{R_S}$ was less than 0.2 %, Fig 4-4, thus, the current should fluctuate by less than 0.2 %. The corresponding resistance change error because the current is not constant is expected to be less than 1 %, Fig 4-4b. The flow conditions used in the numerical model to calculate the expected signal were based on the temperature and velocity of the gas behind a shock wave. The wave conditions used in the analysis of Fig 4-4 were the initial pressure ratio is 4, the driven section initial pressure is 1 atm, and the driven gas and the driver gas are air. The flow conditions can be calculated with the initial pressure ratio and the gas properties using Eq 4.2[32]

$$u = a_1 \left(\frac{p_2}{p_1} - 1 \right) \sqrt{\frac{2/\gamma_1}{(\gamma_1 + 1)p_2/p_1 + (\gamma_1 - 1)}} \tag{4.2}$$

$$u = \frac{2a_4}{\gamma_4 - 1} \left[1 - \left(\frac{p_3}{p_4} \right)^{(\gamma_4 - 1)/2\gamma_4} \right]$$

$$\frac{p_4}{p_1} = \frac{p_2}{p_1} \left[1 - \frac{(\gamma_4 - 1)(a_1/a_4)(p_2/p_1 - 1)}{\sqrt{2\gamma_1}\sqrt{2\gamma_1 + (\gamma_1 + 1)(p_2/p_1 - 1)}} \right]^{-2\gamma_4/(\gamma_4 - 1)}$$

$$\frac{T_3}{T_4} = \left(\frac{p_3}{p_4} \right)^{(\gamma_4 - 1)/\gamma_4}$$

$$\frac{T_2}{T_1} = \frac{1 + \frac{\gamma_1 - 1}{\gamma_1 + 1}\frac{p_2}{p_1}}{1 + \frac{\gamma_1 - 1}{\gamma_1 + 1}\frac{p_1}{p_2}}$$

where u is velocity, T is temperature, a is speed of sound, γ is $\frac{c_p}{c_v}$, and p is pressure. The subscripts 1, 2, 3, and 4 denotes the part of the driven section that has not experienced the shock wave, between the shock wave and the contact surface, between the contact surface and the expansion front, and the pressurized driver section that has not been affected by the expansion front, respectively. These initial conditions produce a shock speed of 462 $\frac{m}{\sec}$ and gas velocity and temperature behind the shock wave of 175 $\frac{m}{\sec}$ and 365 K, respectively. The heat transfer coefficient was calculated based on a fully-developed internal pipe flow correlation, Eq 4.3[33]

$$Nu_D = 0.027(\mathrm{Re})^{4/5}(\mathrm{Pr})^{1/3}\left(\frac{\mu}{\mu_s}\right)^{0.14} \tag{4.3}$$

$$h = \frac{Nu * k}{D}$$

$$\mathrm{Re} = \frac{\rho u D}{\mu}$$

where Nu is the Nusselt number, Re is the Reynolds number, Pr is the Prandtl number, μ is the dynamic viscosity at the film temperature, μ_S is the dynamic viscosity at the wall temperature, k is the air conductivity, D is the pipe diameter, ρ is the air density. Using $\rho = 1\ \frac{kg}{m^3}$, $\mu = 2.7\mathrm{x}10^{-5}\frac{m^2}{\mathrm{sec}}$, $\mu_S = 1.8\mathrm{x}10^{-5}\frac{m^2}{\mathrm{sec}}$, Pr = 0.7, $k = 400\frac{W}{m\cdot K}$, and $D = 5.08$ cm (2"), the heat transfer coefficient is approximately 500 $\frac{W}{m^2 K}$. Subsequently, the heat transfer condition used in the numerical model to generate the expected signals result are step changes of flow temperature from 300 K to 365 K and a heat transfer coefficient from 0 to 500 $\frac{W}{m^2 K}$. Later comparison with measurements will show that the heat transfer coefficient is underestimated by over an order of magnitude using this procedure. The discrepancy is due to initial formation of the boundary layer and will be discussed in more detail in the Results and Discussion chapter.

The current's DC component is filtered out and the current change is detected and converted into a voltage output by the circuit. A voltage V_0 is supplied to the circuit to set the current driving the sensor. The current is proportional V_{I0}, where 1 V = 1 mA. The signal from the circuit, V_{OUT}, is related to the resistance change according to Eq 4.4

$$V_{OUT} = 10^5 I_0 \left(\frac{\Delta R}{R_S}\right) \tag{4.4}$$

The circuit was designed to have sufficient gain to amplify the sensor's signal to measurable levels and a bandwidth capable of faithfully reproducing the sensor's transient response. The expected sensor's time constant was approximately 25 μsec, thus, the circuit must have a time constant smaller than 25 μsec. To the first-order, the following transfer function, Tf, can be used to determine the circuit's bandwidth needed to accurately replicate the sensor's transient signal, Eq 4.5
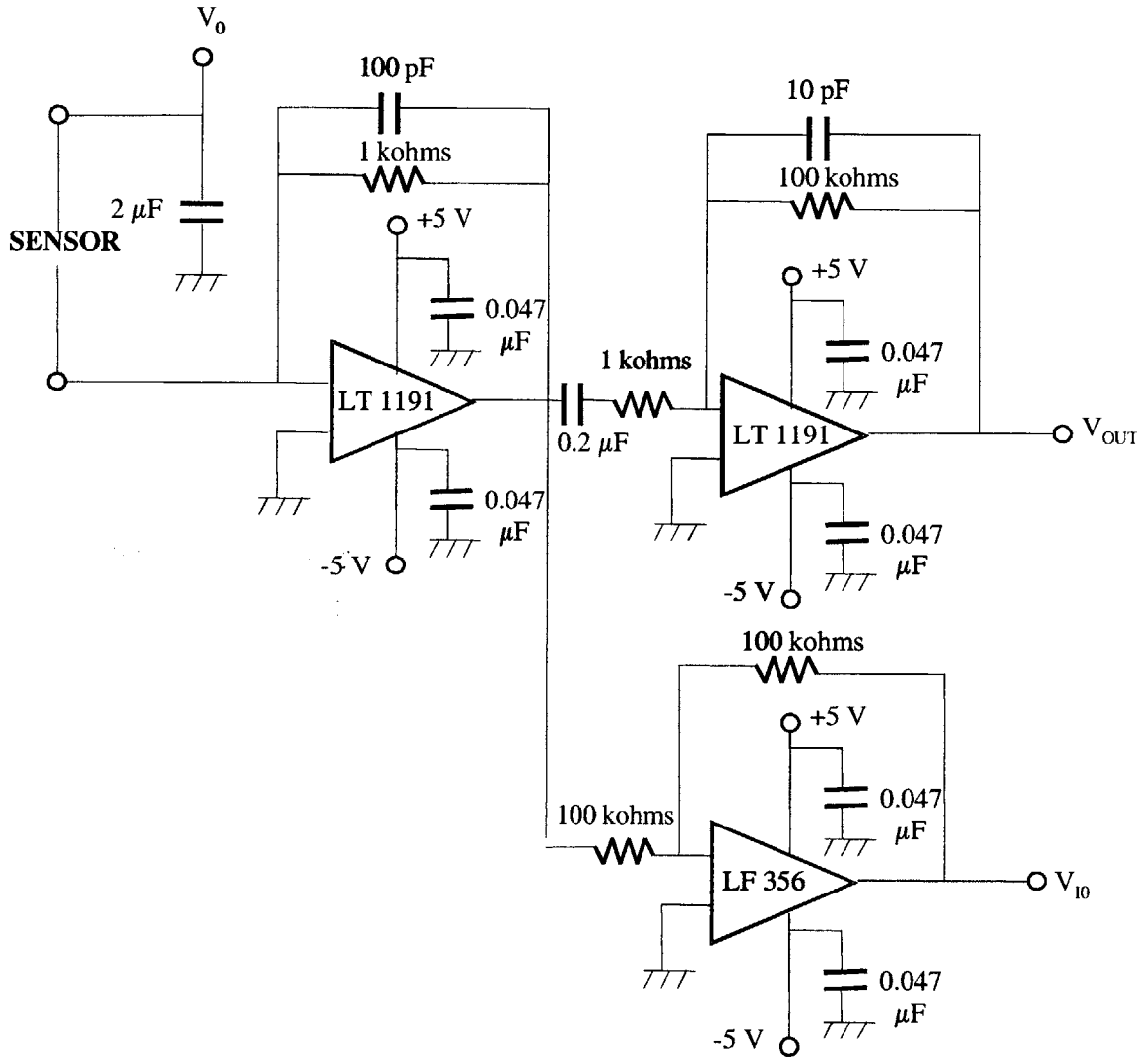
Figure 4-3: Schematic of the sensor's signal conditioner/amplifier circuit. The circuit was designed by Stephen D. Umans of MIT EECS deparment.
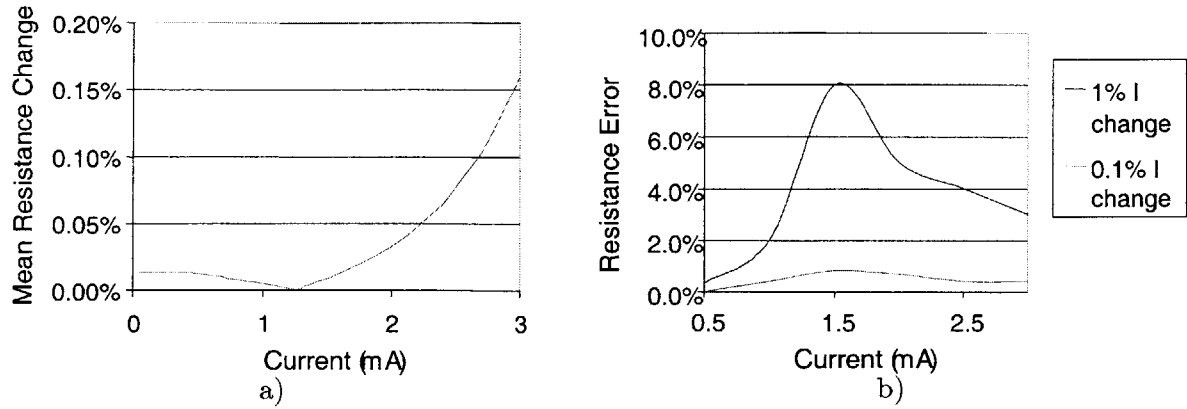
Figure 4-4: a) The expected resistance change from the shock tube experiments. b) The error from current fluctuation. The results are from the numerical model with the following conditions: sensor thickness = 0.6 microns, wall temperature= 300 K, TCR = 0.0008, room temperature resistance = 10 kohms, flow temperature = 375 K, heat transfer coefficient induced by the gas behind the shock wave = 500 W/m(square) K.

$$Tf = \frac{1}{1 + as} \tag{4.5}$$

This transfer function models an op-amp with a gain of 1. The pole, a, affects the similarity between the transient behavior of the op-amp's output and that of the op-amp's input, which will be the sensor's signal. The output from this transfer function for various a with a typical sensor response, the numerical model showed that the transient response for different heat transfer conditions were similar, was calculated using MatLab. The results, Fig 4-5, show that a should be less than $1x10^{-6}$. The transfer function of the circuit (calculated by S. Umans) has poles at $2x10^{-4}$, $1x10^{-6}$, and $1x10^{-7}$, as shown in Eq 4.6

$$\left[\frac{10^3}{1 + 10^{-7}s}\right] \left[\frac{-0.02s}{(1 + 2 \times 10^{-4}s)(1 + 10^{-6}s)}\right] \tag{4.6}$$

The circuit was designed to have a constant output signal between 796 Hz $((5x10^3)/2\pi)$ and 160 kHz $(10^6/2\pi)$ and filter signals higher than 1.6 MHz $(10^7/2\pi)$. The output from the sensor's signal conditioner/amplifier was also displayed on and recorded by a digital oscilloscope.
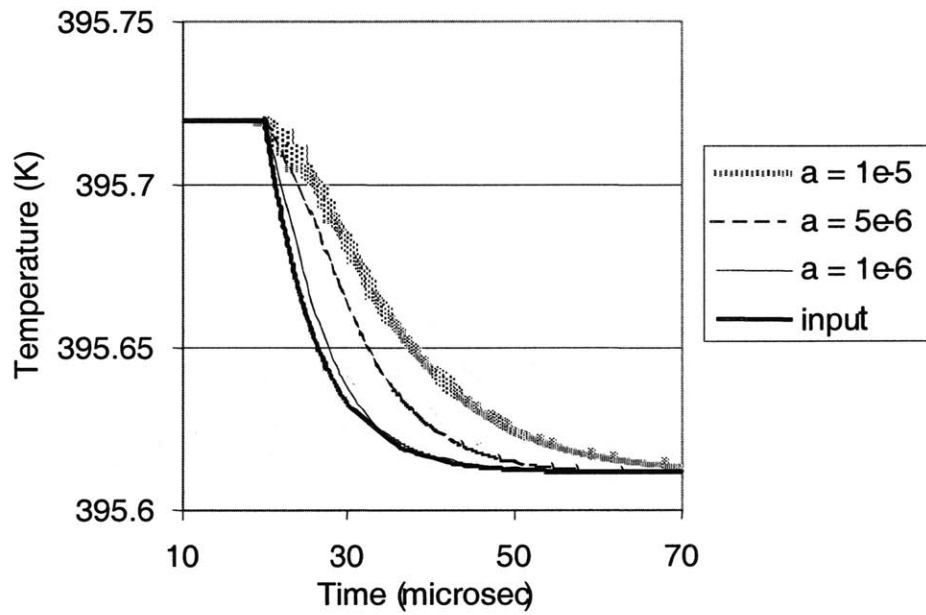
Figure 4-5: Modelled outputs using the transfer function $1/(1+as)$ for various values of a, which correspond an op-amps bandwidth. The output for a = 1e-6 reproduces the input signal better than the larger values for a.

4.3 Packaging

The sensor needed to be packaged for testing in the furnace and the shock tube. The packaging design must satisfy the geometric constraints of both the furnace's quartz tube and the shock tube's instrumentation port and survive up to 700°C in the furnace. A three-fixture design (a die-mount fixture, a handle fixture for the furnace, and an instrumentation plug fixture for the shock tube) and wire bonding were used to package the sensor. The three fixtures will be first discussed followed by a description of the wire bonding method used for electrical connection.

4.3.1 Fixtures

The die-mount fixture is a ceramic, Macor, cylinder with a slot on one surface, Fig 4-6a. The die and two pieces of platinum foil were epoxied onto the die-mount fixture's using Resbond 940 Fast Set ceramic epoxy. Subsequently, the platinum foils were connected to the contact pads by wire bonding platinum wires (for high temperature) or gold wires (for low temperature). The ceramic and platinum foil are capable of surviving up to 800°C and 1700°C, respectively, and thus, are suitable for use in both the furnace and the shock tube.

The handle fixture is a 0.15875 cm ($\frac{1}{16}$") thick ceramic, Macor, sheet machined to 30.48 cm x 1.5875 cm (12" x $\frac{5}{8}$"), Fig 4-6b. After the die and platinum foils were epoxied to the die-mount fixture, the die-mount fixture and two pieces of platinum foil were epoxied at opposite ends of the handle fixture using the ceramic epoxy. The platinum foils on the die-mount fixture were connected to the platinum foil on the opposite end of the handle fixture by spot welding 0.25 mm bare platinum wires. Copper wires, soldered to the platinum foils on the end that is outside of the furnace, were connected to electronic instruments, such as a current source, a volt-meter, and/or an ohm-meter.

The instrumentation plug fixture was made from a 0.635 cm x 5.08 cm x 5.08 cm ($\frac{1}{4}$" x 2" x 2") aluminum base, a 0.635 cm ($\frac{5}{8}$") diameter ceramic piece, and the die-mount fixture. The aluminum base has 4 through holes for screws to clamp it to the shock tube's instrumentation port and 2 0.5 mm through holes for the lead wires. Also, it has an o-ring groove on the side in contact with the shock tube. The cylindrical ceramic piece is epoxied to the center of the aluminum base piece using a 15-minute epoxy. The die-mount fixture is then epoxied to
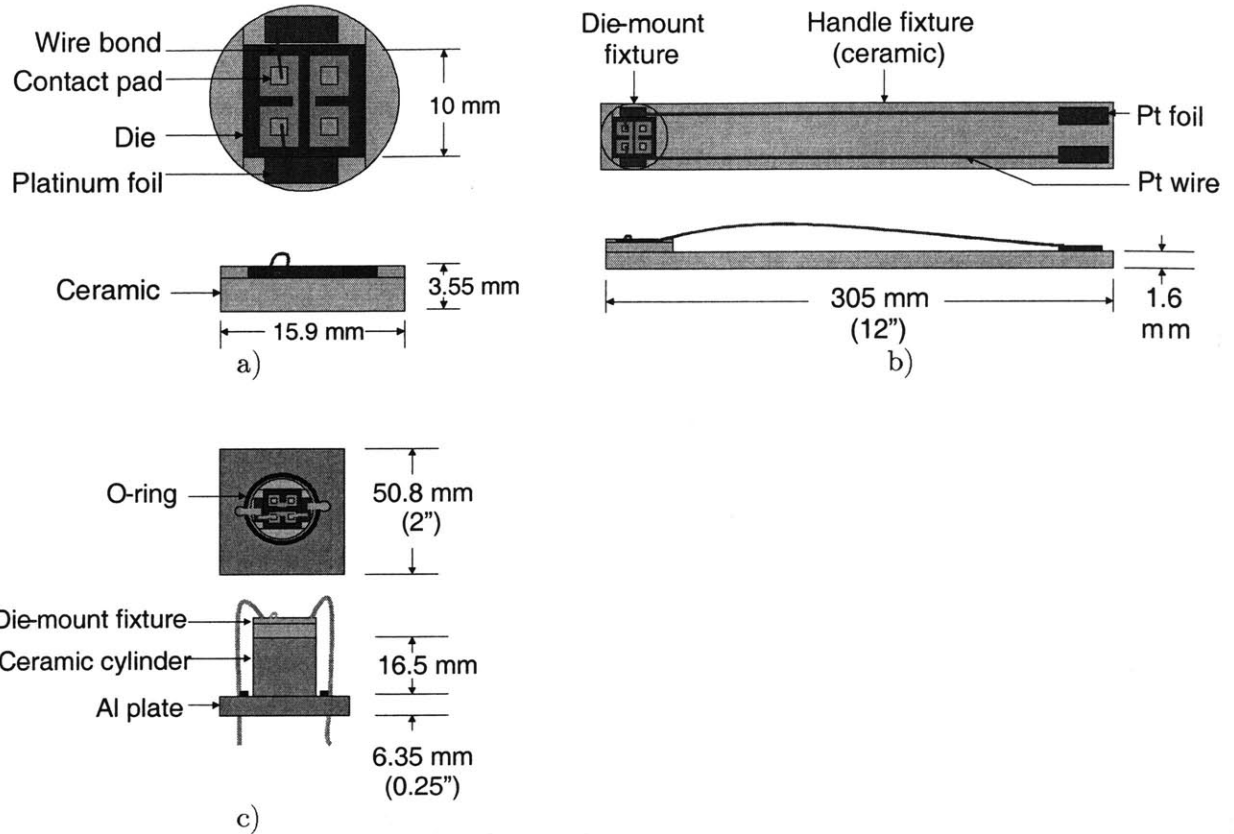
Figure 4-6: Fixture designs. Not to scale. a) The ceramic fixture used to mount the die. The die and two pieces of platinum foil are epoxied to the ceramic fixture. b) The ceramic handle fixture used for the furnace. The die-mount fixture and two pieces of platinum foil are epoxied to opposite ends. c) The shock tube instrumentation port fixture. The die-mount fixture is epoxied to the shock tube instrumentation port fixture and wires are soldered to the platinum foils on the die-mount fixture.

the cylindrical ceramic piece using a 15-minute epoxy. Since the fixture and the die will not experience high temperature in the shock tube, gold wires can be used to wire bond the contact pads to the platinum foils for samples that have not been wire-bonded. Teflon covered wires are soldered to the platinum foil and fed through the 0.508 cm ($\frac{1}{5}$") holes, which are subsequently potted with 15-minute epoxy.

4.3.2 Wire Bonding

After the die and platinum foils were epoxied to the die-mount fixture, the device's contact pads were connected to the platinum foils by wire bonding platinum wires for the furnace experiment or gold wires for the shock tube experiment. Platinum wires were used for the

furnace experiment because of the high temperature. However, the platinum wires were bonded using a Kulicke and Soffa Industries Model 4123 wedge bonder and wedge bonding platinum was difficult, which resulted in low yields of devices successfully packaged for the furnace testing. In contrast, the gold wires were bonded using a Kulicke and Soffa Industries Model 4124 ball bonder and had better yield. However, gold wires can only be used for the low temperature shock tube experiment.

Chapter 5

Results and Discussion

This chapter presents and discusses the furnace experiment and shock tube experiment results. The furnace experiment was used to characterized the sensor's resistance vs. temperature behavior, effects of thermal cycles on the temperature coefficient of resistance, and resistance stability during annealing. The shock tube experiment was used to measure the sensor's time constant and to compare the measured responses to the predicted responses.. The feasibility of incorporating the sensor into the microengine will be discussed using the test results.

5.1 Furnace Experiment

This section describes and discusses the temperature characterization results: resistance vs. temperature behavior, effects of thermal cycles on the resistance vs. temperature behavior, and resistance stability during annealing at 500°C. In the thermal cycles, the temperature cycled from room temperature to 700°C. The purpose of this experiment was to observe changes in the TCR and resistance drift caused by thermal cycles. At the end of the thermal cycles, the sensor was annealed at 500°C, which is about the wall temperature where the sensor would be located in the microengine, to observe any resistance drift caused by the high temperature. Resistance drift is a function of the temperature and annealing time. Even though the sensor experienced a maximum temperature of 700°C in the experiment, the annealing time at 700°C is several minutes and produces negligible resistance drift compared to annealing at 500°C for over an hour.

The sensor's resistance was measured by either an ohm-meter or calculated from I-V measurements. Using an ohm-meter to measure resistance is more straightforward and provides a more precise resistance measurement than calculating resistance from I-V measurements, provided that the device has a linear I-V characteristic. The uncertainty in the resistance calculated from the I-V measurements is larger than the resistance measured from an ohm-meter because of the relatively large uncertainty in the current reading for the I-V measurement, as described in the Appendix: Uncertainty Analysis. The relatively large uncertainty in the current readings can be eliminated by using an higher precision ammeter, which was not available at the time of the experiments. The I-V measurements will confirm the sensor's linear I-V characteristic and validate the ohm-meter resistance measurements.

The sensors used for the temperature characterization experiments have no undercut etch, i.e. steps 13-17 in the fabrication process were skipped. These steps were skipped to increase the yield and produced more devices to test for the temperature characterization experiment. The yields were low (~15%) because aligning the second mask to get the oxide mask trenches between the sensing elements required ± 0.5 μm alignment accuracy. Future designs should increase the spacing between sensing elements to increase the alignment tolerance.

The structural difference between the samples used for the temperature characterization and the design, undercut vs. no undercut, may introduce some errors in the resistance vs. temperature measurements. Temperature changes the stress in the polysilicon film and the structural difference may cause the samples with no undercut to have different stresses than those with an undercut. Since polysilicon has piezoresistive characteristics, these differences will result in errors in the resistance measurement. An estimate of the $\frac{\Delta R}{R_o}$ caused by piezoresistive effects will be used to validate the resistance measurements obtained from the samples with no undercut.

Using a general theory for elastic interaction in a composite plate composed of layers with different but isotropic properties, the stress caused by a temperature change for a thin film on a thick substrate can be approximated by Eq 5.1[34]

$$\sigma_i = \frac{E_i}{1 - \nu_i} \left(\alpha_s - \alpha_i \right) \triangle T \qquad (5.1)$$

where σ_i in the stress in the ith film, E_i, ν_i, and α_i are the Young's modulus, Poisson's ratio,

and temperature coefficient of expansion (TCE) of the material in the ith film, and $\triangle T$ is the temperature change. This equation assumes that the substrate's thickness is much larger than the combined thicknesses of all the films and the interaction between films is a minor effect. According to this equation, the thin film conforms to the substrate and the thin film's strain is the product of the TCE difference and the temperature change, Eq 5.2

$$\varepsilon_i = (\alpha_s - \alpha_i)\,\triangle T \tag{5.2}$$

where ε_i is the strain in the ith film. The strain is related to the $\frac{\triangle R}{R_o}$ by a gauge factor (G), Eq 5.3[35]

$$\frac{\triangle R}{R_o} = G\varepsilon \tag{5.3}$$

A gauge factor of approximately 25 was measured by Obermeier for 0.5 μm thick polysilicon ion implanted with approximately $5\mathrm{x}10^{15}$ cm^{-2} of boron and annealed at 950°C for 30 minutes[35]. Using TCE's of $2.9\mathrm{x}10^{-6}$ K^{-1}and $4.3\mathrm{x}10^{-6}$ K^{-1}for polysilicon and single crystal silicon[36][20], respectively, and $\triangle T$ of 600 K $\frac{\triangle R}{R_o}$ is approximately 2.5%. This is much smaller than the resistance change measured, approximately 60% resistance change over 600 K, which will be discussed later in this chapter. Thus, the resistance vs. temperature measurements for the samples with no undercut will be similar to those of samples with undercut because the $\frac{\triangle R}{R_o}$ caused by piezoresistive effects is over a magnitude less than that caused by the temperature change.

5.1.1   Room Temperature Resistivity

The sensors produced have room temperature resistances of approximately 9-10 kohms, which corresponds to a resistivity of 0.006 ohms-cm. This resistivity was higher than the expected resistivity, 0.002 ohms-cm, which was based on Jiang's polysilicon dopant concentration ($2\mathrm{x}10^{20}$ cm^{-3} of boron). Two variations contributed to this discrepancy: the ion implant dose and the activation anneal. A discussion of polysilicon's electrical properties will be introduced to explain this discrepancy.

Electrical properties of polysilicon are generally explained using a segregation model or a

grain boundary trapping model. Boron dopant has been shown to not segregate in polysilicon[37]. This discussion will therefore focus on a grain boundary trapping model, which was originally proposed by Kamins[38] and Rai-Choudhury and Hower[39] and, subsequently, quantitatively validated by Seto[40]. Polysilicon's resistivity has contributions from the Si-crystals, crystallites, and from the grain boundaries. Seto proposed a model that relates polysilicon's resistance to these two factors, Eq 5.4

$$R(T) = R_C\,(T)\,\frac{(l - l_g)}{l} + R_g(T)\frac{l_g}{l} \qquad (5.4)$$

where $R(T)$ is the polysilicon's resistance, R_C and R_g are the contributions from the silicon crystal grains and the grain boundaries, respectively, l is the silicon grain's length, l_g is the length of the depletion zone around the grain boundary. This model was later modified by Lu to better match resistivity results of polysilicon for grain size larger than 600 angstroms but still had both contributions[41]. At the grain boundaries, there are a large number of electron traps sites that fill as dopants are added. As these traps are filled by dopants and decrease to below approximately 10^{14} cm^{-3}, the resistivity contribution from the crystallites dominate and approaches that of a single-crystal silicon[42]. The crystallites properties becomes increasingly important at high dopant concentration because it dominates the polysilicon's resistivity. Thus, different grain sizes contributes to variation in resistivity of different polysilicon samples that have the same high dopant concentration[41].

Jiang used polysilicon, 0.5 μm thick, with a 0.002 ohms-cm resistivity with 2×10^{20} cm^{-3} dopant concentration from a boron ion implant dose of 1×10^{16} cm^{-2} at 80 keV. His device was annealed at 1100°C for 1 hour. In contrast, the device presented here was ion implanted with a 5×10^{15} cm^{-2} dose of boron at 80 keV, corresponding to a 8×10^{19} cm^{-3}, and annealed for a total at 900°C for 2 hours. These two factors, lower dopant concentration and lower anneal temperature, which causes slower grain growth, are thought to be the main cause of the expected and measured resistivity discrepancy. This explanation is consistent with experimental results from other researchers. For example, Kim's 0.4 μm thick polysilicon samples deposited at 600°C and have 1.5×10^{20} cm^{-3} and 7.5×10^{19} cm^{-3} of boron and annealed at 950°C for 30 minutes have resistivity of about 0.006 ohm-cm and 0.012 ohms-cm, respectively[43]. Even though the resistivity of Jiang's device, Kim's polysilicon sample, and the device presented

here cannot be directly compared because of different deposition temperature and inherent process condition variations between facilities, the difference in the annealing conditions can demonstrate an approximate trend between grain size and resistivity. Kim's polysilicon samples annealing temperature and time were lower than those of Jiang's devices; thus, the grain size of Kim's polysilicon samples were smaller and have a greater resistivity than those of Jiang's devices.

5.1.2 Thermal Cycles

Fig 5-1a shows the I-V characteristic at 700°C of a sensor that has no undercut etch. It shows a linear I-V characteristic at the lower currents and an increasing slope at larger current. The increasing slope at the larger currents is due to Joule heating, which increases the sensor's temperature and resistance. Fig 5-1b shows the resistance vs. temperature (from 22°C to 700°C) of the same device. Its TCR can be calculated from a the slope and y-intercept from a best-fit linear equation. Resistance and temperature are related by Eq 5.5

$$R = R_0(1 + \alpha \Delta T) \tag{5.5}$$

where R is the resistance at temperature T, R_0 is the resistance at some reference temperature, and α is the TCR. Its TCR was calculated by dividing the slope by the y-intercept, i.e. reference temperature is 0°C, and is 0.08 /°C.

Fig 5-2 shows the resistance vs. temperature behavior of two sensors for about two anneal cycles. These two sensors are from the same wafer. During the anneal cycles, the resistance was measured with either an ohm-meter or calculated from I-V measurements. Both methods were used to verify consistency in the resistance measurements. Device W14-B2 went from room temperature to 700°C, down to 300°C, up to 700°C, down to 300°C, up to 500°C, and was annealed at 500°C for 85 minutes. All of device W14-B2's resistance values were calculated from I-V measurement, thus the uncertainty is relatively large because of the relatively large current uncertainty, as discussed in Appendix: Uncertainty Analysis. Device W14-D4 went from room temperature to 700°C, down to 100°C, up to 700°C, down to 300°C, up to 500°C, and was annealed at 500°C for 60 minutes. All of device W14-D4's resistance values were measured with an ohm-meter except those for the first ramp down, which were calculated from
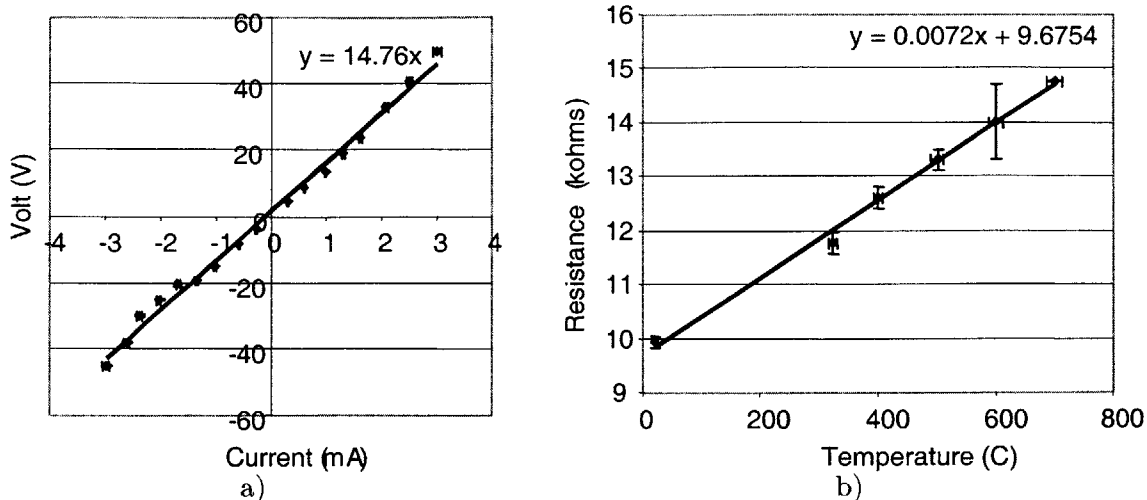
75

Figure 5-1: Furnace characterization results for device W14-C5. a) I-V behavior at 700 C. The nonlinear behavior at the higher current levels are due to Joule heating. b) Resistance vs. temperature behavior. A linear curve fit was used to calculate the TCR.

I-V measurements.

A linear equation was fitted using Excel for each step of the anneal cycles and the results are shown in Fig 5-3. The slope, y-intercept, and R^2 (coefficient of determination) were obtained from Excel's Regression Analysis Toolkit. The 95% uncertainty levels in Fig 5-3 were calculated using a Student-t distribution and the standard error calculated by Excel's Regression Analysis Toolkit. The linear curve fit produced equations that matched the data points well, as demonstrated by the R^2 values. The minimum R^2 value is 0.95, where the fit becomes better as R^2 approaches 1. The TCR for W14-B2 and W15-D4 range from 0.067 $\frac{\%}{K}$ to 0.11 $\frac{\%}{K}$ and 0.076 $\frac{\%}{K}$ to 0.10 $\frac{\%}{K}$, respectively. These values are about 50% of the expected TCR value. The reference resistance for W14-B2 and W14-D4 varied by less than 22% and 18%, respectively, during the anneal cycles.

The sensors produced have TCR in the range from approximately 0.7 $\frac{\%}{K}$ to 0.11 $\frac{\%}{K}$. The expected TCR was 0.2 $\frac{\%}{K}$, which was based on Jiang's polysilicon dopant concentration (2×10^{20} cm^{-3} of boron). This discrepancy can be explained from the process variations, similar to the room temperature resistivity discussed earlier. A discussion of the mechanism by which polysilicon's resistivity changes with temperature will be introduced to explain this discrepancy.

As described in Seto's model, the resistivity is determined mainly by the grain boundaries

16.5

15.5

14.5

Resistance (kohms)

13.5

12.5

11.5

0   200   400   600   800
Temperature (C)
a)

◆ 1 up
■ 1 down
△ 2 up
✳ 2 down
○ 3 up
● hold

17

16

15

14

Resistance (kohms)

13

12

11

10

9

0   200   400   600   800
Temperature (C)
b)

◆ 1 up
■ 1 down
△ 2 up
✳ 2 down
○ 3 up
● hold
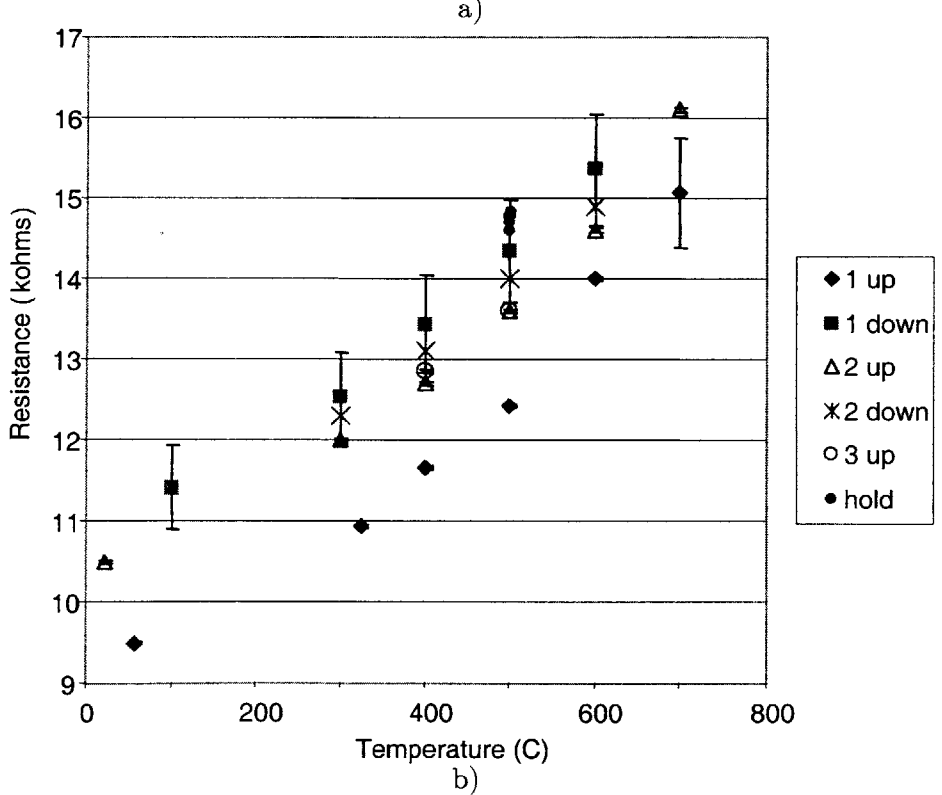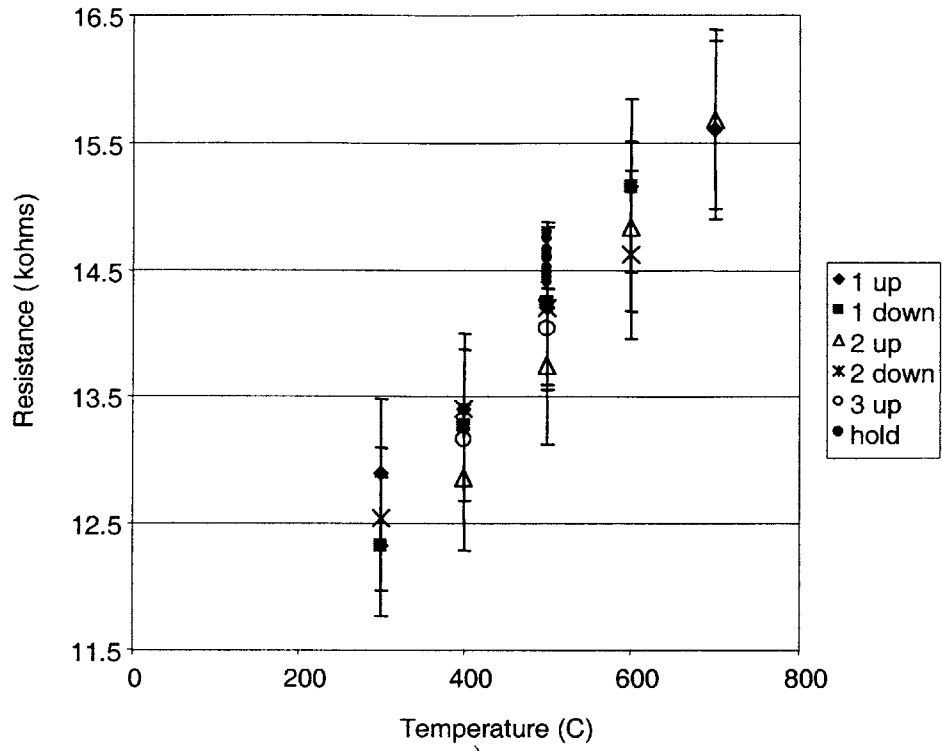
Figure 5-2: Furnace characterization results for two devices: W14-B2 and W14-D4. Both devices went through about two temperature cycles. Both devices were from the same wafer and were annealed with 40 mL/min of N2. a) W14-B2. b) W14-D4.
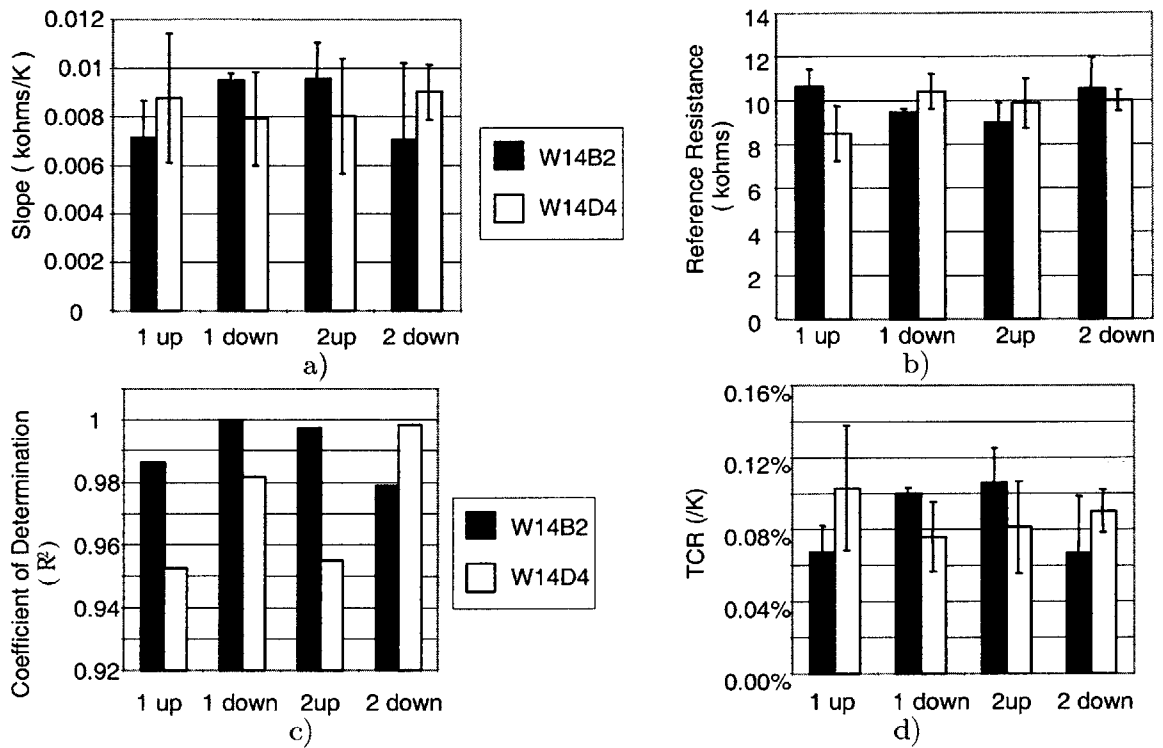
Figure 5-3: Analysis of the resistance vs. temperature measurements. Linear curve fits were used to obtained the slope and reference resistance. The coefficient of determineation was obtained from Exel's Regression AnalysisToolkit. The TCR was calculated using the slope and the reference temperature.
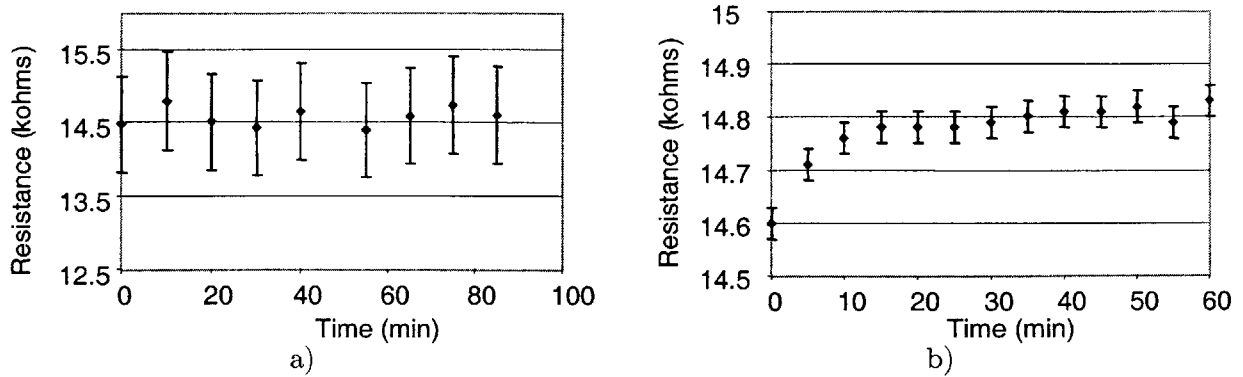
Figure 5-4: Resistance behavior of W14-B2 and W14-D4 while annealed at 500 C. The annealing was done after the 3rd temperature ramp up. a) W14-B2. b) W14-D4.

and crystallites. In the grain boundary, charges trapped there generate an electrostatic force causing a depletion zone. The depletion zone creates a potential barrier and impedes carrier mobility. Increasing temperature excites carriers and more charge are able to overcome this barrier. Thus, the resistivity decreases with increasing temperature when the grain boundaries' contribution dominate. In contrast, the resistivity increases with increasing temperature when the crystallites' contribution dominate. Increasing temperature increases the scattering of carrier; thus, the resistivity is increased[44]. Similar to the resistivity, the TCR also depends on the doping concentration and grain structure.

Obermeier has done a comprehensive study of boron dopant concentration affects on polysilicon's TCR[45]. Based on his sample, 0.5 μm polysilicon deposited by LPCVD followed by ion implantation and anneal at 950°C for 30 minutes, polysilicon with a $8x10^{20}$ cm^{-3} boron concentration had a TCR of approximately 0.01 $\frac{\%}{K}$. His value is within the TCR range calculated for the devices presented here.

5.1.3 Anneals- Resistance Drift

At the end of the anneal cycles, both devices were annealed for 60 or 85 minutes. Fig 5-4 show the annealing behavior for both devices. The resistance of W14-B2 and W14-D4 at 500°C varied by less than 3% and 2%, respectively, during the anneal.

Table 5.1: Flow conditions of the air behind the shock wave, which were calculated using the shock tube equations presented in the Experimental Setup Chapter. Air is the driver and driven gas.

Initial pressure ratio ($\frac{p_4}{p_1}$)	2	3.2	4
$\frac{C_p}{C_V}$	1.38	1.38	1.38
Initial temperature (K)	300	300	300
Shock velocity ($\frac{m}{s}$)	399	442	462
Air speed ($\frac{m}{s}$)	86	145	173
Air temperature (K)	330	351	363
Air pressure (atm)	1.4	1.75	1.93

5.2 Shock Tube Experiment

The shock tube experiment was used to measure the sensor's dynamic response to a step change in flow conditions. The response was used to estimate the sensor's time constant and verify the numerical model. The sensor was placed in the shock tube's instrumentation port #2, connected to the electronics, and supplied with a constant current. The current heated the sensor with the current level determining whether the air flow behind the shock wave heated or cooled it. The electronic was designed to condition and amplify the signal levels mentioned in the Experimental Chapter for a constant current between 1 mA to 2 mA. Therefore, 1.5 mA was used for the testing. The sensor was tested under the following conditions: 1.5 mA at initial pressure ratio of 4, 3.2, and 2 using air as the driven and driver gas. The calculated flow conditions for these pressure ratios are summarized in Table 5.1.

Results of these three test conditions are shown in Figs 5-5, 5-6, and 5-7 with their respective pressure profile, which was measured by a pressure transducer located at the shock tube instrumentation port #1. A comparison between the measured shock wave speed and the expected values, Table 5.2, shows that the predicted shock wave speeds agree within 4.7 % of the measured shock wave speeds. However, the discrepancy is 1.7 % larger than the shock wave speed calculation uncertainty (refer to Shock Speed Section in Appendix: Uncertainty Analysis) and may be due to the uncertainty of the air properties used in the calculations. The air properties used were for air but the gas used was compressed air that may have a different composition and, thus, properties. The predicted pressure behind the shock wave is within 7

Table 5.2: Comparison of the measured shock speed and pressure behind the shock wave to the predicted values obtained from the shock tube equations.

$\frac{p_4}{p_1}$	2	2	3.2	3.2	4	4	4
run #	1	2	1	2	1	2	3
Shock speed: Measured $(\frac{m}{s})$	388	384	434	437	447	441	449
Shock speed: Predicted $(\frac{m}{s})$	399	399	442	442	462	462	462
Pressure (2): Measured (atm)	1.40	1.40	1.70	1.70	1.88	1.88	1.80
Pressure (2): Predicted (atm)	1.4	1.4	1.75	1.75	1.93	1.93	1.93

% of the measured pressure and is within the uncertainty (refer to the Pressure Measurement Section in Appendix: Uncertainty Analysis).

The measured sensor response for the $\frac{p_4}{p_1} = 4$ condition is about 2 orders of magnitude greater than the expected response shown in Fig 4-4. The main reason is the heat transfer coefficient used in the calculation for Fig 4-4 underestimated the heat transfer coefficient by over an order of magnitude. The heat transfer coefficient was calculated using a fully developed internal pipe flow correlation. However, the boundary layer initial growth over each span of the sensor caused by the passing shock wave produced a much larger heat transfer coefficient. A more accurate method of approximating the heat transfer coefficient is to calculate the average heat transfer coefficient using a laminar flat plate correlation, Eq 5.6[47]

$$h_{ave} = \frac{k_{air}}{x}0.664(\text{Re})^{1/2}(\text{Pr})^{1/3} \tag{5.6}$$

where h_{ave} is the average heat transfer coefficient, k_{air} is the air thermal conductivity, and x is the distance from the leading edge. Evaluating h_{ave} for the $\frac{p_4}{p_1} = 4$ condition using air properties at three different air temperatures, 300 K, 350 K, and 400 K, and using the sensing element's width as the characteristic length produced values of 25,661 $\frac{W}{m^2K}$, 25,543 $\frac{W}{m^2K}$, and 25,379 $\frac{W}{m^2K}$, respectively, as summarized in Table 5.3. The calculated h_{ave} values show negligible variation with temperature. Using the average heat transfer coefficient from the flat plate correlation, 25,500 $\frac{W}{m^2K}$, in the numerical model provides an improved match to the measurement, as shown in Fig 5-8. The predicted response was obtained by assuming that each sensing element experiences the same heat flux conditions and the validity of this assumption will be discussed later in this chapter. The time constant of the measured and predicted responses were approximated

Figure 5-5: The pressure and sensor signals recorded by a digital oscilloscope for the p4/p1 = 2 condition. a) Run 1. b) Run 2.

Figure 5-6: The pressure and sensor signals recorded by a digital oscilloscope for the p4/p1 = 3.2 condition. a) Run 1. b) Run 2.
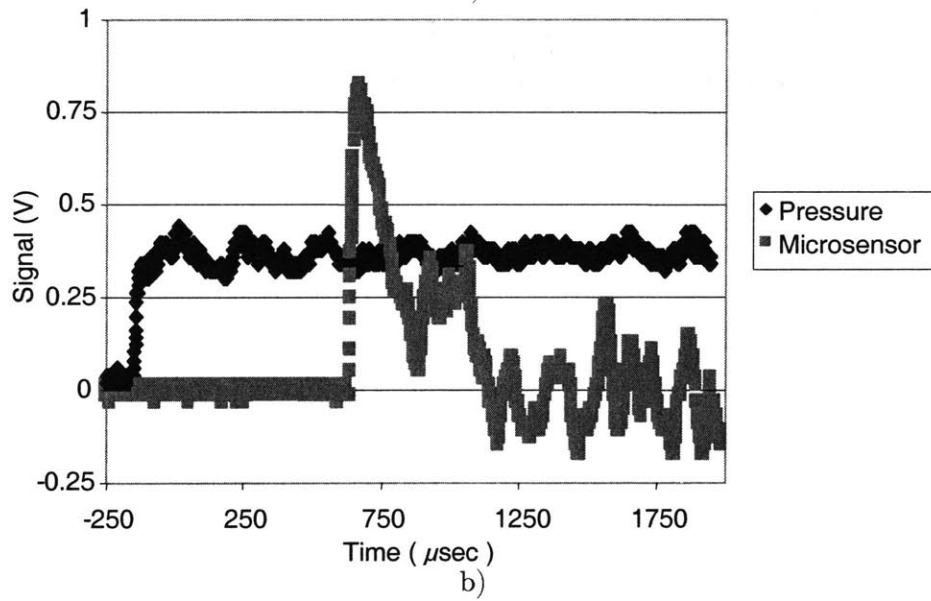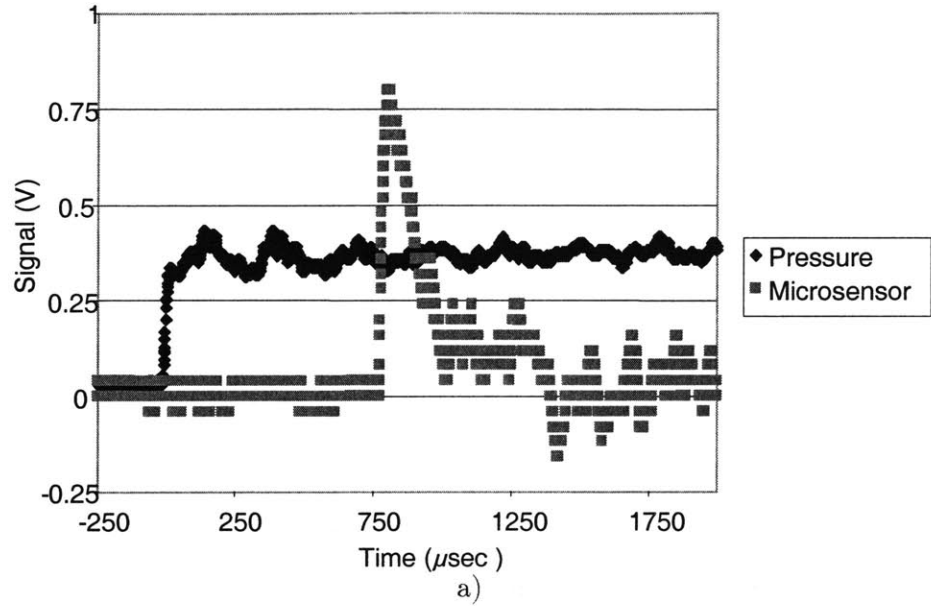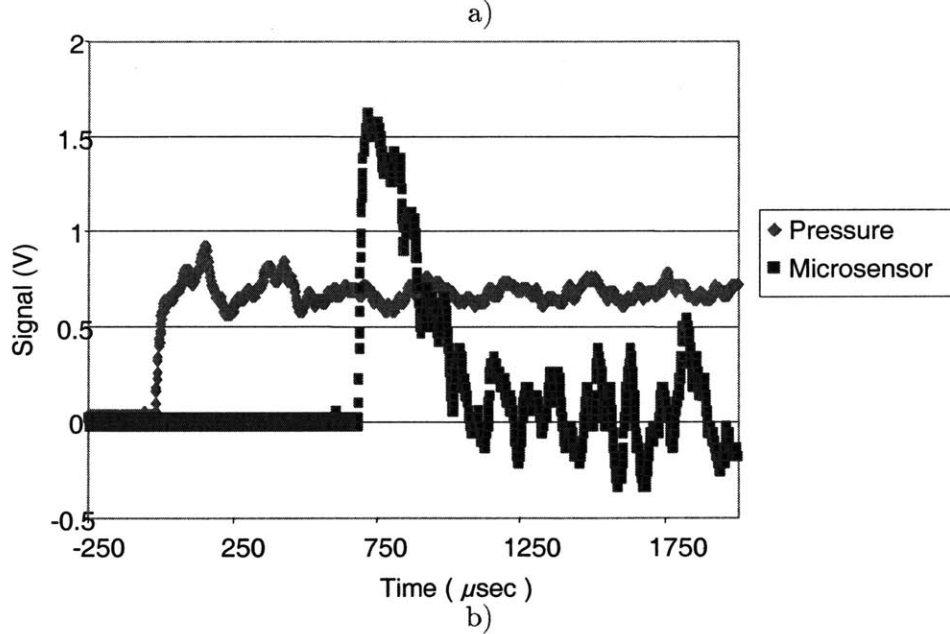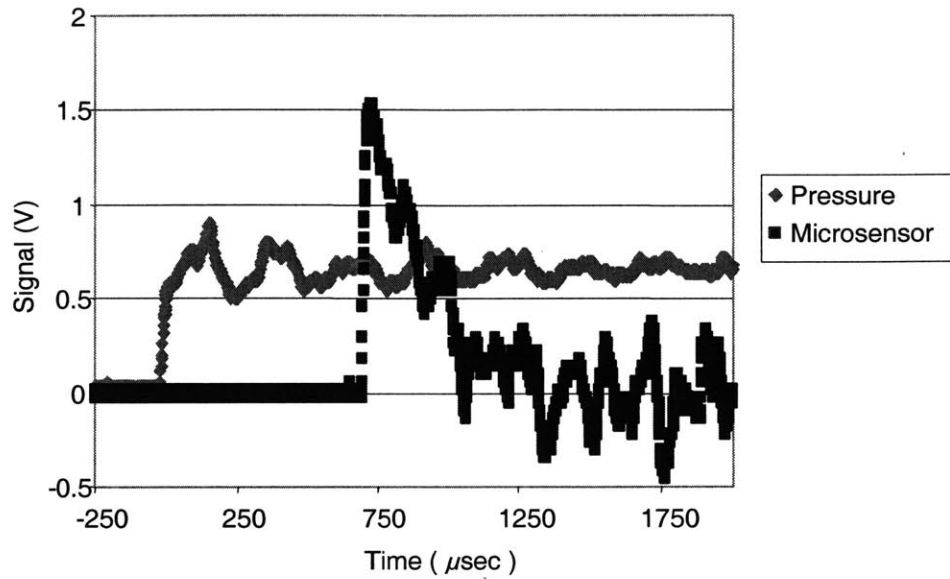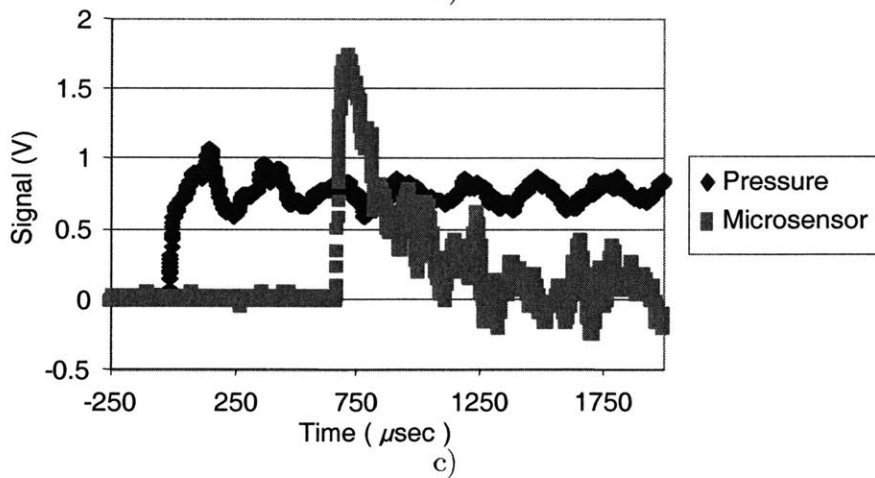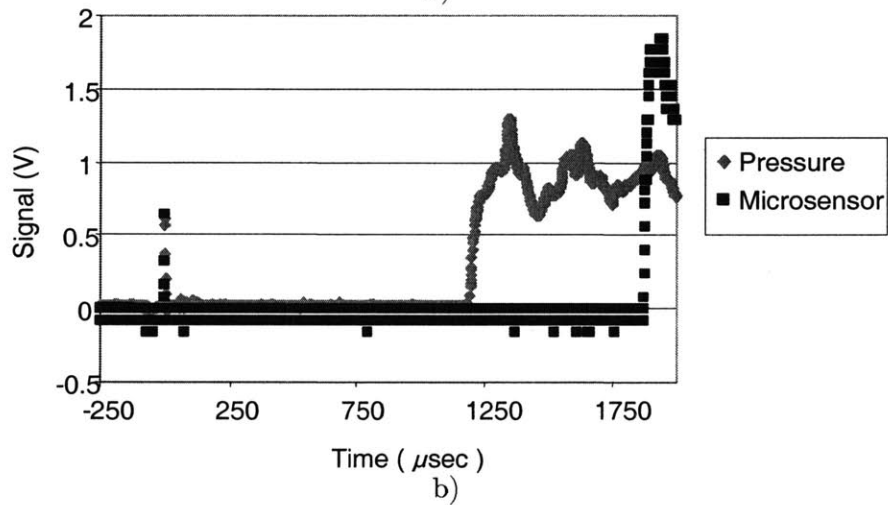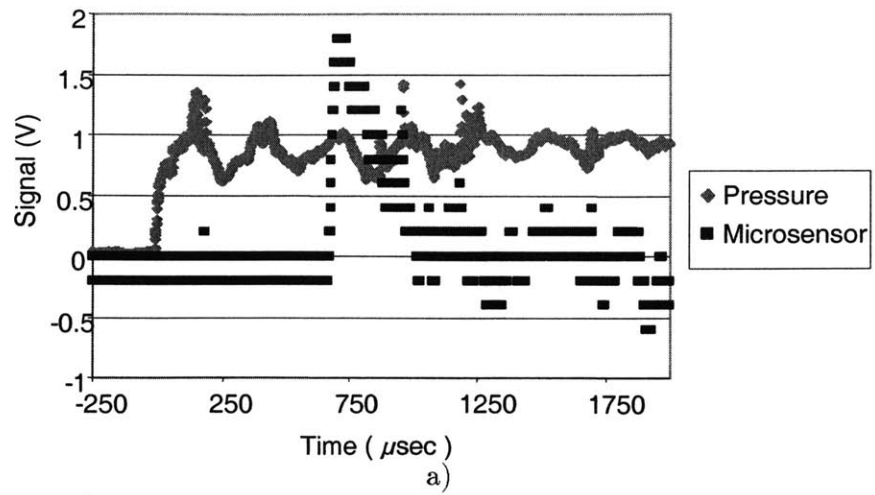
Figure 5-7: The pressure and sensor signals recorded by a digital oscilloscope for the p4/p1 = 4 condition. a) Run 1. b) Run 2. c) Run 3.

84

Table 5.3: Average heat transfer coefficients calculated for the p4/p1=4 condition using a laminar flat plate correlation.

Air temperature (K)	300	350	400
Density $(\frac{kg}{m^3})$	1.161	0.995	0.871
Viscosity $(\frac{Ns}{m^2})$	1.85×10^{-5}	2.08×10^{-5}	2.30×10^{-5}
Thermal conductivity $(\frac{W}{mK})$	2.62×10^{-2}	3.00×10^{-2}	3.38×10^{-2}
Pr	0.707	0.7	0.69
velocity $(\frac{m}{s})$	173	173	173
x (μm)	4	4	4
Re	43	33	26
$h_{ave}(\frac{W}{m^2K})$	25,661	25,437	25,379

by fitting exponential curves to them and are approximately 9 μsec and 6.5 μsec, respectively. The difference between the measured transient response and that of the model is due to the electronics. As discussed in the Experimental Setup chapter, the electronics do not reproduce the transient response perfectly.

Despite the match in transient response, the predicted response's magnitude for the $\frac{p4}{p1} = 4$ condition is approximately 15 % greater than the measured response's magnitude. The predicted response was obtained by assuming that the sensing element's width is the characteristic length, calculating an average heat transfer coefficient, and assuming that each sensing element experienced the same heat flux. However, a 2-D Fluent CFD simulation of the flow around the six sensing elements show that the boundary layer of each sensing element is affected by previous sensing element(s), Figs 5-9, 5-10, and 5-11. The 2-D Fluent CFD simulations were done by Yifang Gong of MIT's GTL and the boundary conditions are as follows: isothermal wall temperature of 300 K, isothermal sensing element temperature of 440 K, uniform flow velocity, temperature, and pressure upstream of the sensing elements (whose values are summarized in Table 5.1). The simulation is only for the flow around the center of each sensing element and the temperature at the center of the sensing elements was obtained from the numerical model assuming a TCR of 0.009 $\frac{1}{K}$. The temperature at the center of the sensing elements was assumed to be constant because the simulation is only used to obtain an approximate flow field.

According to the flow velocity and temperature variations among the sensing elements, the heat transfer coefficient is different for each sensing element and the upper bound is calculated using a sensing element's width, 4 μm, as the characteristic length for a flat plate correlation

85
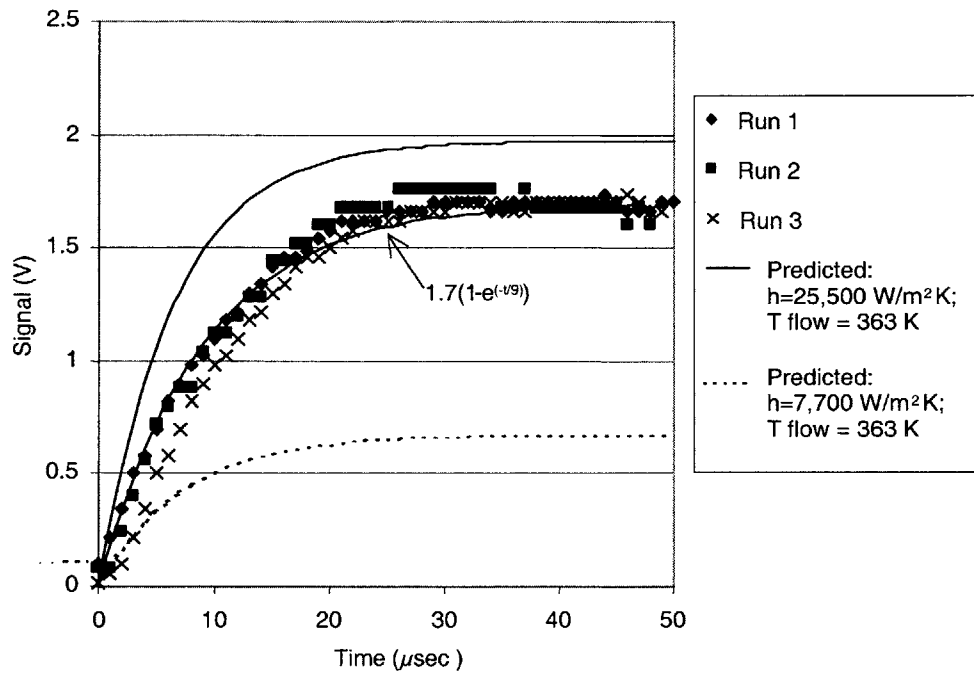
Figure 5-8: The sensor's response in the shock tube for p4/p1 = 4. The time scale is zeroed to the time when the sensor started to experience the shock wave. Responses were fitted with an exponential curve to approximate the time constant. h = 25,500 W/m^2K was calculated from a flat plate correlation using the microsensor's width, 4 microns, as the characteristic length. h = 7,700 W/m^2K was calculated from a flat plate correlation using the distance across all the sensing elements, 6 elements x 4 microns wide + 5 spacings x 4 microns wide = 44 microns, as the characteristic length.

and the lower bound is calculated from a flat plate correlation using the distance across all the sensing elements, 6 elements multiplied by 4 microns wide per spacing + 5 spacings multiplied by 4 microns wide per spacing = 44 microns, as the characteristic length. Replacing x in the previous flat plate correlation with 44 μm for the $\frac{p4}{p1} = 4$ condition, h_{ave} is approximately 7,700 $\frac{W}{m^2 K}$. The magnitude of the predicted response using this value is 60% lower than the magnitude of the measured response, as shown in Fig 5-8. However, the time constant is 7 μsec, which is similar to the previous values.

The hypothesis that the heat transfer coefficient is between the bounds discussed in the previous paragraph is further supported by experiments where the sensor is rotated 90 degrees such that the flow is along the sensing elements' length. The magnitude of the sensor's response in this configuration under the same conditions is approximately 15 % lower than that of the cross-flow configuration, as shown in Fig 5-12. The lower magnitude may be due to the lower driver pressure, p_4, or a change in the heat transfer coefficient. The contribution to the lower ma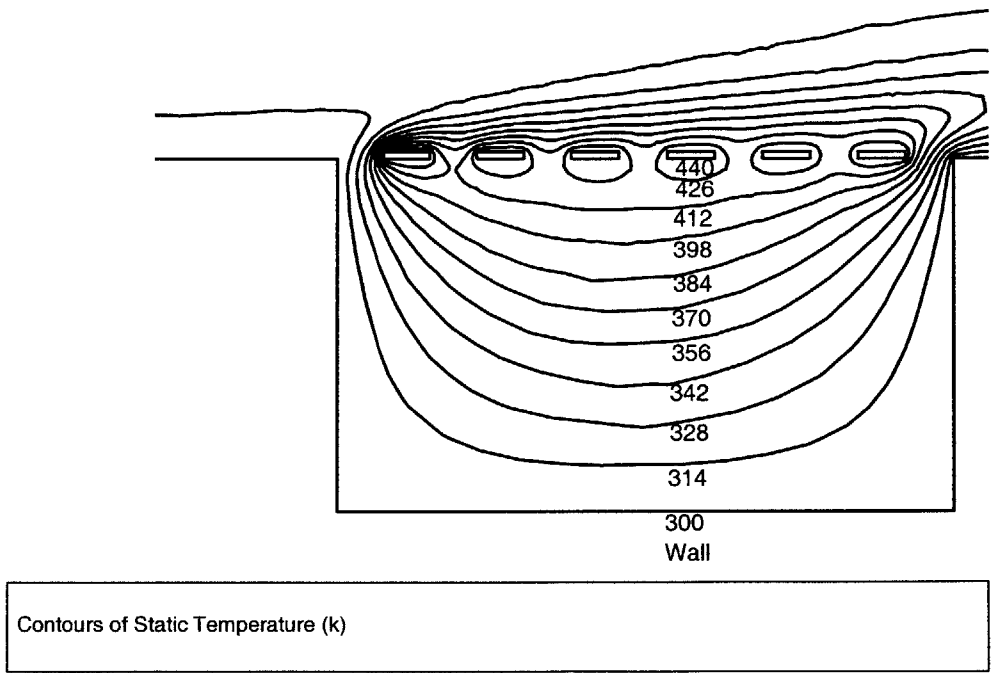gnitude by the lower driver pressure is negligible when the signal magnitude from a $\frac{p4}{p1} = 4$, Fig 5-12, condition is compared to that from a $\frac{p4}{p1} = 3.2$ condition, Fig 5-16. The signal magnitude for the $\frac{p4}{p1} = 3.2$ condition is greater than that of the rotated configuration, Fig 5-12. The lower signal amplitude for the rotated configuration may be due to the larger distance over which heat transfer occurs. Each span is 50 μm long with at least 4 μm upstream, the serpentine bends, which is greater than the sensing element's width.

The previous heat transfer calculation from a flat plate correlation provided bounds for the heat flux. The 2-D Fluent CFD simulation showed that the flow around each sensing element is affected by previous element(s). The flow variations in velocity and temperature, as shown in Figs 5-9, 5-10, and 5-11, cause the heat flux from each sensing element to vary and was calculated in the simulation. The first sensing element experiences the largest heat flux and the heat fluxes from the subsequent sensing elements reduced by approximately 50%, as shown in Fig 5-13. The heat flux profile along the length of each sensing element was calculated by assuming that it is proportional to the difference between the flow temperature and the temperatures along the length of the sensing element. The heat fluxes at a particular node, lengthwise location, for the six sensing elements were average to calculate an average heat flux profile. The predicted response using the average heat flux profile has a 7 μsec time constant

90

80

70

60

50

40

30

20

10

Sensing
Element

0

Wall

Contours of Velocity Magnitude (m/s)

a)

440
426
412
398
384
370
356
342
328
314
300

Wall

Contours of Static Temperature (k)
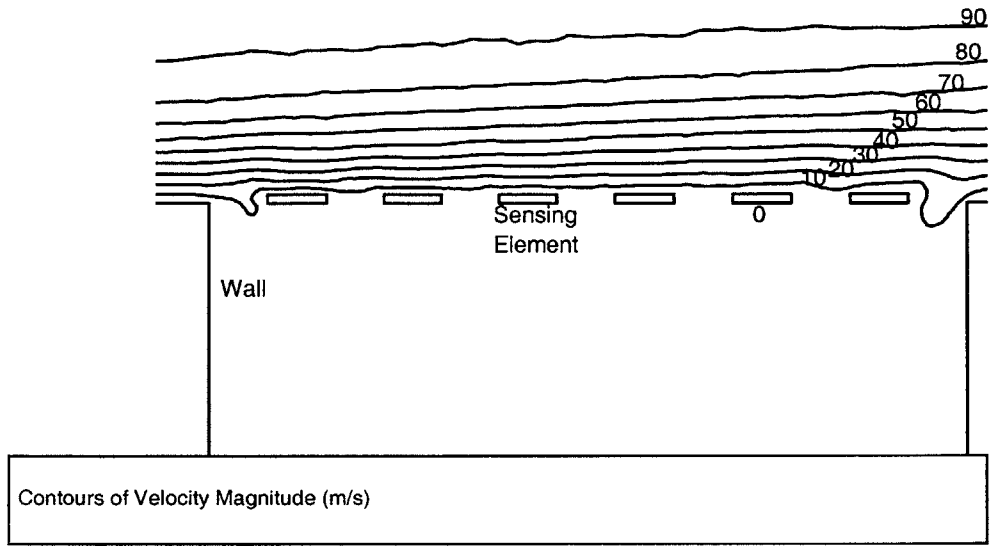
b)

Figure 5-9: Results from a 2-D Fluent CFD simulation for the p4/p1 = 2 condition. a) Velocity contour. b) Temperature contour.

Contours of Velocity Magnitude (m/s)

a)

Contours of Static Temperature (k)

b)

Figure 5-10: Results from a 2-D Fluent CFD simulation for the p4/p1 = 3.2 condition. a) Velocity contour. b) Temperature contour.

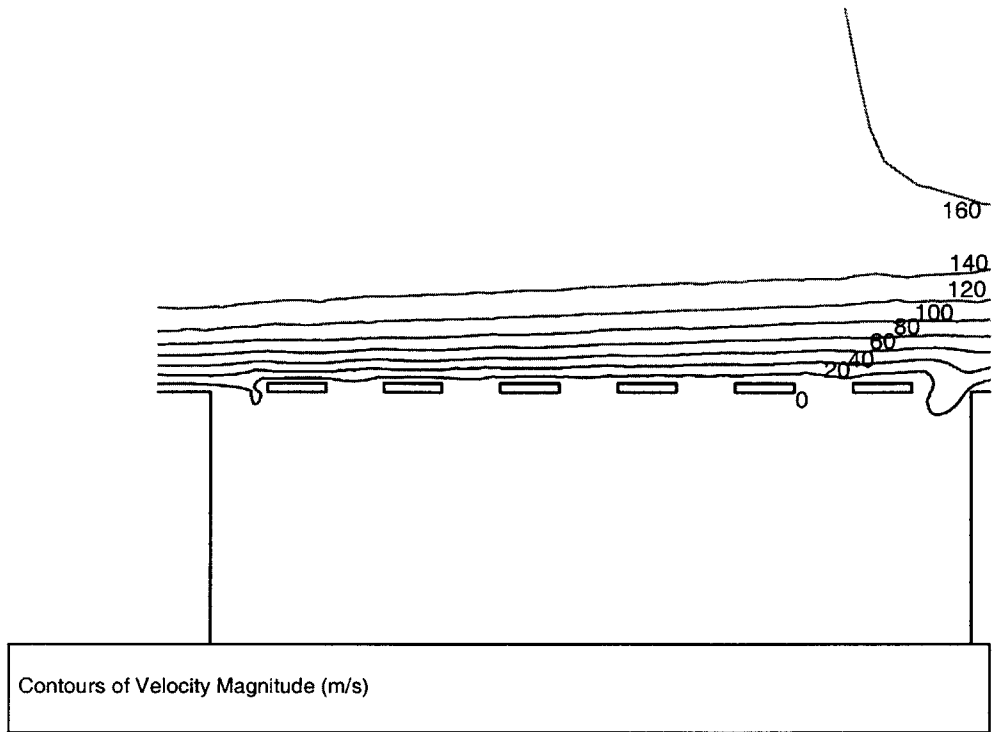Contours of Velocity Magnitude (m/s)

a)

Contours of Static Temperature (k)
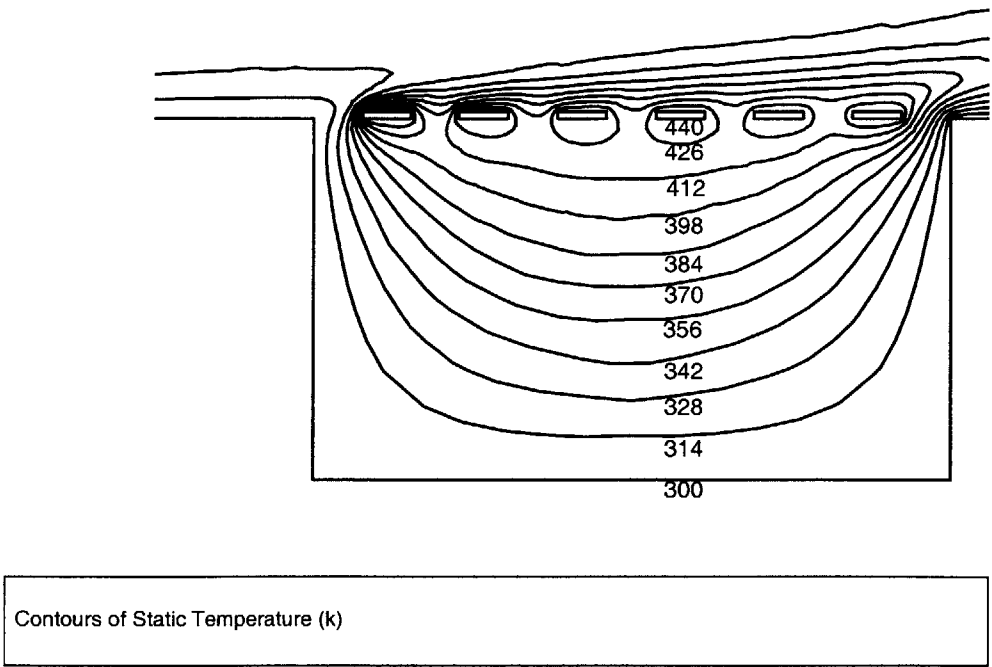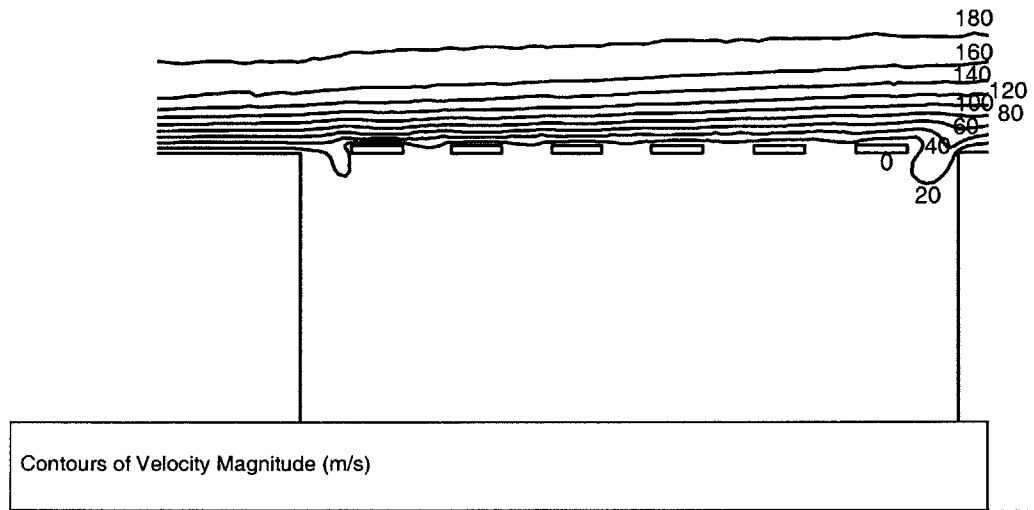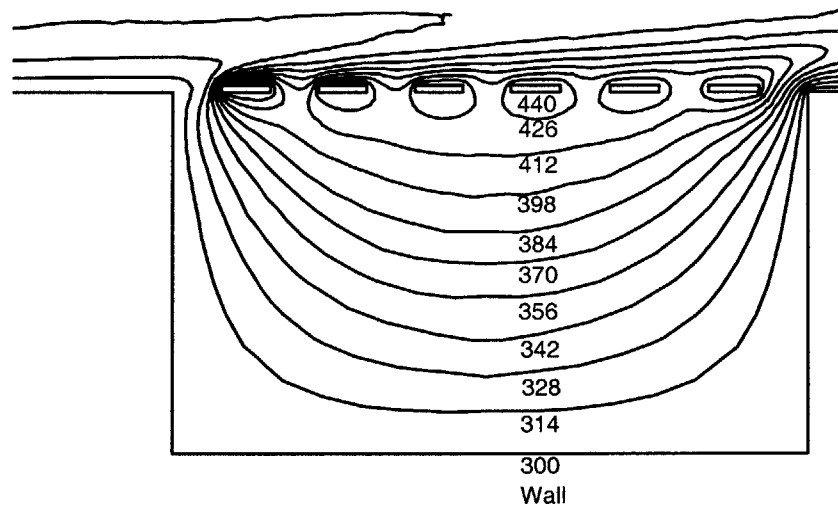
b)

Figure 5-11: Results from a 2-D Fluent CFD simulation for the p4/p1 = 4 condition. a) Velocity contour. b) Temperature contour.
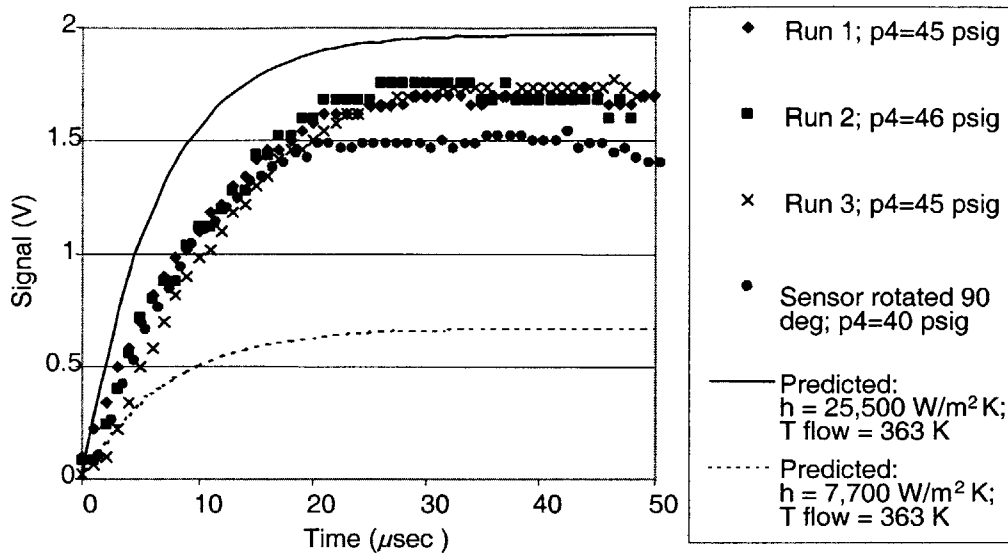
Figure 5-12: The sensor's response when it is rotated 90 degrees from the original configuration. The flow is along the sensing elements' length. The driver pressure is lower, p4 = 40 psig, than Runs 1-3.

and the magnitude is approximately 26% lower than that of the measured response, Fig 5-14.

The previous analysis to predict the sensor response was repeated for two additional conditions: $\frac{p4}{p1} = 2$ and 3.2. Average heat transfer coefficients were calculated using a laminar flat correlation and 4 μm and 44 μm as characteristic lengths. Also, average heat flux profiles were approximated for both conditions. The predicted and measured responses are shown in Fig 5-15 and 5-16.

Similar to the previous condition, $\frac{p4}{p1} = 4$, the laminar flat plate correlation was used to estimate the average heat transfer coefficient for the conditions $\frac{p4}{p1} = 2$ and 3.2. Since the air properties do not vary significantly for the temperature range of interest, 350 K $\pm$ 50 K, the average heat transfer coefficients were calculated using air properties at 350 K. The average heat transfer coefficients for the $\frac{p4}{p1} = 2$ condition using 4 μm and 44 μm as the characteristic lengths are 5,400 $\frac{W}{m^2K}$ and 17,950 $\frac{W}{m^2K}$, respectively. Similarly, the average heat transfer coefficients for the $\frac{p4}{p1} = 3.2$ condition using 4 μm and 44 μm as the characteristic lengths are 7,050 $\frac{W}{m^2K}$ and 23,300 $\frac{W}{m^2K}$, respectively. Again, the measured transient responses match the predicted transient responses, as shown in Fig 5-15 and 5-16 and summarized in Table 5.4. However,
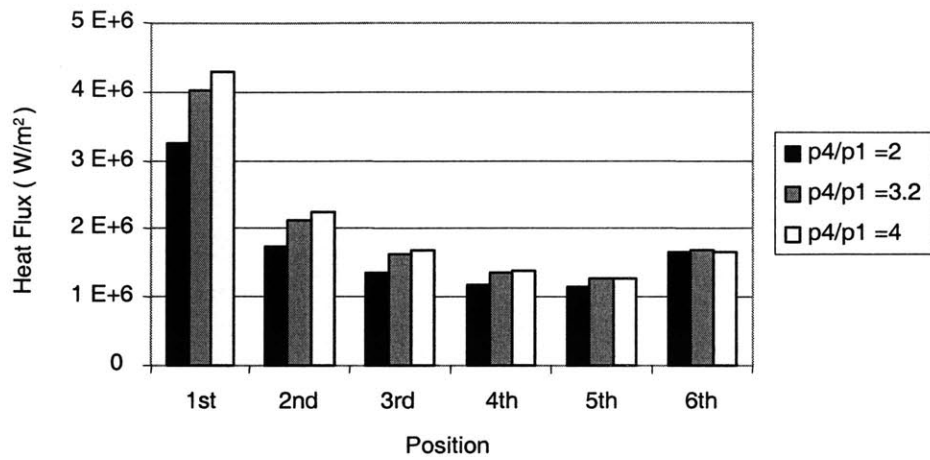
Figure 5-13: Heat flux at the center of each sensing element calculated in the 2-D Fluent CFD simulation.
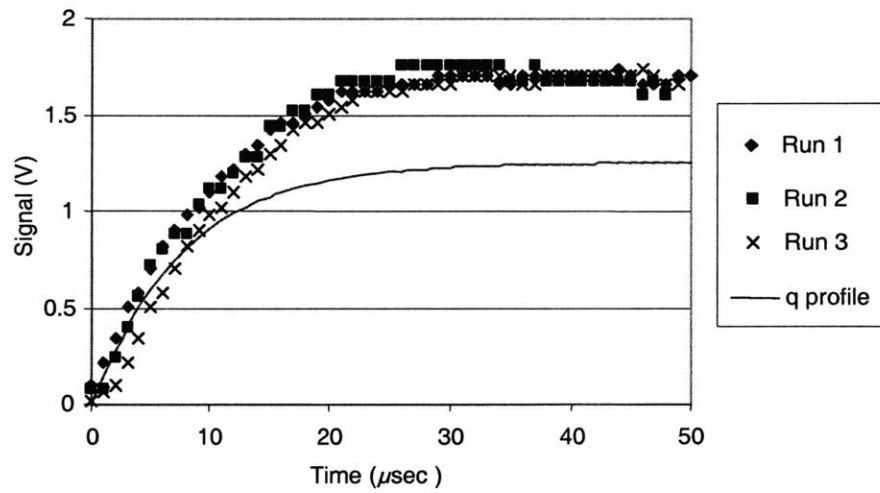
Figure 5-14: The predicted sensor response using the average heat flux profile for the condition p4/p1=4.
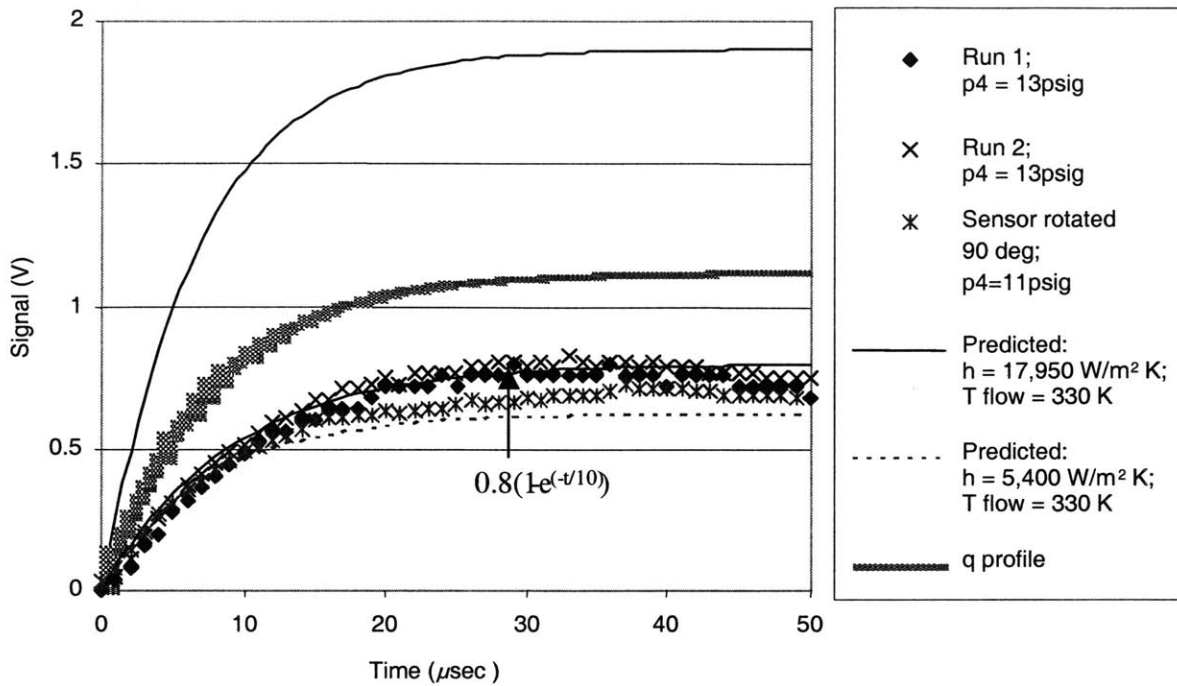
Figure 5-15: The predicted and measured sensor response when subjected to a shock wave with a p4/p1=2 initial condition.

the signal magnitude for the conditions $\frac{p_4}{p_1} = 2$ and 3.2 differ by 138% and 25%, respectively, when a 4 μm characteristic length is used and by 25% and 59%, respectively, when a 44 μm characteristic length is used, Table 5.5. However, the measured responses were bounded by the predicted responses obtained using these two characteristic lengths.

The sensor's response is determined by its dimensions, material properties, temperature and by the flow's temperature and properties. The sensor's signal magnitude is significantly influenced by the convection conditions: the heat transfer coefficient and the temperature difference between the flow and the sensor. The relatively large difference between the measured and predicted response is maybe due to the inaccurate description of the convection heat transfer. The 2-D Fluent CFD simulation results show that the flow field around each sensing element is influenced by preceding sensing elements and, therefore, a flat plate correlation cannot be used to accurately calculate the heat transfer coefficient. In addition, a thermal boundary layer starts to develop at the first sensing element which reduces the heat flux to the flow from the
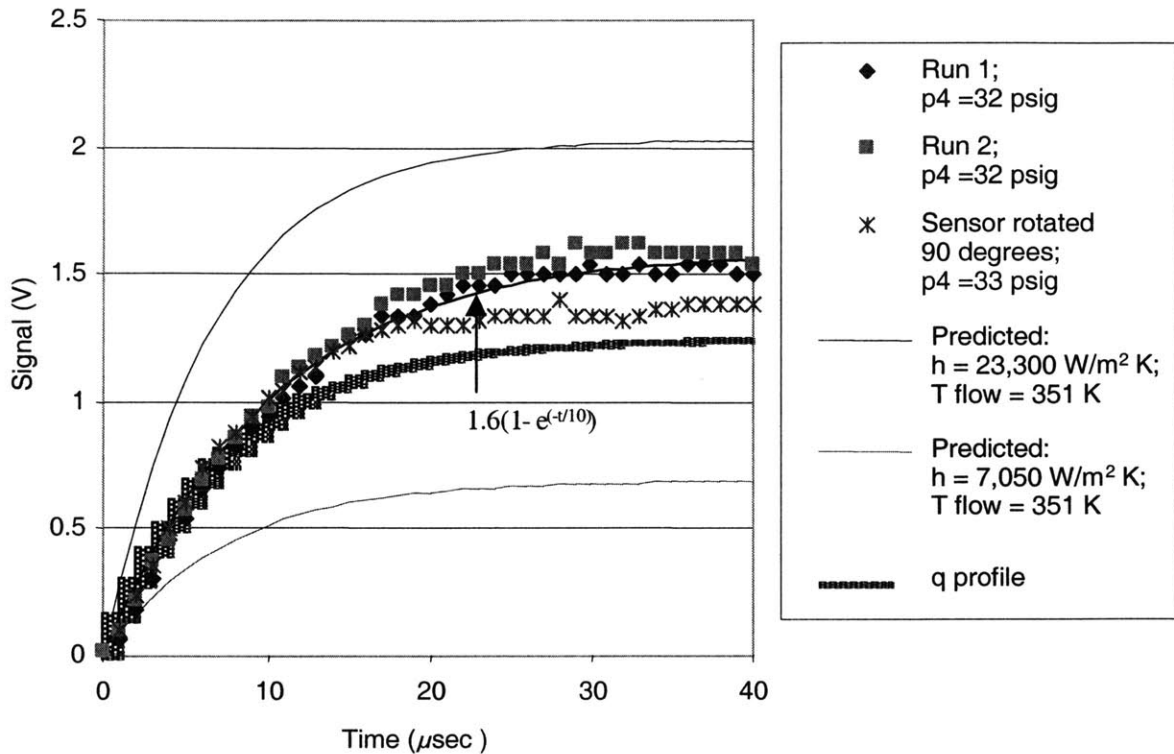
Figure 5-16: The predicted and measured sensor response when subjected to a shock wave with a p4/p1=3.2 initial condition.

Table 5.4: Time constants for the predicted and measured responses for different shock tube conditions. The time constants for the predicted responses using different methods to model the heat flux are shown.

Initial pressure ratio	2	3.2	4
Flat plate correlation: 4 μm characteristic length	6.3 μsec	6.5 μsec	6.5 μsec
Flat plate correlation: 44 μm characteristic length	7.5 μsec	7 μsec	7 μsec
Average heat flux profile	7.5 μsec	7.5 μsec	7 μsec
Measured response	10 μsec	10 μsec	9 μsec

Table 5.5: The signal amplitudes for the predicted and measured response for different shock tube conditions.

Initial pressure ratio	2	3.2	4
Flat plate correlation: 4 μm characteristic length	1.9 V	2.0 V	2.0 V
Flat plate correlation: 44 μm characteristic length	0.6 V	0.7 V	0.7 V
Average heat flux profile	1.1 V	1.2 V	1.2 V
Measured response	0.8 V	1.6 V	1.7 V

94

subsequent sensing elements. The thermal boundary layer is thicker for the $\frac{p_4}{p_1} = 2$ condition because the slower air speed allows more time for heat to transfer from the sensing element to the air. Thus, the signal magnitude decreases more at the lower air speed, i.e. lower $\frac{p_4}{p_1}$, as seen by comparing the signal magnitude difference between $\frac{p_4}{p_1} = 4$ and 3.2 to that between $\frac{p_4}{p_1} = 3.2$ and 2.

However, its transient response, which was quantified using the time constant, is influenced more by the material properties and dimensions than the flow properties when the time constant is dominated by the time constant associated with conduction to the support because of the large aspect ratio (100). A brief discussion on time constant can be found in Chapter 1 Previous Work section. Consequently, the time constants of the measured responses matched those of the predicted responses within a few percent because the convection heat transfer uncertainties do not significantly influence the time constants.

The noise measured for these measurements was approximately 50 mV, which is over 1 order of magnitude lower than the signals measured. The noise from the electronics dominated the measured noise.

5.3 Sensor Design Evaluation

The results from the furnace and shock tube experiments will be used to assess the sensor's design feasibility. This section will use the shock tube results to discuss the expected signal when the sensor is used in the microengine. A comparison of the predicted heat flux fluctuation amplitude in the microengine to the predicted heat flux step change in the shock tube experiments suggest that the sensor will have a detectable signal when incorporated into the microengine to measure blade passing frequency. The expected signal will then be compared to the noise measured in the shock tube test. Finally, design recommendations will be made using lessons learned from the furnace and shock tube experiments. The sensor's signal may be increased with design changes that eliminates multiple parallel sensing elements and by adjusting the doping level to increase the TCR.

The shock tube results show the sensor's transient response and signal levels for different heat transfer conditions. The sensor does not have time to reach steady state as the blades

95

pass beneath it at the maximum blade passing frequency. The period between blade passings is 5 μsec and, therefore, the signal rise occurs up to 2.5 μsec. The expected heat flux amplitude at the center of a sensing element when the sensor operated as a cold-wire, i.e. Joule heating is negligible, is approximately $3\text{x}10^6$ $\frac{\text{W}}{\text{m}^2}$, Fig 2-21. Assuming that the convection heat transfer decreases across the sensing elements when the sensor is in the microengine similarly to when it is in the shock tube, Fig 5-13, the shock tube measurement and the predicted response using the average heat flux profile can be used to estimate the expected response when the sensor is in the microengine. The heat flux at the center of the sensing element for the $\frac{p_4}{p_1} = 2$ condition is approximately $3.2\text{x}10^6$ $\frac{\text{W}}{\text{m}^2}$, which over-estimated the measured response. Using the measured response for the $\frac{p_4}{p_1} = 2$ condition, the signal at 2.5 μsec for Runs 1 and 2 are approximately 0.12 V and 0.15 V, respectively, which correspond to $\frac{\Delta R}{R} = 0.08$ % ($\Delta T = 0.9$ K where TCR was assumed to be 0.09 $\frac{\%}{K}$) and $\frac{\Delta R}{R} = 0.1$ % ($\Delta T = 1.1$ K where TCR was assumed to be 0.09 $\frac{\%}{K}$), respectively. The room temperature resistance of the sensor used for the tests is 11,900 kohms, which gives $\Delta R = 9.5$ ohms and 11.9 ohms for Runs 1 and 2, respectively. These signals were produced with a 1.5 mA driving current, thus, $\Delta V = 14$ mV and 18 mV for Runs 1 and 2, respectively. This conservative estimate suggests that the sensor's signal when used as a cold wire will be detectable with low-noise electronics that condition and amplify the signal. The electronics must contribute less than approximately 10 mV to the signal to obtain a S/N that gives meaningful measurements. In addition, the electronics must have sufficient bandwidth to reproduce the transient behavior of the sensor's signal. The electronics used for signal conditioning and amplification in the shock tube experiments were designed to measure the transient response in the shock tube and filter low frequency components of the signal. This design can be used to condition and amplify a high frequency signal, such as the one produced by the heat fluctuation from passing blades in the microengine. However, the noise must be reduced to below approximately 10 mV.

The sensor's signal can be increased by increasing the resistance change per unit increase in temperature and/or the heat flux into/out of the sensing elements. The former involves increasing the TCR. The signal is proportional to the TCR and the S/N is proportional to the square of the TCR. The TCR is a function of the sensor material and, in the case of a polysilicon sensor, the TCR depends on the grain size and doping level. A -0.4 $\frac{\%}{K}$ TCR was

measured by Luder[46] from polysilicon with a different boron concentration. A TCR with a larger absolute value will increase the signal level and S/N. However, the sensor's geometry must be designed such that the total resistance of the sensor, electrical contacts, and electrical leads is still dominated by the sensor at the operating temperature. The sensor's signal will increase by approximately a factor of four if the TCR's absolute value is increased to 0.4 $\frac{\%}{K}$.

Unlike increasing the TCR, increasing the heat flux into or out of the sensing elements requires a design change rather than a process change. As shown in the previous section, a thermal boundary layer develops starting from the first sensing elements and reduces the heat flux into or out of the subsequent sensing elements. This reduction in heat transfer may not occur if the sensor is operated as a cold-wire. However, the heat flux may still be reduced because the closely space sensing elements increases the characteristic length, which decreases the heat transfer coefficient. These two problems can be solved by increasing the spacing between sensing elements. One sensing element can be placed in each spacing between blades and connected in series with polysilicon on the bottom surface of Level 2. The polysilicon connection must be designed with a geometry that makes its resistance insignificant compared to the sensing elements. This design will approximately double the average heat flux by eliminating the reduction in convection, as shown in Fig 5-13, when sensing elements are closely space. Also, increasing the number of sensing elements increases the S/N as discussed in the Design Analysis chapter.

Chapter 6

Conclusion

This chapter summarizes the research presented in this thesis and presents some recommendations for future work.

6.1 Summary

The overall project goal was to develop an embedded sensor to measure the microengine's rpm. The scope of the work presented in this thesis is to establish whether using a temperature-based sensor to measure heat flux fluctuation is feasible. A stand-alone device for the preliminary investigation was modelled, designed, and tested to determine such a device's thermal stability, signal levels, and step response.

The device was numerically modelled using Matlab to determine one sensing element's, a span across the undercut, response. Flow around the compressor blade were obtained from a FLUENT 3-D CFD simulation and used in the numerical model to predict the sensor's signal when subjected to the heat transfer conditions at the wall above the compressor blades. The model suggested that the sensor's signal will be on the order of 0.3 K when operated as a cold-wire, increasing with driving current.

Subsequently, such a sensor was fabricated using a two-mask micromachining fabrication process in MTL. Steady state furnace experimental results show that the TCR, 0.09 $\frac{\%}{K}$, is approximately 50 % of the expected value, 0.2 $\frac{\%}{K}$, and that the resistance varies by less than 3 % during anneals at 500°C for up to 85 minutes. Shock tube experiment results showed that the

sensor's time constant agrees with predicted values but the response magnitude was lower. The discrepancies between the predicted and measured signal are due to the inaccurate modelling of the sensing elements' heat flux conditions. However, the sensor response suggests that the sensor will have detectable signals when incorporated into the microengine if low-noise electronics are used. The maximum heat flux at the center of the sensing element when subjected to the heat flux conditions in the microengine was estimated using a 3-D Fluent CFD simulation, which showed that the magnitude is larger than the maximum heat flux at the center of the sensing element when subjected to the shock wave with a p4/p1 = 2 initial condition.

6.2 Recommendations for Future Work

This section presents some recommendations for future work and are divided into three sections: Design, Fabrication, and Testing. The goals for these recommendations are to increase the signal, improve the fabrication process, and reduce development risks.

6.2.1 Design

As discussed in the previous chapter, the sensor's signal can be increased by increasing the TCR's absolute value and/or changing the design to eliminate closely spaced sensing elements. Adjusting the TCR can increase the signal by several factors without much process changes. It involves characterizing the TCR for polysilicon with different deposition temperatures and dopant concentrations. Prior to changing the design, stand-alone sensors with only one sensing element should be fabricated and tested using the shock tube to verify that the signal approaches values predicted by using an average heat transfer coefficient calculated with a flat plate correlation using the sensing element's width as the characteristic length.

6.2.2 Fabrication

The sensor's fabrication process is a relatively simple two-mask process. However, the current design suffers from low yield because the close spacing between sensing elements required alignment to be less than 0.5 μm. The yield is projected to increase to 100 % if the single sensing element concept is adopted. In addition, the current fabrication process for the stand-alone

devices neglects interconnects for the microengine. An interconnect scheme needs to be developed in order for the sensor to be incorporated into the microengine. The interconnect must be compatible with the microengine's fabrication process and operable at high temperatures. Candidate interconnect schemes are thru-wafer interconnect or leads through the sides of the microengine where Level 2 bonds to Level 3. Several researchers have developed thru-wafer interconnects which can be used as a reference for the microengine[50]. However, no work has been done on designing leads thru the seams of bonding surfaces.

6.2.3 Testing

The shock tube results suggest that the current design may produce detectable signals if incorporated into the microengine. Incorporating the sensor into and tested it in a microengine is the only method to determine if the signal is detectable. However, methods for increasing the signals were also suggested and should be investigated before testing it in a microengine. It is hypothesized that the closely spaced sensing element design reduces the average signal and that a single sensing element will produce a larger signal. This can be tested by fabricating devices with only one single sensing element and testing it in the shock tube. In addition, a different dopant level to obtain a larger TCR absolute value can be incorporated into these devices to further increase the signal.

Appendix A

Numerical Model Code

The following is the code in MATLAB used to simulate temperature response of a rectangular sensing element under different boundary conditions. The sensing element is held at constant temperature at the ends and the top surface is subjected to a heat flux.

```
% Created by David Tang, 2000
% Calculate Temperature Response of Rectangular Sensor with ends at a fix temperature.
% This provides a worst case result because the ends limit the flucuation amplitude.
% Subjected to heat flux variation extracted from FLUENT
% modified from sensorJGb.m
clear
rad =[57.55 58.77 60.77 62.77 64.77 66.77 68.77 70.77 72.77 74.77 78.77 82.77 86.77 90.77
      93.31];
q =[1.50E+05 1.31E+05 -1.07e4 -1.13E+05 -2.27e5 -2.58E+05 -1.91e5 -3.52E+04 5.54e4
    9.87E+04 1.02E+05 1.10E+05 1.35E+05 1.56E+05 1.50E+05];
Tflow =[819 814 535 500 473 630 771 795 810 814 815 816 817 818 819];
h = [7916.469174 9378 40.37762528 376.7404997 693.3271652 1517.712816 6592.329141
     7044.1118 6924 7051.368029 6814.088967 6867.672213 7943.220288 8639.192283 7914.138563];

% q_shock is the approximated average heat flux into the sensor calculated from the 2-D
% FLUENT simulation and is used in the section "Hot-Wire" below
```

q_shock=[-317424.9905 -293094.3544 4139.649342 288576.9789 560200.7673 818994.9316 1008894.461 1195557.518 1358434.471 1453120.328 1566325.455 1603801.659 1612989.73 1627841.711 1649268.494 1668694.154 1666858.515 1689947.698 1710886.575 1714547.618 1717418.779 1745720.842 1724268.935 1720871.073 1727708.333 1727708.333 1720871.073 1724268.935 1745720.842 1717418.779 1714547.618 1710886.575 1689947.698 1666858.515 1668694.154 1649268.494 1627841.711 1612989.73 1603801.659 1566325.455 1453120.328 1358434.471 1195557.518 1008894.461 818994.9316 560200.7673 288576.9789 4139.649342 -293094.3544 -317424.9905];

%SENSOR DIMENSIONS/PROPERTIES

Cp_sen = 700; %Heat Capacity of sensor (J/kgK)

density_sensor = 2330; %sensor density (kg/m^3)

k_sen = 70; %Sensor thermal conductivity (J/mK)

%This portion for rectangular model of sensor

length =50e-6; % meter

width = 4e-6; % meter

thickness = 0.6e-6; % meter

A_sen = width*length; %Surface area exposed to heat flux.

                    %Assume top surface is subjected to heat flux.

cross_A_sen = width*thickness; %cross sectional area

sensor_mass = density_sensor *cross_A_sen * length;

% rectangular version end

%Numerical Model Simulation parameters

number_node = 50; %number of nodes that the sensor is divided into

time_per_blade = 0.000005; %time for one blade & gap to pass sensor

                    % (ie. 1/frequency) (seconds)

endtime = 0.000070; % duration of simulation (sec)

delta_t = 0.000000001; % incremental step of simulation (sec)

time = [0: delta_t: endtime];

number_cycle = endtime/time_per_blade;

```
nn1= size(q);
n1 = nn1(1);
for i=1: number_cycle,
q_dummy( ( (i-1)*n1+1 ): n1*i ) = q;
rad_dummy( ( (i-1)*n1+1 ): n1*i ) = rad + i*36;
Tflow_dummy( ( (i-1)*n1+1 ): n1*i ) = Tflow;
h_dummy( ( (i-1)*n1+1 ): n1*i ) = h;
end


time_dummy = rad_dummy;
nn_dummy = size(rad_dummy);
n_dummy = nn_dummy(2);


for i = 1: n_dummy,
time_dummy(i) = endtime/( rad_dummy(n_dummy)-rad_dummy(1) ) *
                        (rad_dummy(i) - rad_dummy(1) );
end


q2 = spline (time_dummy, q_dummy, time);
h2 = spline (time_dummy, h_dummy, time);
Tflow2 = spline (time_dummy, Tflow_dummy, time);
nn2 = size(q2);
n2 = nn2(2);
%rad2=time;
%for i=1: n2,
% rad2(i) = 36.0 * (endtime/time_per_blade) /( time(n2)-time(1) ) *( time(i) - time(1) );
%end
%Step change in h: for shock tube
h2(1: (n2/2-0.5)) = 0.0;
h2((n2/2+0.5) : n2) = 7700.0;
% Step change in h END
```

```matlab
k_air = 0.04; % thermal conductivity of air

Temperature = zeros( n2, number_node);

Twall = 300.0; % wall temperature (K)

%Tflow = 810; % flow temperature (K)

Temperature(:,:) = Twall;

h=20000; %heat transfer coefficient

resistance = 11900/6; %resistance of each element

TCR = 0.0009;

%%%%

resistance = resistance/(number_node);

%%%%%

resistance0 = resistance;


%Use this section if want current to oscillate sinusoidally

current=time;

for f=1:n2

current(f) =0; % 3.32e-4+ 3.32e-4*sin(2*3.14*time(f)/time_per_blade);

end

% Sin CURRENT end


% Use this section if want heat flux to oscillate sinusoidally

%for f = 1: n2

% q2(f) = 2000000*sin(2*3.14*time(f)/time_per_blade);

%end

% Heat flux oscillate end


%Use this section if want Flow Temp to oscillate sinusoidally

%Tflow=time;

%for f=1:n2

% Tflow(f) = 810 + 100*sin(2*3.14*time(f)/time_per_blade);

%end
```

% Flow Temperature oscillation end

%This section for a square wave: heat flux

% To model the frequency response of sensor

q_square =6250 + 6250*square(2*pi*500000*time);

% Square section ends

for i=2: (n2-1),

for j = 2: (number_node-1),

resistance = resistance0 * (1 + TCR*(Temperature(i-1,j) - 300));

%varying HEAT FLUX

%Temperature(i,j) = Temperature(i-1,j) + (time(i)-time(i-1))/ (sensor_mass/

number_node)/Cp_sen*(q2(i-1)*A_sen/number_node+k_sen*

cross_A_sen/(length/number_node)*(Temperature(i-1,j-1) +

Temperature(i-1,j+1) -2*Temperature(i-1, j)));

%Temperature(i,j) = Temperature(i-1,j) + (time(i)-time(i-1))/ (sensor_mass/

number_node)/Cp_sen*(q2(i-1)*A_sen/number_node+k_sen*

cross_A_sen/(length/number_node)*(Temperature(i-1,j-1) +

Temperature(i-1,j+1) -2*Temperature(i-1, j)) +k_air*A_sen/

number_node/(5e-6)*(Twall-Temperature(i-1,j)));

%varying FLOW TEMPERATURE

%Temperature(i,j) = Temperature(i-1,j) + (time(i)-time(i-1))/

(sensor_mass/number_node)/Cp_sen*(h*(Tflow(i-1)-Temperature(i-1,j))

*A_sen/number_node+k_sen*cross_A_sen/(length/number_node)*

(Temperature(i-1,j-1) +Temperature(i-1,j+1) -2*Temperature(i-1, j)));

%HOT-WIRE: power dissipation is not negligible compared to heat flux in

%Temperature(i,j) = Temperature(i-1,j) + (time(i)-time(i-1))/ (sensor_mass/

number_node)/Cp_sen*(current(i)^2*resistance+h2(i-1)*(Tflow2(i-1) -

Temperature(i-1,j))*A_sen/number_node+k_sen*cross_A_sen/(length/

number_node)*(Temperature(i-1,j-1) + Temperature(i-1,j+1) -2*

Temperature(i-1, j)));

Temperature(i,j) = Temperature(i-1,j) + (time(i)-time(i-1))/ (sensor_mass/

number_node)/Cp_sen *(0.0015^2*resistance+h2(i-1)*(363-

Temperature(i-1,j))*A_sen/number_node+k_sen*cross_A_sen/

(length/number_node)*(Temperature(i-1,j-1) + Temperature(i-1,j+1) -

2*Temperature(i-1, j)));

% Temperature(i,j) = Temperature(i-1,j) + (time(i)-time(i-1))/ (sensor_mass/

number_node)/Cp_sen *(0.0015^2*resistance+ -h2(i-1)*q_shock(j)*

A_sen/number_node+k_sen*cross_A_sen/(length/number_node)*

(Temperature(i-1,j-1) + Temperature(i-1,j+1) -2*Temperature(i-1, j)));

%Square heat transfer coefficient

%Temperature(i,j) = Temperature(i-1,j) + (time(i)-time(i-1))/ (sensor_mass/

number_node)/Cp_sen*(0.002^2*resistance+q_square(i)*A_sen/

number_node+k_sen*cross_A_sen/(length/number_node)

*(Temperature(i-1,j-1) + Temperature(i-1,j+1) -2*Temperature(i-1, j)));

%STEP heat flux

%Temperature(i,j) = Temperature(i-1,j) + (time(i)-time(i-1))/ (sensor_mass/number_node)/

Cp_sen *(10*(Tflow -Temperature(i-1,j))*A_sen/number_node+

k_sen*cross_A_sen/(length/number_node)*(Temperature(i-1,j-1) +

Temperature(i-1,j+1) -2*Temperature(i-1, j)));

%SINUSOIDAL CURRENT

%Temperature(i,j) = Temperature(i-1,j) + (time(i)-time(i-1))/ (sensor_mass/number_node)/

Cp_sen *(current(i)^2*resistance/number_node + 100*(Tflow -Temperature(i-1,j))

*A_sen/number_node+k_sen*cross_A_sen/(length/number_node)*

(Temperature(i-1,j-1) + Temperature(i-1,j+1) -2*Temperature(i-1, j)));

%Step CURRENT

Temperature(i,j) = Temperature(i-1,j) + (time(i)-time(i-1))/ (sensor_mass/number_node)/

Cp_sen *(0.01^2*resistance/number_node + 100*(Tflow -Temperature(i-1,j))*

A_sen/number_node+k_sen*cross_A_sen/(length/number_node)*

```
                (Temperature(i-1,j-1) + Temperature(i-1,j+1) -2*Temperature(i-1, j)));

end

end

subplot(2,1,1)

plot(time,(Temperature(:,(number_node/2))'));

hold on

plot(time,Temperature(:,5)');

zoom on

subplot(2,1,2)

plot(time,q2)

zoom on


%This section calculates temperature fluctuation for each node.

%Used for calculating average sensor temperature fluctuation in Exel

deltaT = zeros(3,number_node);

deltaT(1,:) = max( Temperature);

deltaT(2,:) = min( Temperature ( ((n2-2*0.000005/delta_t): (n2-1) ),:) );

deltaT(3,:) = deltaT(1,:) - deltaT(2,:);

fid = fopen('deltaT.txt','w');

fprintf(fid,'%12.8f\n',deltaT(3,:));

fclose(fid)
```

Appendix B

Masks Design
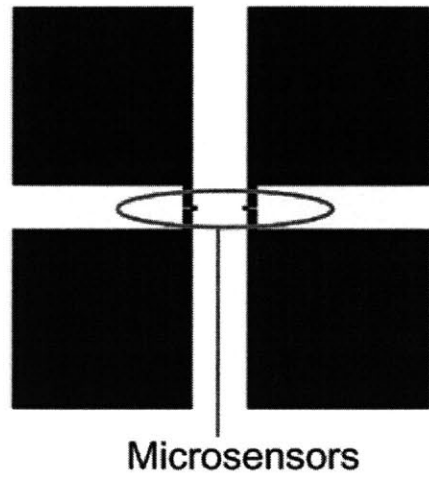
Figure B-1: Mask 1: Sensor Pattern. Clear-field mask. The Sensor close-up pictures are in the subsequent figure.

Figure B-2: Closeup of the sensor pattern. a) Design for the sensor on the left (baseline design). b) Design for the sensor on the right (one end supported design).
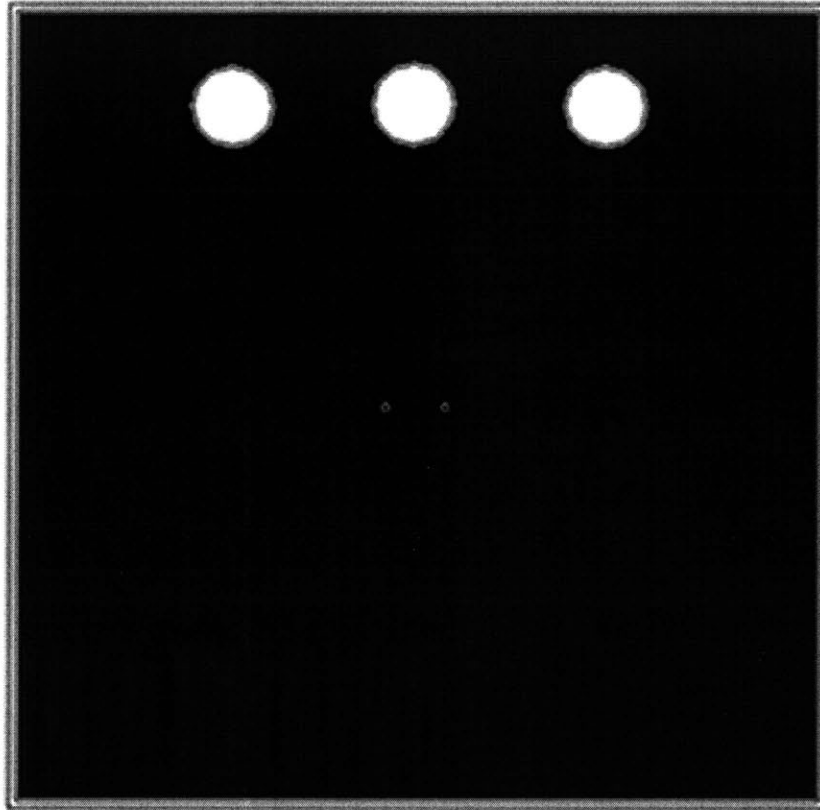
Figure B-3: Mask 2: Oxide Trench Pattern. Dark field mask. The circles at the top are for die identification. The border allows deep etching into the silicon, which is for cleaving the die. Closeup of the oxide trench patterns are in the subsequent figure.

a)   b)
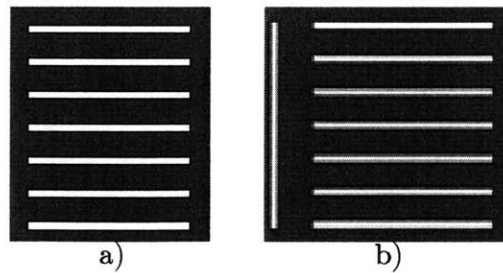
Figure B-4: Closeup of the oxide trench mask pattern. a) Design for the sensor on the left (baseline design). b) Design for the sensor on the right (one end supported design).
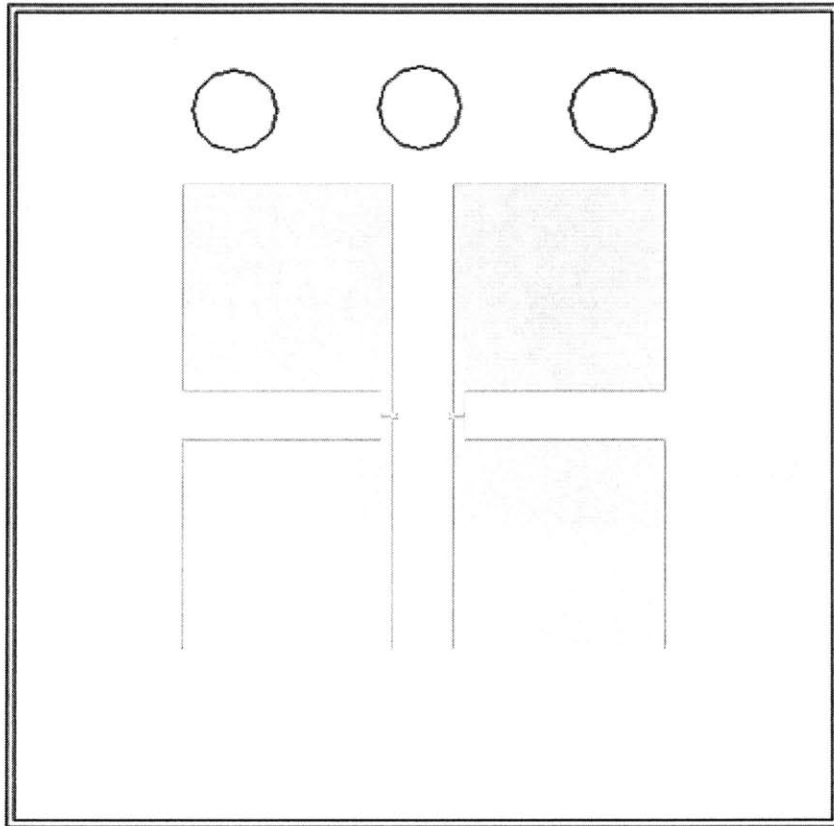
Figure B-5: Overlay of the two masks.

Appendix C

Fabrication Process

This section describes the sensor's fabrication process with recipe specific to MTL's equipment. Process times may need to be adjusted due to variations over time of MTL's equipment process conditions.

| Step	Process	Facility	Equipment	Recipe
1	RCA clean	ICL	RCA hood	
2	Grow thermal oxide: 0.5 μm	ICL	furnace A3	240
3	Deposit poly-silicon: 0.5 μm	ICL	furnace A6	705
4	Ion implant: 80 keV, 5e-15 cm^{-2} B	vendor		
5	Pirahna clean	TRL	acidhood	
6	RCA clean	ICL	RCA hood	
7	LTO deposition: 0.05 μm	ICL	furnace A7	466
8	Anneal at 900 °C for 1 hour	ICL	furnace A2	179
9	BOE	ICL	acid hood	
10	Photolithography	TRL	photolith room	
11	Anisotropic polysilicon etch: 0.5 μm	ICL	AME 5000	Poly-Std
12	Strip photoresist	ICL	asher	
13	Pirahna clean	TRL	acidhood	
14	RCA clean	ICL	RCA hood	

15	LTO: 0.5 μm	ICL	furnace A7	462
16	Densify oxide at 900 °C for 1 hour	ICL	furnace A2	179
17	Photolithography	TRL	photolith room	
18	Anistropic oxide etch: 1 μm	ICL	AME 5000	Isabella LTO
19	Strip photoresist	TRL	asher	
20	Anisotropic silicon etch	TRL	STS1	MIT 69
21	Isotropic silicon etch	TRL	STS1	sf6_2
22	BOE etch	TRL	acidhood	
23	Shadow mask			
24	Metal deposition			

Appendix D

Uncertainty Analysis

This appendix contains the uncertainty analysis for the measured and calculated results presented in this thesis. The analysis is separated in the Independent Measurements (temperature, resistance, current, and voltage) and the Derived Quantities (resistance, shock speed, and pressure).

D.1 Uncertainty Analysis: Independent Measurements

This section quantifies the uncertainty of the independent measurements discussed in this chapter. The uncertainty of the independent measurements will be based on the accuracy of the instruments and/or the smallest division that the instrument is capable of displaying. The independent measurements discussed in this section are the temperature, resistance, current, and voltage measurements.

D.1.1 Temperature Measurements

The sensor's temperature was approximated using a measurement system with a thermocouple and a temperature controller/display. The thermocouple used was a *Omega* 20 mil type K unsheathe thermocouple. The manufacturer specified that its accuracy is ± 2.2°C or 0.75% of the reading, whichever is larger. The maximum temperature read was 700°C and 0.75% of that is 5.25°C. Thus, the maximum bias uncertainty in the temperature measurement that is due to the thermocouple is ± 5.25 K.

The thermocouple was epoxied onto a ceramic fixture such that the thermocouple was about 2.54 cm (1") away from the sensor. The air temperature varies by less than 1K over 5 cm (1.97") at the center of the quartz tube. Since ceramic is a better thermal conductor that air and the distance between the thermocouple and the sensor is less than 5 cm, then the temperature difference between them is less than 1 K. Thus, the bias uncertainty of the sensor's temperature due to the system setup is conservatively approximated to be ± 1 K.

The temperature measurement system's bias uncertainty is calculated by combining both bias uncertainties using Eq D.1[48]

$$b_{sys} = \sqrt{\left(b_1^2 + b_2^2\right)} \qquad (D.1)$$

where b_{sys} is the overall bias uncertainty of the system and b_x is the bias uncertainty from a particular cause. The assumption is that the bias uncertainties from the different causes are associated from independent sources so their maximum errors are not likely to occur simultaneously. This is valid because one bias uncertainty is due to the thermocouple, such as its material and how it was manufactured, and the other bias uncertainty is due to the thermocouple's placement. The overall bias uncertainty is ± 5.3 K.

The thermocouple is connected to and read by a *Omega* CN4400 temperature controller. The manufacturer specified that its accuracy is ± 0.5% of the full-scale, 0°C to 1194°C , + 1°C. Thus, the maximum precision uncertainty in the temperature reading is 6.0°C.

The temperature measurement system's, the thermocouple and the temperature controller, overall uncertainty is calculated with Eq D.2

$$u_y = \sqrt{\left(p_y^2 + b_y^2\right)} \qquad (D.2)$$

where p is the precision uncertainty and b is the biased uncertainty. The assumption is the same as for Eq D.1, the uncertainties are associated with independent sources so their maximum error values are not likely to occur simultaneously. The overall uncertainty of the temperature measurement system is ± 8.0 K

D.1.2   Resistance Measurements: Ohm-meter Measurements

The sensor's was measured using a Fluke 87 True RMS Multimeter. The manufacturer specified that its resistance measurement has an accuracy of ± 0.2% with a range from 400 ohms to 40 Mohms.

D.1.3   Current Measurements

The current supply that was used for the I-V measurements was connected in series with a Weston Electrical Instrument Corporation Model #430 ammeter. The minimum resolution of this ammeter is 0.2 $\frac{mA}{div}$. The precision uncertainty is assumed to be less than the minimum resolution, 0.2 mA. The precision of the current reading from the ammeter is limited to its resolution and, therefore, the precision uncertainty is conservatively estimated to be 0.2 mA. The largest current reading using this ammeter is 2.2 mA and the precision uncertainty is 9%. The bias uncertainty is assumed to be much less than 9% and thus, negligible compared to the precision uncertainty. Thus, the overall uncertainty is conservatively estimated to be 0.2 mA.

D.1.4   Voltage Measurements

The voltage across the sensor for the I-V measurements was measured using the Fluke 87 True RMS Multimeter. The manufacturer specified that its resistance measurement has an accuracy of ± 0.05% with a range from 400 mV to 1000 V.

D.2   Uncertainty Analysis: Derived Quantities

This section quantifies the uncertainty in the derived quantities. The bias uncertainty is calculated using Eq D.3

$$b_y = \sqrt{\Sigma_{i=1}^n \left[\frac{\partial y}{\partial x_i} b_i \right]^2} \tag{D.3}$$

where y is a function of n variables $x_1, x_2, x_3, ..., x_n$ and b is the bias uncertainty. The precision uncertainty is calculated using Eq D.4[49]

$$p_y = \sqrt{\Sigma_{i=1}^n \left[\frac{\partial y}{\partial x_i} p_i \right]^2} \tag{D.4}$$

where p is the precision uncertainty.

D.2.1   Resistance Measurements: I-V measurements

The sensor's resistance from the I-V measurements are given by Eq D.5

$$R = \frac{V}{I} \tag{D.5}$$

where R is the resistance, V is the voltage, and I is the current. The precision uncertainty is calculated from an alternate form of Eq D.4, Eq D.6

$$\frac{u_R}{R} = \sqrt{\left(\frac{u_V}{V}\right)^2 + \left(-\frac{u_I}{I}\right)^2} \tag{D.6}$$

where u is the uncertainty in resistance, voltage, or current. The resistance calculated from the I-V measurements have a precision uncertainty of 9%, which is dominated by the current measurement uncertainty.

D.2.2   Shock Speed Calculations

The shock speed was calculated using Eq D.7

$$U_{shock} = \frac{x_{1,2}}{t_{1,2}} \tag{D.7}$$

where U_{shock} is the shock wave speed, $x_{1,2}$ is the distance between the instrumentation ports #1 and #2, 0.30 m, and $t_{1,2}$ is the time between the pressure transducer and sensor excitations. Similar to the Resistance Measurement uncertainty, the shock speed precision uncertainty is calculated using Eq D.8

$$\frac{u_U}{U} = \sqrt{\left(\frac{u_x}{x_{1,2}}\right)^2 + \left(-\frac{u_t}{t_{1,2}}\right)^2} \tag{D.8}$$

120

Table D.1: Summary of the pressure behind the shock wave for the three p4/p1 conditions.

p4/p1	2	2	3.2	3.2	4	4	4
run #	1	2	1	2	1	2	3
Pressure: Measured (V)	0.37	0.37	0.7	0.7	0.9	0.9	0.8
Uncertainty: Measured (V)	± 0.05	± 0.05	± 0.1	± 0.1	± 0.15	± 0.15	± 0.1
Pressure: Converted (atm)	1.40	1.40	1.70	1.70	1.88	1.88	1.80
Uncertainty: Converted	13 %	13 %	14 %	14 %	17 %	17 %	13 %

where u is the uncertainty in shock speed, distance, or time. The uncertainty in the distance the instrumentation ports #1 and #2 is due to measurement error and is conservatively estimated to be ± 0.01 m. The uncertainty in the time between excitation is due to the sampling time of the oscilloscope and the time between samples is 1 μsec. The time uncertainty is 2 μsec because the start and end times each contribute 1 μsec. The shock speed uncertainty for the p4/p1 = 2, 3.2, and 4 conditions is 3 %.

D.2.3 Pressure Measurement

The pressure is measured after calibrating the 250 psi Kulite pressure transducer. The calibration curve is shown in Fig D-1 and was used to calculate the pressure behind the shock wave from the pressure transducer's signal. The signals for the p4/p1 =2, 3.2, and 4 conditions are summarized in Table D.1. The pressure was calculated from the voltage signal using Eq D.9

$$P = \frac{(V - 1.1692)}{1.0981} \tag{D.9}$$

The pressure precision uncertainties were calculated using Eq D.10

$$\frac{u_p}{P} = \frac{u_V}{V} \tag{D.10}$$

u_V was due to the pressure fluctuations in the signal. Average pressures (V) were used in the conversion to atm units and the uncertainties were estimated based on the fluctuation amplitudes.
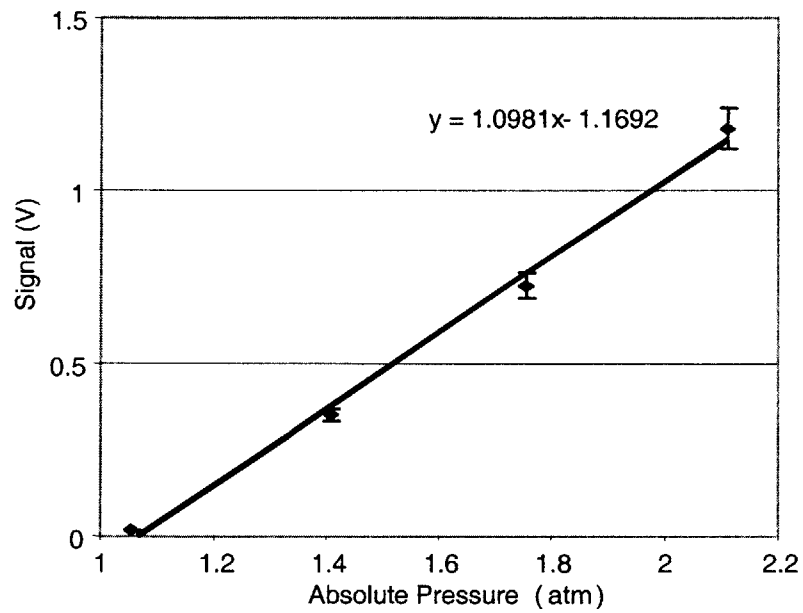
Figure D-1: Calibration curve for a 250 psi Kulite pressure transducer. The pressure transducer was placed in the shock tube's instrumentation port #1 and was used to measure the pressure profile as the shock wave passes it.

Bibliography

[1] A.H. Epstein, Senturia, Anathasuresh, Ayon, Breuer, Chen, Ehrich, Esteve, Gauba, Ghodssi, Groshenry, Jacobson, Lang, Lin, Mehra, Mur Miranda, Nagle, Orr, Piekos, Schmidt, Shirley, Spearing, Tan, Tzeng, Waitz, "Power MEMS and Microengines," presented at IEEE Conference on *Solid State Sensors and Actuators*, Chicago, IL, June 1997

[2] A.H. Epstein and S. D. Senturia, "Macro Power from Micro Machinery," *Science*, May 23, 1997, Vol 276, p. 1211

[3] Epstein, Senturia, Al-Midani, Anathasuresh, Ayon, Breuer, Chen, Ehrich, Esteve, Frechette, Gauba, Ghodssi, Groshenry, Jacobson, Kerrobrock, Lang, Lin, London, Lopata, Mehra, Mur Miranda, Nagle, Orr, Piekos, Schmidt, Shirley, Spearing, Tan, Tzeng, Waitz, "Micro-Heat Engines, Gas Turbines, and Rocket Engines", AIAA 97-1773, presented at 28th AIAA Fluid Dynamics Conference, 4th AIAA Shear Flow Control Conference, Snowmass Village, CO, June 29-July 2, 1997

[4] Protz, *An Assessment of the Aerodynamic, Thermodynamic, and Manufacturing Issues for the Design, Development, and Microfabrication of a Demonstration Micro Engine*, Aeronautics and Astronautics Ph.D. thesis, Massachusetts Institute of Technology, September 2000

[5] Drela, personal communication, Massachusetts Institute of Technology

[6] Kerrebrock, **Aircraft Engines and Gas Turbines**, The MIT Press, 1992, pp. 36-39

[7] Frechette, "Development of a Microfabricated Silicon Motor-Driven Compression System", Ph.D. thesis, Massachusetts Institute of Technology, 2000, pp. 46-47

[8] Kerrebrock, pp.189-192

[9] www.kulite.com

[10] Jacobson, personal communication, Massachusetts Institute of Technology

[11] Dennis, **Photodetectors- An Introduction to Current Technology**, Plenum Press, 1987, pp.111-113

[12] Jiang, Tai, Ho, Li, "A Micromachined Polysilicon Hot-Wire Anemometer", *Solid-State Sensor and Actuator Workshop*, Hilton Head, South Carolina, June 1994, p. 264-267

[13] Epstein and Guenette, "High-Frequency Response Heat-Flux Gauge", *Review of Scientific Instruments*, Vol. 57, No. 4, April 1986, pp. 639-649

[14] Diller, "Advances in Heat Flux Measurements", *Advances in Heat Transfer*, Vol. 23, 1993, pp. 315-316

[15] Dunn, "Experimental short-duration techniques", *Convective Heat Transfer and Film Cooling in Turbomachinery*, 1986

[16] Fingerson, Freymuth, "Thermal Anemometers", *Fluid Mechanics Measurements*, J. Goodstein, ed., Hemisphere Publishing Corp., 1983, pp. 99-154

[17] Jiang, "Silicon Micromachined Flow Sensors", Ph.D. thesis, California Institute of Technology, 1998, p. 30-33

[18] Carslaw and Jaegar, **Conduction of Heat in Solids**, Oxford University Press, 1959, p. 77

[19] Biggs, J., Introduction to Structural Dynamics, McGraw-Hill Inc., 1964, p. 155

[20] http://mems.isi.edu/mems/materials/

[21] Epstein and Guenette

[22] Yifang Gong, Gas Turbine Laboratory, Massachusetts Institute of Technology, personal communication

[23] Carslaw and Jaegar, p. 139

[24] Carslaw and Jaegar, p. 202

[25] **Microsystems Technology Laboratories Annual Report**, Massachusetts Institute of Technology, May 2000, pp. 302-320

[26] Harbeke, Krausbauer, Steigmeier, Widmer, Kappert, and Neugebauer, "Growth and Physical Peoperties of LPCVD Polycrystalline Silicon Films", *Journal of Electrochemical Society*, Vol. 131, No. 3, 1984, pp. 675-682

[27] Jiang, Tai, Ho, Li

[28] Jiang, Tai, Ho, Li, p. 264

[29] A. Ayon, R. Braff, R Bayt, H. Sawin, and M. Schmidt, "Influence of Coil Power on the Etching Characteristics in a High Density Plasma Etcher", *Journal of the Electrochemical Society*, July 1999, Vol. 146, No. 7

[30] Firebaugh, "Investigation of Materials for Use in High-Temperature, Thin-Film Heaters and Temperature Sensors", M.S.E.E. thesis, Massachusetts Institute of Technology, 1997 pp.25-26

[31] Wright, **Shock Tubes**, John Wiley & Sons, Inc., 1961

[32] Liepmann, **Elements of Gasdynamics**, John Wiley & Sons, Inc., 1957, p 79

[33] Incropera, DeWitt, **Fundamentals of Heat and Mass Transfer**, John Wiley & Sons, Inc., 1981, p 460

[34] Townsend, Barnett, "Elastic Relationships in Layered Composite Media with Approximation for the Case of Thin Film on a Thick Substrate", *Journal of Applied Physics*, Vol. 62, No. 11, December 1987, pp. 4438-4444

[35] Obermeier, "Polysilicon as a Material for Microsensor Applications", *Sensors and Actuators: A*, Vol. 30, 1992, pp. 149-155

[36] Sharpe, Yuan, Vaidyanathan, "Measurements of Young's Modulus, Poisson's Ratio, and Tensile Strength of Polysilicon", *Proceedings of the Tenth IEEE International Workshop on Microelectromechanical Systems*, Nagoya, Japan, 1997, pp. 424-429

[37] Kamins, **Polycrystalline Silicon for Integrated Circuit Applications**, Kluwer Academic Publishers, 1988, p. 189

[38] Kamins, "Hall Mobility in Chemically Deposited Polycrystalline Silicon", *Journal of Applied Physics*, Vol. 42, 1971, pp. 4357-4365

[39] Rai-Choudhury, Hower, "Growth and Characterization of Polycrystalline Silicon", *Journal of Electrochemical Society*, Vol. 120, 1973, pp. 1761-1766

[40] Seto, "The Electrical Properties of Polycrystalline Silicon Films", *Journal of Applied Physics*, Vol. 46, 1975, pp. 5247-5254

[41] Lu, "A Quantitative Model of the Effect of Grain Size on the Resistivity of Polycrystalline Silicon Resistors", *IEEE Electron Device Letters*, March 1980, pp. 38-41

[42] Hughes, "Polycrstalline Silicon Resistors for Use in Integrated Circuits", *Solid State Technology*, May 1987, pp. 139-143

[43] Kim, "Electrical Characterization of Heavily Doped Polycrystalline Silicon for High-Frequency Bipolar Transistor Application", *IEEE Transaction on Electron Devices*, Vol. 34, No. 8, August 1987, pp. 1774-1780

[44] Luder, "Polycrystalline Silicon-Based Sensors", *Sensors and Actuators*, Vol 10, 1986, pp. 9-23

[45] Obermeier, pp. 149-155

[46] Luder, p. 14

[47] Incropera, p. 354

[48] The American Society of Mechanical Engineers, **Instruments and Apparatus: Part 1 Measurement Uncertainty**, ANSI/ASME PTC 19.1-1985, p11

[49] Beckwith, Marangoni, Lienhard, **Mechanical Measurements**, Addison-Wesley Publishing Co., 1993, pp. 82-83

[50] Mehra, Zhang, Ayon, Waitz, Schmidt, "Through-wafer Electrical Interconnect for Multilevel Microelectromechanical System Devices", *Journal of Vacuum Science & Technology B*, Vol 18, No. 5, Sep 2000, p 2583-2589